X-ray Spectral Studies of Ultra-Luminous Compact X-ray Sources in Nearby Galaxies

Ryohei Miyawaki

Department of Physics, School of Science,
University of Tokyo, Japan

abstract

Spectral studies of ultra-luminous compact X-ray sources (ULXs; Makishima et al. 2000) in nearby galaxies were conducted, motivated by a fundamental question whether they are accreting black holes that are significantly more massive than the ordinary stellar-mass black holes. In order to quantify the spectra and chase the spectral evolution, eight luminous nearby ULXs observed multiply with *Suzaku* and *XMM–Newton* were selected. From systematic studies of the sample ULXs, they were found to exhibit a common luminosity-dependent spectral evolution, in the following manner.

At relatively higher luminosities, the sample ULXs all showed convex-shaped spectra, which can be reproduced by a variable-p disk model with the temperature gradient index $p \sim 0.6$. Their luminosity changed approximately in proportion to the square of their inner-disk temperature. From these properties, ULXs in this state are interpreted as hosting "slim" accretion disks, just like Galactic/Magellanic black hole binaries (BHBs) that are shining at close to their Eddington limits.

When the luminosity decreases to 0.2–0.4 times those in the above state, the ULXs were confirmed to make clear transitions to a state where the spectra are much less convex, and are approximately expressed by a power-law (PL) model with $\Gamma = 1.5$–2.5. Furthermore, their spectral slope was found to steepen as the luminosity increases. When the data have high statistics, these PL-type spectra are often accompanied by a soft excess component, expressed by a cool (~ 0.3 keV) disk emission. Based on these results, the PL-type ULXs can be interpreted to be in the very-high state which is found among Galactic BHBs while they are somewhat less luminous than in the slim-disk state.

In some PL-type spectra, a spectral turn over at ≥ 6 keV was found. In particular, utilizing the broad energy band up to ~ 20 keV provided by the *Suzaku* Hard X-ray Detector, such a spectral curvature with a cutoff energy of ~ 6 keV was clearly observed from M82 X-1. Generally, these cutoff energies of PL-type ULXs are significantly lower than that observed in a Galactic BHB in its very-high state.

At the lowest luminosity, very soft spectra, approximated by a PL model with $\Gamma \sim 3$, were detected from two ULXs, NGC1313 Source A and Holmberg II X-1. Since the spectrum is better explained by adding a cool disk contribution at the softest spectral region, this state is considered to be analogous to the well established high/soft state of BHBs. This possibly provides the first evidence for standard accretion disks in ULXs.

Combining these results altogether, the sample ULXs have been inferred to stay below their Eddington limits, or under rather extreme assumption, to become mildly super-Eddington. Accordingly, the masses of our sample ULXs can be estimated as several tens to several hundreds $M_{\odot}$, which are significantly more massive than the ordinary stellar-mass BHBs.

Contents

Chapter 1

INTRODUCTION

Since the beginning of the cosmic X-ray investigations early in 1960s, various types of X-ray sources have been found in our Galaxy and the Magellanic clouds. Among them, the most luminous class of X-ray sources are X-ray binaries (XRBs), including neutron star binaries (NBSs) and black hole binaries (BHBs). They are close binary systems consisting of mass-donating ordinary stars and mass-accreting collapsed objects, wherein the X-ray emission is all fueled by gravitational energy of matter accreting onto these high density stars. Their X-ray luminosity reaches $\sim 10^{38}$ erg s^{-1}, which is consistent with the Eddington limit for compact objects with masses of ~ 1 to ~ 10 solar masses. In addition, a limited number of extra-Galactic X-ray sources were detected, including active galactic nuclei and nearby clusters of galaxies.

The *Einstein Observatory* launched in 1978, having X-ray imaging capability with a $\sim 10''$ angular resolution, for the first time enabled us to investigate much fainter X-ray sources, including discrete X-ray objects associated with nearby external galaxies. Although many of them were understood as NBSs, BHBs, and some young supernova remnants just like those in our Galaxy, it was discovered that some nearby galaxies host more luminous sources with their X-ray luminosity reaching $10^{39.5-40.5}$ erg s^{-1}. Since their luminosity exceeds by 1–2 order of magnitude the Eddington luminosity of NSBs (2×10^{38} erg s^{-1}), they could potentially be BHBs with as large a mass as $\sim 100\ M_{\odot}$, if they are obeying the Eddington limit. However, this interpretation was regarded as unlikely, since the current understanding of the stellar evolution cannot explain the formation of such massive black holes: no matter haw massive a star may be, it would most of its mass into stellar winds, and would end up with a black hole that is no massive than $\sim 20\ M_{\odot}$.

Thus, the nature of these objects remained an enigma.

With a wide-band (0.5–10 keV) spectroscopic capability and a moderate angular resolution ($\sim 3'$), *ASCA* , launched in 1993, enabled us to achieve a large progress in the study of these luminous objects, and led us to call them Ultra-Luminous compact X-ray sources (ULXs; Makishima et al. 2000).

In fact, *ASCA* spectra of a dozen of ULXs were successfully represented (Makishima et al. 2000; Mizuno et al. 2001; Mizuno 2000), by so-called multi-color disk (MCD) emission model, which successfully describes bright soft X-ray components emitted by Galactic BHBs. Furthermore, some ULXs were found to exhibit spectral transitions between the MCD-type spectra and a different spectral state characterized by power-law (PL) shaped spectra (Kubota et al. 2001). These novel results obtained with *ASCA* have for the first time established realistic astrophysical grounds on which we can regard ULXs as mass-accreting black holes, with possibly significantly higher masses than those found in the Local Group galaxies (including the Milky Way). The central paper, Makishima et al. (2000), has 210 citations (in refereed papers) as of 2007 December.

The *ASCA* discoveries described above have been reconfirmed and reinforced by *Chandra* and *XMM–Newton* observations of nearby galaxies, which gave us a much larger sample of ULXs thanks to their higher angular resolution. Through these studies, one comprehensive interpretation of ULXs, as described below, has been emerged (e.g., Sugiho 2003; Tsunoda et al. 2006; Mizuno et al. 2007). Namely;

1. ULXs are mass accreting black holes, and their high luminosities (relative to ordinary stellar-mass BHBs) reflect their higher (in absolute sense) mass accretion rates.

2. ULXs with PL-type spectra have overall X-ray properties that are similar to those of BHBs in a so-called very-high state (VHS), which appears at a luminosity close to the Eddington limit.

3. ULXs with MCD-type spectra are analogous in their X-ray spectral behavior to the stellar-mass BHBs in a so-called slim-disk state, which appears at still higher luminosities than the VHS.

4. An alternative scenario, which interprets ULXs as strongly beamed X-ray objects, is unlikely, considering luminous large-scale optical nebulosities found around some

objects (Pakull & Mirioni 2002): the nebulae require strong and rather isotropically radiating sources of excitation.

5. From 2 and 3 above, the luminosities of ULXs are not considered to largely exceed their Eddington limits.

6. It follows from 4 and 5 that ULXs indeed have rather high Eddington luminosities, and hence that they harbor rather massive stellar black holes, typically several tens to several hundreds solar masses.

7. Such heavier black holes may be produced as a result of run-away mergers of massive stars in dense stellar clusters (Ebisuzaki et al. 2001).

Although the above view provides one possible explanation, several authors (e.g., Okajima et al. 2006; Vierdayanti et al. 2006; Foschini et al. 2006) propose an alternative interpretation that ULXs are radiating at considerable super-Eddington luminosities, so that their masses need not to exceed $\sim 30\ M_{\odot}$ or so. At present, it is not yet settled whether this alternative interpretation is closer to the reality or not. This is because ULXs are much farther than Galactic BHBs, so that the available X-ray spectra are of much poorer quality, and their detection has been limited to < 10 keV. Furthermore, the number of observations of each source remained too small to clearly understand their spectral changes.

The aim of the present thesis is to elucidate the nature of ULX, through the analysis of accumulating X-ray data, employing the above listed items 1 through 7 as our working hypothesis. For this purpose, we utilize a large amount of archival data from the European *XMM–Newton* satellite, and study luminosity-related spectral changes of a fair number of ULXs. Furthermore, we utilize our *Suzaku* satellite, which allows us wide-band observations with an unprecedented sensitivity. The author of this thesis has deeply contributed to the development, fabrication, and calibration of the Hard X-ray Detector (Takahashi et al. 2007; Kokubun et al. 2007) onboard *Suzaku* , as well as to the operation of *Suzaku* .

In Chapter 2, we summarize the overall knowledge on ULXs accumulated so far. Chapter 3 describes we introduce instruments utilized in the present data analysis. Before analyzing the observational data, we explain in Chapter 4 targets, observational datasets, and analysis procedures. Chapter 5 and Chapter 6 describe results of spectral analysis,

utilizing the observational data of target ULXs. We discuss the obtained results in Chapter 7, and finally, summarize the thesis in Chapter 8.

Chapter 2

REVIEW

2.1 X-ray Sources in Normal Galaxies

2.1.1 X-ray sources in our Galaxy

Since the first discovery of an X-ray source outside the solar system, namely Sco X-1 (Giacconi et al. 1962), it has been known so far that X-rays are radiated more or less from all kinds of stellar objects in our Galaxy. Among them, typical luminous X-ray sources include X-ray binaries (XRBs), which are close binary systems each consisting of a mass-donating ordinary star and a mass-accreting collapsed objects. They are classified into white dwarf (WD) binaries with an X-ray luminosity of $L_{\rm X} \sim 10^{30-34}$ erg s^{-1} , neutron star binaries (NSBs, $L_{\rm X} \sim 10^{36-38}$ erg s^{-1}), and black hole binaries (BHBs, $L_{\rm X} \sim 10^{36-39}$ erg s^{-1}). The X-ray emission from these binaries is all fueled by gravitational energy of matter accreting onto these high density stars. When a proton falls onto the surface of a typical WD and neutron star (NS), an energy of ~ 0.2 MeV and ~ 200 MeV, respectively, is released. Similarly, a proton falling onto a black hole (BH) releases $\sim \frac{1}{6} m_{\rm p} c^2 \simeq 160$ MeV (with $m_{\rm p}$ the proton mass and c the light speed) while it reaches 3 times the Schwarzschild radii. Thus, the accretion onto NSs and BHs is a highly efficient conversion process of gravitational energies into radiation.

Of course, the mass accretion is not the only energy source of Galactic X-ray sources. For example, some WD binaries, called super soft sources (SSSs, $L_{\rm X} \sim 10^{38}$ erg s^{-1}), are considered to emit their luminous soft X-rays via stable nuclear fusion on the surface; although accretion is a necessary condition, the X-ray emission in this case is sustained by

nuclear energy (~ 1 MeV per nucleon), rather than the gravitational energy release (~ 0.2 MeV per nucleon) described above. Isolated NSs also emit X-rays ($L_{\rm X} \sim 10^{31-36}$ erg s^{-1}); most of them are known as rotation-powered pulsars, which are radiating by consuming their rotational energies. As another type of X-ray emitting objects, supernova remnants (SNRs) derive their X-ray luminosities ($L_{\rm X} \sim 10^{35-38}$ erg s^{-1}) from kinetic energies of the expanding matter shell, via creation of hot plasmas or acceleration of non-thermal particles, both via the strong shocks. Finally, stellar coronae in various types of stars, created by magnetic activity, all become thermal X-ray emitters ($L_{\rm X} \sim 10^{26-34}$ erg s^{-1}).

2.1.2 X-ray sources outside our Galaxy

In early days, our knowledge on X-ray sources outside our Galaxy had been limited mainly to active galactic nuclei (AGNs), which are mass-accreting super-massive black holes (SMBHs) of $10^5 \sim 10^9$ $M_\odot$, where $M_\odot = 2.0 \times 10^{33}$ g represents the solar mass, sitting at galactic centers. The *Einstein Observatory*, launched in 1978 (Giacconi et al. 1979), provided for the first time an X-ray imaging capability with an angular resolution of $\sim 10''$, and enabled X-ray source population studies over a large sample of external galaxies (Fabbiano et al. 1992). It was shown that elliptical galaxies are usually more X-ray luminous than spirals, and their X-rays are dominated by a large-scale hot gaseous component of temperature ~ 1 keV. Among spirals, starburst galaxies are rather X-ray luminous, also harboring a hot gaseous component which probably originates from the star formation activity. X-ray emission from other normal galaxies was generally understood as an assembly of discrete X-ray sources, among which the most luminous and rather isolated ones were individually resolved by the imaging optics. Although some of these luminous discrete sources in external galaxies were securely regarded as NSBs, BHBs, and SNRs, an amazing discovery was that some others are too luminous ($L_{\rm X} = 10^{39-40}$ erg s^{-1}) to be identified with any class of X-ray sources known in our Galaxy. This is the discovery of the fascinating objects now called ULXs (Ultra-Luminous compact X-ray sources), which form the central subject of the present thesis.

A majority of point sources observed in nearby galaxies are less luminous than 2×10^{38} erg s^{-1}. Hence they are consistent with being NSs, because the Eddington luminosity for a NS of $1.4 M_\odot$mass (Bethe et al. 1995) is $\sim 2 \times 10^{38}$ erg s^{-1}. The Eddington luminosity

is given as

$$L_{\rm E} = 1.5 \times 10^{38} \frac{M}{M_\odot} \ \ {\rm erg\ s^{-1}}. \tag{2.1}$$

This is determined by the balance between the gravitational force from the central body of mass M and the outward radiation pressure from it, assuming the cosmic helium/hydrogen ratio. This balance is written as

$$\frac{GM\rho}{R^2} \geq \frac{Ln\sigma_{\rm T}}{4\pi R^2 c}, \tag{2.2}$$

using the gravitational constant G, a distance from the center of the accretion star R, a mass density of the gas ρ, a bolometric luminosity of the source L, a number density of the electrons n, and the Tomson scattering cross section $\sigma_{\rm T}$. Accordingly, the bolometric luminosity from any celestial body cannot persistently exceed the Eddington luminosity, as long as the radiation is rather isotropic. This limit is supported by the observational fact, for example, that the X-ray luminosity of an NSB saturates at a value consistent with equation 2.1, when it exhibits an unstable nuclear fusion called X-ray bursts (e.g. Inoue et al. 1981). In this sense, ULXs are amazingly luminous, because their luminosity reaches 10–100 times the Eddington limit of NSs. While a straightforward interpretation of ULXs is to regard them as BHBs with masses of 10–100 $M_\odot$, the idea was not examined seriously, since the current understanding of the stellar evolution cannot explain the formation of such massive BHs. Thus, the nature of ULXs has been remained a big puzzle.

A large progress for understanding the nature of the ULXs was provided by *ASCA* , which enabled wideband (0.5–10 keV) spectroscopy with a moderate angular resolution ($\sim 3'$). Utilizing *ASCA* , Makishima et al. (2000) conducted spectral studies of a dozen of ULXs, and found for the first time that their X-ray spectra resemble those observed from established Galactic BHBs (§2.5). They proposed that ULXs harbor accreting black holes which are significantly more massive than those in ordinary BHBs, named them "Ultra-Luminous compact X-ray sources (ULXs)", and pointed out their importance because their luminosity falls in between those of BHBs and AGNs.

With the launch of the *Chandra Observatory* (in 1999), having a sub-arcseconds angular resolution, we have become able to study X-ray populations in galaxies of various morphological types at a distance of several tens Mpc, down to a typical limiting luminosity of $\sim 10^{37}$ erg s^{-1} . Figure 2.1 shows an X-ray image of M83 obtained by *Chandra* where

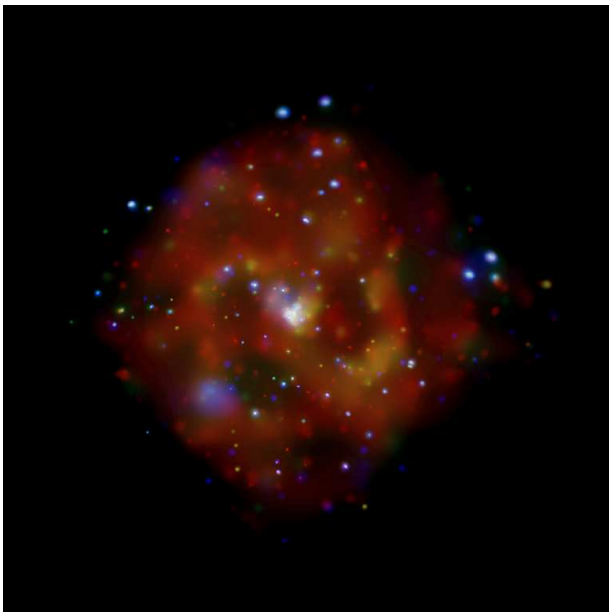

Figure 2.1: A 0.3–8 keV X-ray image of M83 observed by *Chandra* (Soria & Wu 2002; from http://chandra.harvard.edu), Many of point-like sources are visible, where lower energy emission is shown in red, and higher energy emission in blue.

a large number of point-like sources are resolved. These X-ray sources are considered as an inhomogeneous mixture of accreting NSBs, BHBs, luminous SNRs, and ULXs which are the brightest several objects located relatively off the galaxy center. Thus, ULXs are single objects, rather than unresolved clumpings of several NSBs or BHBs.

Figure 2.2 shows integrated source number distributions (i.e. X-ray luminosity functions; LFs) observed in several types of galaxies. We can see that some galaxies have X-ray LFs well extending beyond $\sim 10^{39}$ erg s^{-1} , and hence ULXs are an established population of X-ray sources observed in nearby galaxies. In addition, Grimm et al. (2003) reported that an LF of X-ray sources in a large number of nearby galaxies is extending up to 2×10^{40} erg s^{-1} . Because an LF of Galactic X-ray sources is up to $\sim 10^{39}$ erg s^{-1} and Galactic BHBs have their mass of $\sim 10\ M_{\odot}$, this suggests that ULXs are dominated by BHs of mass up to $\sim 100\ M_{\odot}$.

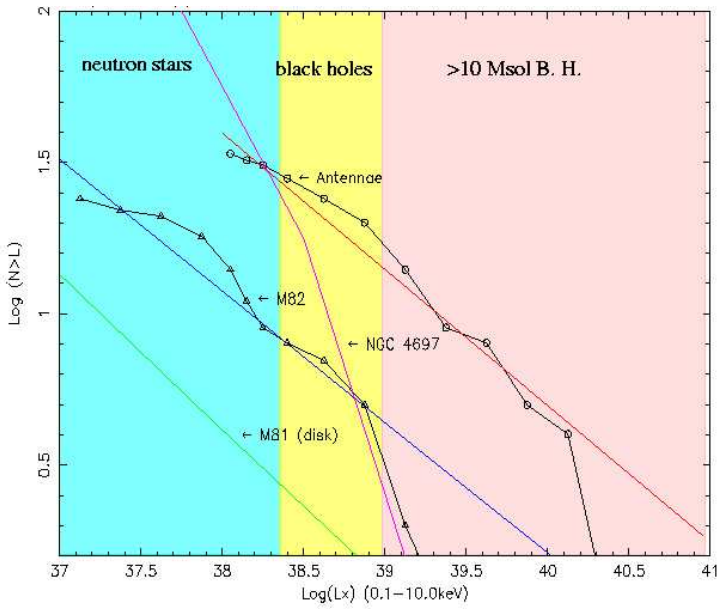

Figure 2.2: X-ray luminosity functions of four reprensentative galaxies obtained by *Chandra* observations (Zezas et al. 2002; from http://chandra.harvard.edu). Both data points and best-fit power-law models are shown for the Antennae and M82. Only the best-fit power-law models are shown for the elliptical galaxy NGC4697 and the disk of M81 (a spiral galaxy). The background is divided into three luminosity intervals and painted in blue (NSs; $L_{\rm X} \leq 2 \times 10^{38}$ erg s^{-1}), yellow (ordinary-mass BHs; $2 \times 10^{38} \leq L_{\rm X} \leq 10^{39}$ erg s^{-1}), and red (BHs with $M \geq 10\ M_{\odot}$; $L_{\rm X} \geq 10^{39}$ erg s^{-1}).

2.2 Black Hole Binaries (BHBs)

2.2.1 An overview

Among handful X-ray sources discovered by early X-ray observations including the strongest source Sco X-1, Cyg X-1 is the first that was suggested by Oda et al. (1971) to contain a BH, on the basis of its peculiar characteristics such as rapid variability. Soon after, Cyg X-1 was optically identified with a 9.6 mag O-type star (Bolton 1972), which was considered to be the mass-donating component. Then, the optical radial-velocity measurements of the companion star yielded the mass of the X-ray emitter as $\sim 10\ M_{\odot}$(e.g. Paczynski 1974). Since this significantly exceeds the theoretical upper-limit mass for a NS, it has become a general consensus that Cyg X-1 is indeed a BH.

Today, at least twenty XRBs in our Galaxy and Large Magellanic cloud (LMC) are regarded as BHBs (e.g. Tanaka & Lewin 1995; McClintock & Remillard 2006). Most of these BHBs are transient sources, and only three of them are known as persistent sources (Cyg X-1, LMC X-1, and LMC X-3). However, both these types of BHBs show common spectral properties in the X-ray band, so we discuss them together. As shown in figure 2.3, they generally exhibit two distinct spectral states; low/hard and high/soft states, with lower and higher luminosities, respectively. In the hard state, the X-ray emission from BHBs is characterized by strong time variability and a single power-law spectrum with a photon index of $\Gamma = 1.4 \sim 1.7$. The power-law spectrum often shows an exponential cutoff in the range from several tens keV to ~ 100 keV. In the soft state, a BHB spectrum is characterized by a prominent ultrasoft thermal component below 10 keV, and a steep power-law hard-tail with a photon index of $\Gamma = 2.0 \sim 2.5$. They usually show spectral transitions between the hard and soft states, typically at a threshold of a few percents of the Eddington luminosity.

The ultrasoft component characterizing the soft state is thought to be emitted from an optically thick and geometrically thin accretion disk, created around a BH under a high accretion rate (Shakura & Sunyaev 1973). As described in detail in the next subsection, the ultrasoft component is expressed well by a spectral model called multi-color disk (MCD) model (Makishima et al. 1986), with its characteristic disk temperature of $T_{\rm in} =$ 0.5–1.2 keV. In the hard state, in contrast, the accretion disk around a BH is considered to be optically thin and geometrically thick, due to the low accretion rate wherein radiative

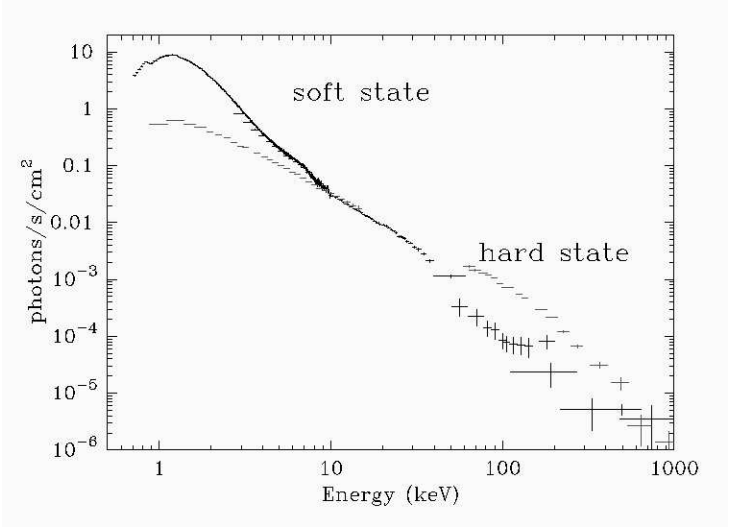

Figure 2.3: X-ray to soft γ-ray spectra of Cyg X-1 in the soft/high state (solid symbols) and the hard/low state (dotted symbols), obtained by some recent observations (from Kubota 2001).

cooling is inefficient. The spectrum is interpreted in terms of Comptonization of soft photons by thermal electrons with a temperature $\sim$ 100 keV, as is indicated by the spectral high-energy cut-off. The overall property in the hard state is understood by the concept of advection-dominated accretion flow (ADAF; Ichimaru 1977; Narayan & Yi 1994).

2.2.2 Emission from standard accretion disks

Here, we summarize the theory of the standard accretion disk (Shakura & Sunyaev 1973), typically observed in the high/soft state of BHBs. We also introduce so-called multi-color disk model (the MCD model; Mitsuda et al. 1984), which is employed as a convenient approximation to the integration spectrum expected from an optically-thick standard accretion disk.

Around the compact object (e.g. a BH) in a close binary, the inflow matter from the mass-donating star is expected to form an accretion disk due to its angular momentum. The viscous stress in differentially rotating matter, exerted by gas pressure and magnetic field, can transport the angular momentum outward. When the accretion rate is high, the disk is expected to be geometrically thin and optically thick, because of an efficient

radiative cooling. The standard accretion model is an analytic solution to the accretion flow in this physical state, obtained by Shakura & Sunyaev (1973) to explain the X-ray spectra of soft-state BHBs. Assuming that the kinetic energy of the matter in Keplerian motion dominates that in radial motion. The virial theorem predicts that just half the gravitational energy release is converted into the Keplerian energy, while the remaining half is radiated as blackbody with a local effective temperature $T_{\rm eff}$. Then, the radiative energy flux density, as a function of radius r from the center, is expressed as

$$\sigma \left\{T_{\rm eff}(r)\right\}^4 = \frac{3GM\dot{M}}{8\pi r^3}\left(1-\sqrt{\frac{R_{\rm in}}{r}}\right) \ , \tag{2.3}$$

where M is the compact object mass, $\dot{M}$ is the mass acrretion rate, $R_{\rm in}$ is the radius of inner disk boundary, G is the gravitational constant, and σ is the Stefan-Boltzmann constant. The energy flux from such a disk observed at a distance d and inclination i is given as

$$F(E) = \frac{\cos i}{d^2}\int_{R_{\rm in}}^{R_{\rm out}} 2\pi r B(E, T_{\rm eff}(r)) d{\rm r} \ , \tag{2.4}$$

where $B(E,T)$ is the blackbody spectrum function of temperature T and photon energy E, and $R_{\rm out}$ is the outer disk radius.

The MCD model neglects the term $\sqrt{R_{\rm in}/r}$ in equation (2.3), and approximates the effective temperature T as

$$T(r) = \begin{cases} 0 & (r < r_{\rm in}) \\ T_{\rm in}\left(\frac{r}{r_{\rm in}}\right)^{-\frac{3}{4}} & (r > r_{\rm in}) \end{cases} \ , \tag{2.5}$$

where $r_{\rm in}$ is another radius parameter close to but somewhat larger than $R_{\rm in}$. This approximated temperature becomes equal to the true inner disk temperature $T_{\rm in}$ at $r_{\rm in}$. Thus, assuming $R_{\rm out} \gg r_{\rm in}$, the overall energy spectrum from the disk is obtained by integrating equation (2.4) from $r = r_{\rm in}$ out to infinity. We show the shape of an MCD-spectrum in Figure 2.4; it exhibits a power-law shape with $\Gamma = 2/3$ at $E \ll kT_{\rm in}$, while it behaves like a blackbody model at $E \gg kT_{\rm in}$. The bolometric luminosity from the disk is given by integrating this spectrum over the energy, as

$$L_{\rm bol} = 2 \times \int_{r_{\rm in}}^{R_{\rm out}} 2\pi r \sigma T(r)^4 dr = 4\pi\sigma r_{\rm in}^2 T_{\rm in}^4 \ , \tag{2.6}$$

where the first factor of 2 means the two sides of the disk.

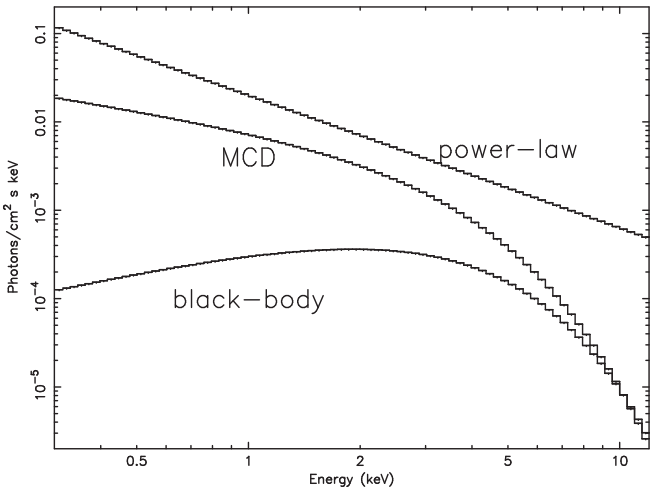

Figure 2.4: X-ray model spectra, in terms of the photon number flux emitted per unit interval of the photon energy. From top to bottom, a power-law (PL) with photon index $\Gamma = 1.5$, an MCD model with $T_{\rm in} = 1.2$ keV, and a blackbody (BB) with $T = 1.2$ keV. Their normalizations are arbitrary.

2.2.3 Application of the MCD model to actual X-ray data

Although the MCD model spectrum is regarded as a very accurate approximation to the exact Shakura & Snyaev solution, we need several cautions when converting the MCD model parameters ($r_{\rm in}$ and $T_{\rm in}$) to physical values of the disk. First, because the inner boundary condition is different in the MCD approximation from the Shakura & Sunyaev disk solution, the value of $r_{\rm in}$ obtained through an MCD fit to the actual data must be multiplied by a correction factor to obtain the true radius $R_{\rm in}$. The factor, $\xi = R_{\rm in}/r_{\rm in} \sim 0.41$, is obtained by equating $T_{\rm in}$ with $T_{\rm max}$ (Kubota et al. 1998). Furthermore, the effect of electron scattering in the disk vertical direction is expected to make the observed color temperature T higher than the effective temperature by a "hardening factor" κ, as previously observed in X-ray bursts (Nakamura et al. 1989). Shimura & Takahara (1995) obtained $\kappa = 1.7$. Takining into account these effects, we obtain (Makishima et al. 2000)

$$R_{\rm in} = \kappa^2 \xi r_{\rm in} = 1.19 \left(\frac{\kappa}{1.7}\right)^2 \left(\frac{\xi}{0.41}\right) r_{\rm in} \ . \tag{2.7}$$

The MCD model has successfully reproduced the ultrasoft component observed in the spectra of high-state BHBs (e.g. Makishima et al. 1986 for GX 339–4; Ebisawa et al. 1993 for LMC X–3; Dotani et al. 1997 for Cyg X–1). Furthermore, the value of $r_{\rm in}$,

hence $R_{\rm in}$ too, has been confirmed to be really constant in several BHBs, even though the X-ray intensity varied significantly (e.g. Ebisawa 1991 for LMC X–3; Ogawa 1992 for GS 2200+25; Takizawa 1991 for GS 1124–68). We may then assume that $R_{\rm in}$, determined by the actual X-ray spectrum, corresponds to the radius of the last stable orbit around a Schwarzshild BH. This yields a relation as

$$R_{\rm in} = 3\alpha R_{\rm s} = 3\alpha \cdot \frac{2GM}{c^2} = 8.85\alpha \left(\frac{M}{M_\odot}\right) \ {\rm km} \ , \tag{2.8}$$

where $R_{\rm s} = 2GM/c^2$ is the Schwarzshild radius and α is a numerical factor used for including the Kerr metric; $\alpha = 1$ for a Schwarzshild BH and $\alpha = 1/6$ for an extreme Kerr BH. We can therefore estimate the BH mass from the X-ray knowledge as

$$M = \frac{c^2}{6\alpha G} R_{\rm in} = \frac{c^2}{6\alpha G} \xi \kappa^2 \sqrt{\frac{L_{\rm bol}}{\sigma T_{\rm in}^4}} = \frac{c^2}{6\alpha G} \xi \kappa^2 \sqrt{\frac{d^2 F_{\rm bol}}{\sigma T_{\rm in}^4 2\cos i}} \ . \tag{2.9}$$

The masses of several representative BHBs have actually been estimated in this way. Indeed, the results obtained with $\alpha = 1$ generally agree with their optically estimated dynamical masses (Makishima et al. 2000). Thus, by utilizing the MCD model, a consistent picture as to the soft-state BHBs has been obtained from X-ray observations.

Finally, we examine the properties of standard disks in some more details. The bolometric luminosity of the disk is given from equation 2.6 as

$$L_{\rm bol} = 7.2 \times 10^{38} \left(\frac{\xi}{0.41}\right)^{-2} \left(\frac{\kappa}{1.7}\right)^{-4} \alpha^2 \left(\frac{M}{10\ M_\odot}\right)^2 \left(\frac{T_{\rm in}}{\rm keV}\right)^4 \ {\rm erg\ s^{-1}} \ . \tag{2.10}$$

In order to directly relate $T_{\rm in}$ and M, let us normalize the bolometric luminosity to the Eddington limit as $L = \eta L_{\rm E}$, where η is a dimensionless factor. Then, we obtain from equations (2.1) and (2.10)

$$L_{\rm bol} = 3.1 \times 10^{39} \left(\frac{\xi}{0.41}\right)^2 \left(\frac{\kappa}{1.7}\right)^4 \alpha^{-2} \eta^2 \left(\frac{T_{\rm in}}{\rm keV}\right)^{-4} \ {\rm erg\ s^{-1}} \ , \tag{2.11}$$

where M is eliminated, and

$$T_{\rm in} = 1.2 \left(\frac{\xi}{0.41}\right)^{\frac{1}{2}} \left(\frac{\kappa}{1.7}\right) \alpha^{-\frac{1}{2}} \eta^{\frac{1}{4}} \left(\frac{M}{10\ M_\odot}\right)^{-\frac{1}{4}} \ {\rm keV} \ , \tag{2.12}$$

where $L_{\rm bol}$ is eliminated. Thus, more massive BHs are inferred to have lower disk temperatures, when compared at the same value of η. For example, massive ($M \sim 10^{6-9} M_\odot$) BHs at the center of many galaxies are thought to have $T_{\rm in} \sim$ 1–30 eV, so that their disk

emission is expected to emerge in the vacuum ultraviolet frequency where observation is severely hampered by interstellar absorption.

While the bright ultrasoft component in the soft-state spectra is well represented by the emission from the standard accretion disk, the spectra above ∼10 keV is dominated by a hard tail (figure 2.3). These hard tails, described by a power-law model with a photon index $\Gamma \sim 2.4$, are steep, compared with the entire power-law like continuum in the hard-state BHBs, but extended to MeV energies without a break. The hard-tail component in the hard state is little understood.

2.2.4 Solutions beyond the standard disk

As described so far, the picture of the standard accretion disk is simple and physically well-understood. However, this picture has recently been found to be sometimes broken when the disk luminosity reaches a certain critical luminosity, which is of the same order as, but not necessarily identical to $L_{\rm E}$.

Figure 2.5 is *RXTE* spectra from the transient BHB, XTE J1550−564, where panel (a), observed at $L \sim 0.2 L_{\rm E}$, is consistently interpreted in terms of the standard scenario. However, as the system gets brighter and enters an anomalous state of panel (b), where the disk emission is overwhelmed by a strong power-law component with a relatively steep slope of $\Gamma = 2.5$–3.0, as if the hard tail in the soft state has drastically increased. When this spectrum is fitted with an MCD component and a power-law, the derived values of $T_{\rm in}$ become rather high, as shown in figure 2.6. At the same time, the estimated values of $R_{\rm in}$ become no longer constant, and are often unusually small. This state, often called the very-high state (VHS), was discovered in observations with *Ginga* (e.g. Miyamoto et al. 1991).

Together with the above spectral features, the VHS is characterized by large intensity variations accompanied by quasi-periodic oscillations (QPOs). Based on the *RXTE* observations of three Galactic BHBs, GRO J1655−40, XTE J1550−564, and 4U1630−47, Kubota et al. (2001), Kubota & Makishima (2004), and Abe et al. (2005) respectively found that the strong hard emission in the VHS is most likely caused by inverse Compton scattering due to high energy electrons that may reside around the disk. They for the first time found quantitatively that $R_{\rm in}$ returns to the same value as seen in the standard regime, if the Compton effect is taken into account. This scenario is

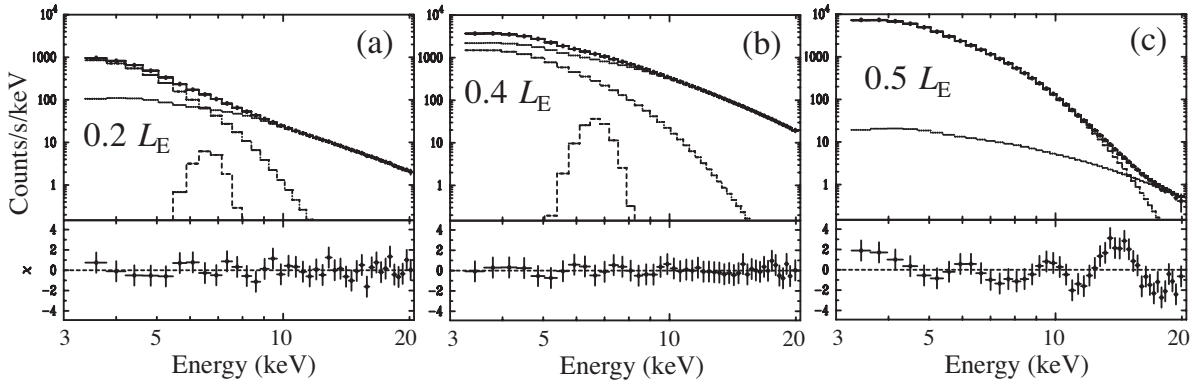

Figure 2.5: Three typical spectra of XTE J1550-564 obtained by *RXTE* Proportional Counter Array (Kubota & Makishima 2004). The best-fit MCD plus power-law models are also shown. The lower panel of each spectrum shows fit residuals. The results of (a) the high/soft state, (b) the very-high state, and (c) the slim-disk state are shown.

consistent with those of QPOs, which are usually thought to be related to some corona surrounding the disk. Thus, in the very-high state, the standard accretion disk is still present, but is considered to be surrounded by a rather thick and hot corona presumably due to enhanced radiation pressure.

In addition to the very-high state, another unusual state appeared in the brightest period of XTE J1550−564, (Kubota & Makishima 2004), as shown in figure 2.5 (c). Like in the case of the standard state, the X-ray spectrum is apparently expressed by a superposition of the dominant soft component and a weak power-law tail, as shown in figure 2.5 panel (c). However, the spectral shape of the soft component is somewhat distorted from that of the standard disk, and implies a significantly higher disk temperature. The disk luminosity is no longer proportional to $T_{\rm in}^4$, but to $T_{\rm in}^2$ (or $r_{\rm in} \propto T_{\rm in}^{-1}$). As argued by Kubota & Makishima (2004), this state shows a sign of optically-thick ADAF, or equivalently so called "slim disk", which is predicted to be formed at high accretion rates near or even above the Eddington limit (Abramowicz et al. 1988; Watarai et al. 2000). In this state, the accretion flow is thought to obey a solution which is different from that of Shakura & Sunyaev; the matter now acquires a considerable radial infall velocity, rather than follow a Keplerian rotation. The gravitational energy release is mainly carried away by advection, instead of being radiated away. As a result, the radiation luminosity becomes saturated at $\sim L_{\rm E}$ (or somewhat higher), even when the accretion rate keeps increasing.

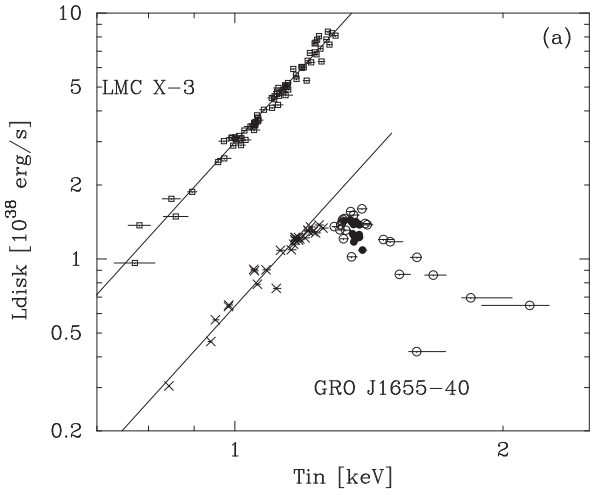

Figure 2.6: The accretion-disk luminosity of the two BHBs, LMC X-3 and GRO J1655−40, shown as a function of the measured time (Kubota et al. 2001). The solid lines represent the $L_{\rm disk} \propto T_{\rm in}^4$ relation.

Furthermore, the accretion disk becomes optically thick even at $r < 3R_s$ (Mineshige et al. 2000; Watarai et al. 1999, 2000), which makes the innermost disk temperature higher.

In order to empirically approximate the X-ray spectrum emergent from a slim disk, Mineshige et al. (1994), Hirano et al. (1995), and Kubota (2001) modified the MCD formula into so called varible-p disk model, which assumes that the temperature profile follows $T(r) \propto r^{-p}$ with a free parameter p, instead of $r^{-0.75}$ in equation (2.5) of the MCD model. This empirical modification has been motivated by the fact that the radial temperature profile of a "slim disk" approaches $T(r) \propto r^{-0.5}$ in the extreme case. The spectra for several representative values of p are given in Figure 2.7. Utilizing this model, Kubota (2001) analyzed the spectra of XTE J1550−584, and found that p indeed approaches ~ 0.5 when $R_{\rm in}$ is changing as $\propto T_{\rm in}^{-1}$ at the highest luminosity phase ($L \sim 0.5 L_E$).

As described so far, our current understanding of BHBs is that they have four distinct spectral states: the low/hard state, the high/soft state, the VHS, and the slim-disk state, in the increasing order of accretion rates. Figure 2.8 illustrate spectral shapes of these four states. This overall picture provides us a basis in trying to understand the ULX phenomena.

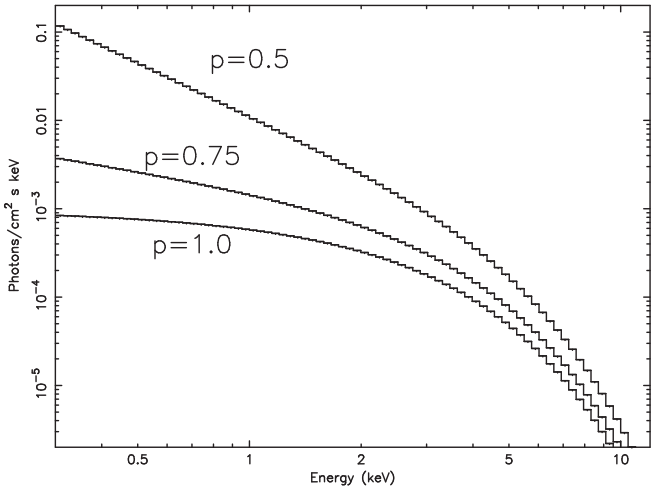

Figure 2.7: The spectral shape of the varibale-p disk model for different values of p. As p decreases, the low energy slope of the spectrum steepens.

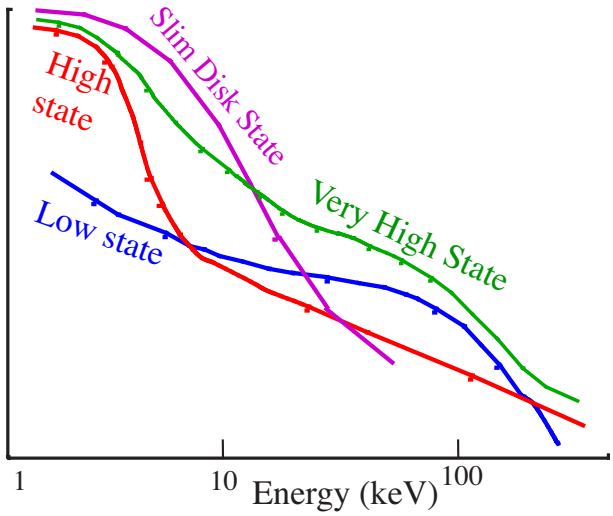

Figure 2.8: An overall picture of the four spectral states observed in Galactic BHBs.

2.3 Ultra-Luminous Compact X-ray Sources (ULXs)

Since their discovery by *Einstein* , a number of ULXs have been found and extensively studies by various observatories. For instance, using archival observations of *ROSAT* High Resolution Imager, Liu & Bregman (2006) found 109 ULXs with their luminosities exceeding 10^{39} erg s^{-1} in 313 nearby galaxies within 40 Mpc. Furthermore, utilizing *Chandra* and *XMM–Newton* data, Sugiho (2003) analyzed about 50 ULXs with X-ray luminosity above 2×10^{39} erg s^{-1} in 64 nearby galaxies. On the other hand, our Galaxy and the Local Group galaxies apparently host no ULXs, except one "transition-class" object with $L \sim 1 \times 10^{39}$ erg s^{-1} . This is not unnatural bacause it is estimated that between about 1 in $4 \sim 8$ galaxies host X-ray luminous objects with luminosity in excess of 10^{39} erg s^{-1} (Ptak & Colbert 2004; Liu, Bregman & Irwin 2006). ULXs are associated predominantly with late-type galaxies (spirals and irregulars), rahter than early-type elliptical galaxies (e.g. Sugiho 2003). Furthermore, star-burst galaxies often have an enhanced population of ULXs (e.g. Fabbiano et al. 2001; Roberts et al. 2002; Miyawaki et al. 2004). Generally, ULXs are located in star forming and spiral arms of their host galaxies with clear signature of young populations.

As indicated by the X-ray luminosity functions (figure 2.2), some ULXs exhibit luminosities reaching up to several times 10^{40} erg s^{-1} . Futhermore, using the *Chandra* imaging, Matsumoto et al. (2001) and Kaaret et al. (2001) revealed that the star-burst galaxy, M82, hosts an off-center luminous source with its peak luminosity reaching 10^{41} erg s^{-1} . That is the most extreme object among a number of ULXs known so far. Assuming isotropic radiation with a sub-Eddington luminosity (from equation 2.1), a mass of at least 700 $M_{\odot}$ is necessary to account for the highest luminosity recorded from this object.

ULXs cannot be foreground objects belonging to our Galaxy, since none of them have been identified with any bright stellar objects in other wavelengths. Furthermore, statistical calculation show that well established ULXs known from the *Einstein* era, with a typical flux of $> 5 \times 10^{-13}$ erg s^{-1}cm^{-2} and clear association with nearby luminous galaxies, have a negligible (below 1%) chance of being a background AGN (Fabbaino et al. 1989). Accordingly, we regard ULXs as really belonging to their host galaxies. Although the distance estimates generally have uncertainties, the Cepheid distances, which are accurate within $\lesssim 10\%$, have become available for some galaxies (Freedman et al. 2001). Thus, the ULXs luminosities obtained by assuming an isotropic radiation and nominal

distances to their host galaxies are sufficiently reliable.

Until early 1990's, we were still left with an interpretation that ULXs are luminous SNRs, which are free from the Eddington limit constraint. However, many ULXs were then found to exhibit time variability on time scales from several hours to years, by up to a factor of ∼10 (§2.6). Therefore, most if not all, ULXs must be compact objects, probably powered by accretion. Furthermore, the superb angular resolution ($\sim 0.5''$) of *Chandra* revealed many ULXs to be really point-like, with and upper-limit size of ∼10 pc. Thus, there is no room left for yet another interpretation, that a ULX is composite of multiple accreting objects which individually satisfy the Eddington limit of reasonable mass. Therefore, a ULX cannot be interpreted other than a single compact object, which appears truly as luminous as we observe.

2.4 Possible explanations for ULXs

Taking it for granted that ULXs are generally single mass-accreting compact objects, their high luminosities up to 10^{41} erg s^{-1} , assuming isotropic emission, allow at least the following three alternative and competing interpretations.

2.4.1 Intermediate-mass BHs (IMBHs)

One interpretation of ULXs is to assume that they are close binaries involving unusually massive (up to 100–1000 $M_\odot$) stellar BHs, in order for their high luminosities to remain sub-Eddington. This alternative has some empirical basis in that all kinds of compact objects in the Milky Way basically radiate below the Eddington limit. However, this interpretation is at the same time subject to a serious difficulty, that the stellar remnant black holes which are known in our own Galaxy and the Magellanic clouds have their masses in the range 3 $M_\odot < M <$ 18 $M_\odot$(McClintock & Remillard 2006). Furthermore, Fryer & Kalogera (2001) calculated that the vast majority of black holes formed from the evolution of a single massive star will have mass $< 20\ M_\odot$, clearly inadequate to power the brighter end of the ULX population if obeying the Eddington limit. This is because any massive star will lose a large fraction of its mass in stellar winds, before it finally collapses into a BH. Thus, other possibilities have often been discussed, without involving such massive stellar BHs.

2.4.2 Beamed emission

One attempt to explain the high ULX luminosity without violating the Eddington limit nor appealing to unusualy massive BHs is to consider that their X-ray radiation is strongly ($\sim$ 10 times) beamed toward us, and hence they appear much more luminous than they actually are. Such an X-ray beaming may be produced either through relativistic boosting of their X-ray emission along our line-of-sight (Kording, Falcke & Markoff 2002), or through collimation of their radiation probably by a geometrically-thick accretion disk such that it only escapes into a fraction of the sky (King et al. 2001, King 2002). However, luminosities of the most luminous Galactic NSBs fall $\sim$100 times short of those of the most luminous ULXs. Even if we assume BHBs with ordinary masses (10–20 $M_{\odot}$), the luminosity is 10$\sim$100 times insufficient. Therefore, uncomfortably high collimation (10–100) would be needed to explain ULXs as beamed radiation from NSBs, or BHBs of ordinary masses. There is no known mechanism to produce such a strong X-ray beaming. In addition, ULXs are often surrounded by optical emission nebulae (§§2.7.2), and the necessity for their excitation suggests that their central ULXs are radiating rather isotropically.

2.4.3 Super-Eddington emission

The other possibility is that ULXs are really at significant super-Eddington luminosities. One possible mechanism for such a super-Eddington radiation is radiation-pressure-dominated inhomogeneous disk, where a geometrical arrangement of emission and absorption regions allow the photons to escape without interacting with surrounding material (Begelman 2002). Hence, super-Eddington luminosities are achieved and maintained, up to a factor <10 above the Eddington limit (Begelman 2002; Ebisawa et al. 2003; Heinzeller & Duschl 2007). Even without invoking such ideas, the slim disks discribed in §§2.2.4 will become a mildly super-Eddington objects, if the mass accretion rate is highly super-Eddington. If these mechanisms are operating, we can explain the ULX luminosity up to $\sim 10^{40}$ erg s^{-1} as emerging from ordinary mass ($\sim$ 10 $M_{\odot}$) BHBs or NSBs. However, the highest luminosity of $\sim 10^{41}$ erg s^{-1}, observed from the most luminous source in M82, cannot be explained by this scenario. Thus, this alternative is also speculative like the other two.

2.5 X-ray Spectral Properties of ULXs

X-ray spectra often inform us of important physical conditions of target objects. In this section, we review X-ray spectra so far observed from ULXs.

2.5.1 Overall features of ULX spectra

In the era of *Einstein* and *ROSAT* , X-ray spectral studies were limited within the bandpass up to $\sim$ 3 keV with relatively poor energy resolution. Therefore, the obtained spectral information was too limited to constrain the nature of ULXs. *ASCA* , with the wide bandpass (0.5–10 keV) and moderate angular resolution ($\sim 3'$), enabled for the first time detailed spectroscopic studies of about dozen brightest ULXs (Mizuno 2000; Makishima et al. 2000; Mizuno et al. 2001), which were mostly known from the *Einstein* era. Then, the spectra of ULXs were confirmed to be generally featureless, unlike line-rich spectra of young SNRs. Furthermore, *ASCA* spectra of some ULXs have been represented successfully by the MCD model (Okada et al. 1998; Mizuno et al. 1999; Mizuno 2000; Makishima et al. 2000; Mizuno et al. 2001; Kotoku et al. 2001), On the other hand, some ULX spectra were better fitted by a PL model rather than an MCD model. These results drastically strengthened the BHB interpretation of ULXs, because the two spectral types, the MCD and PL, are exactly, what have been observed from Galactic BHBs in the soft and hard states, respectively (§§2.2.1).

Since the launch of *Chandra* and *XMM–Newton* with their excellent spatial resolution, we have become able to study a much larger number of ULXs: ULX spectra have been studied by a number of authors (e.g. Humphrey et al. 2003; Swartz et al. 2004; Feng & Kaaret 2005). Sugiho (2003) extracted X-ray spectra from about 50 ULXs, and found that some of them are successfully represented by the MCD model and others are by the PL model. This confirmed preceding studies, including those with *ASCA* .

2.5.2 Spectral transitions

Further progress in our understanding of the ULXs has been achieved with *ASCA* , through two observations of two ULXs (Source 1 and Source 2) in the spiral galaxy IC342 (Kubota et al. 2001). As illustrated in figure 2.9, in the first observation conducted in September 1993, Source 1 showed an MCD-type spectrum with $T_{\rm in} \sim 1.7$ keV

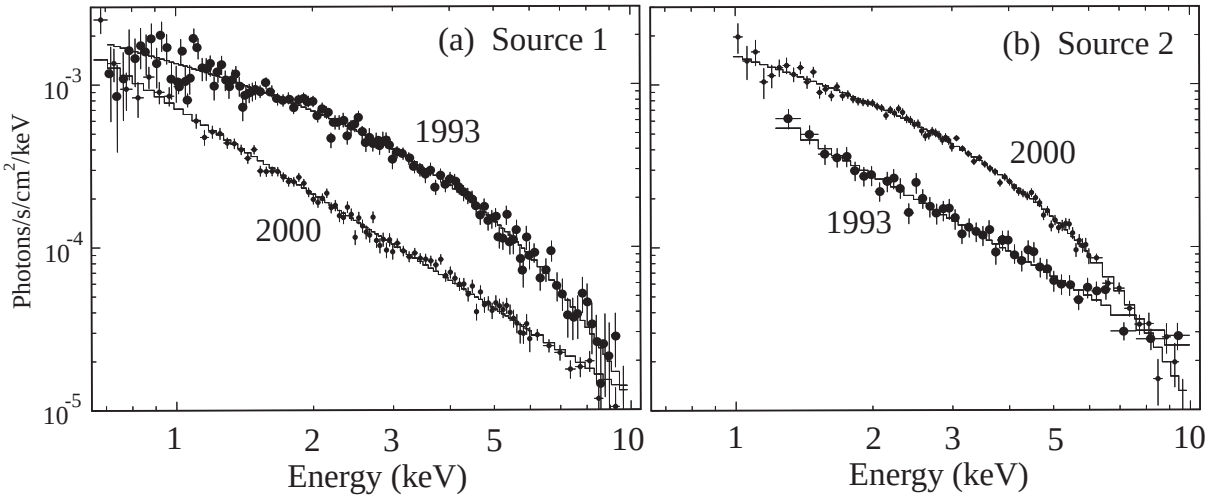

Figure 2.9: The *ASCA* spectra of IC342 Source 1 (panel a) and Source 2 (panel b) obtained in two observations (1993 and 2000). The detector response and absorption are removed, taken from Kubota et al. (2001).

and $L_{\rm X} \sim 1.9 \times 10^{40}$ erg s^{-1}, while Source 2 a quite hard spectrum represented by a power-law of photon index $\Gamma \sim 1.4$, with $L_{\rm X} \sim 0.8 \times 10^{40}$ erg s^{-1}. However, in the second observation made in January 2000, their spectral properties were nearly exchanged; Source 1 exhibited a power-law like spectrum with a lower luminosity of $L_{\rm X} \sim 0.6 \times 10^{40}$ erg s^{-1}, while Source 2 an MCD-type spectrum with $T_{\rm in} \sim 1.6$ keV and a higher value of $L_{\rm X} \sim 1.4 \times 10^{40}$ erg s^{-1}. This behavior is very reminiscent of the spectral transitions observed in Galactic BHBs between the soft state and hard state.

Similar spectral transitions have been reported for several ULXs, including in particular the object called M81 X-9 (La Parola et al. 2001, Wang 2002): it made a clear transition from a power-law type spectrum with $\Gamma \sim 1.4$ and $L_{\rm X}$(0.5–10 keV)$\sim$ 0.6×10^{40} erg s^{-1} (Ezoe et al. 2001), to an MCD-type spectrum with $T_{\rm in} = 1.24$ keV and $L_{\rm X} \sim 1.8 \times 10^{40}$ erg s^{-1}. In all these cases, ULXs exhibit higher luminosities while they are in the MCD-type state.

2.5.3 ULXs with MCD-type spectra

Although the successful MCD modeling of a significant franction of the ULX spectra obtained by *ASCA* has reinforced their BHB interpretation, there remains three funda-

mental self-inconsistencies. The first one is that the disk temperatures of ULXs ($T_{\rm in}$ = 1–2 keV; Makishima et al. 2000) are significantly higher than those of BHBs (0.5–1.2 keV; Tanaka & Lewin 1995). With the MCD formalism, equation (2.9) would then dictate that such high $T_{\rm in}$ objects should have smaller values of $R_{\rm in}$, and hence lower masses, causing a serious contradiction to the high BH mass needed to explain the high luminosities of ULXs. This problem was first pointed out by Okada et al. (1998), then by Mizuno (2000), and Makishima et al. (2001).

Another problem with ULXs was revealed through the *ASCA* observations by Mizuno (2000) and Mizuno et al. (2001). They found that some MCD-state ULXs exhibit intensity-correlated spectral changes roughly as $L_{\rm bol} \propto T_{\rm in}^2$. Such examples include IC 342 Source 1 in the 1993 observation, NGC 1313 Source B observed in 1993 and 1995, and M81 X–6 observed seven time. This scaling clearly contradicts the $L_{\rm bol} \propto T_{\rm in}^4$ relation, which has been confirmed in classical BHBs in the soft state. Since the $L_{\rm bol} \propto T_{\rm in}^4$ scaling is taken as evidence for standard accretion disks, the distinct behavior of ULXs suggests that the accretion disk is no longer in the standard state.

The last problem is related to the spectral transitions observed from some ULXs, described in the previous subsection. Although such spectral transitions are very reminiscent of those observed from a number of Galactic BHBs, the analogy involves a significant problem, as pointed out by Kubota et al. (2002) and Tsunoda et al. (2006). In Galactic BHBs, the spectral transitions between the soft and hard states are known to occur at a threshold luminosity of (0.02–0.03) $L_{\rm E}$ (Tanaka & Lewin 1995). Therefore, if these spectral transitions of ULXs are of the same origin as those of BHBs, we must conclude that these ULXs are radiating at close to the transition threshold luminosity that is extremely sub-Eddington, because the transitions of ULXs involved only factor 2–3 changes in the 0.5–10 keV luminosity. Then, we would have to conclude that the true Eddington limits of these ULXs are as high as several times 10^{41} erg s^{-1}, making the puzzle even more difficult.

It is useful here to revisit Galactic BHBs. As described in §§2.2.2, the overall behavior of BHBs in the soft state has been understood adequately in terms of the standard accretion disk. However, as mentioned in §§2.2.4, some transient BHBs in the Milky Way were discovered to violate these relations, and considered to form slim disks at their highest luminosity. Objects in the slim-disk state show relatively high inner-disk temperatures

($T_{\rm in} \sim$ 1–2 keV), and their luminosities vary apparently as $\propto T_{\rm in}^2$ (Kubota & Makishima 2004). These features resemble those observed in the MCD-type ULXs, which are the first and second self-inconsistent features when the MCD-type ULXs are interpreted as in the soft-state of BHBs. Therefore, the MCD-type ULXs are likely to be in a state which correspond to the slim-disk states of Galactic BHBs, rather than to their soft-states (Watarai et al. 2001; Ebisawa et al. 2003; Sugiho 2003). Actually, the MCD-type spectra observed from some ULXs are successfully represented by the variable-p disk model with $p \sim 0.6$ (M81 X-6, Sugiho 2003; Holmberg IX X-1, Tsunoda et al. 2006; M82 X-1, Okajima et al. 2006). Like in the case of BHBs, this property, together with the $L_{\rm bol} \propto T_{\rm in}^2$ scaling observed, strengthen the slim-disk interpretation of MCD-type ULXs.

2.5.4 ULXs with PL-type spectra

Although the slim-disk picture may thus be able to solve the first and second puzzles presented in the previous subsection, the last one still remains unsolved. This may require us to revise the assumption that the ULX transitions between the PL-type and MCD-type spectra corresponds to the high-low state transitions of classical BHBs.

As already described in §§2.2.4, a BHB does not directly evolve from the soft state into the slim-disk state, as its luminosity approached $L_{\rm E}$. Instead, an intervening state, namely the very high state (VHS), appears. In this state, the cool standard disk is still present, but its emission is strongly Comptonized into a strong spectral hard tail by a hot electron cloud. The spectrum is approximated by a dominant PL and a weak MCD. Using the *ASCA* data on the typical ULX, IC342 Source 1, Kubota et al. (2002) proposed that the PL-type ULXs correspond to the VHS of Galactic BHBs, rather than their hard (low) state. This tentative state assignment is based on the fact that the VHS spectra, when observed in a limited (e.g. 1–10 keV) energy range, are often approximated better by a power-law than by an MCD model. Because the VHS of BHBs appears near the Eddington luminosity, this assignment would explain away the third puzzle, by dictating that the observed luminosities $L_{\rm X} \sim 10^{39-40}$ erg s^{-1} of ULXs are close to their Eddington luminosity. This leads to an implicit interpretation that ULXs harbor really massive stellar BHs.

Utilizing *XMM–Newton* observations of a large number of ULXs, more detailed spectral properties of the PL-type spectra have been revealed. Miller et al. (2003; 2004a;

2004b) found that some brightest ULXs exhibit a soft excess component at the softest end of their apparently power-law shaped X-ray spectra. This could be a standard disk emission, vailed by the strong PL-like component. These soft components, when reproduced by an MCD model of cool inner-disk temperatures as $T_{\rm in} \sim 0.3$ keV. Furthermore, due to the large luminosity and the low value of $T_{\rm in}$, the inner-disk radius $R_{\rm in} \propto L^{\frac{1}{2}} T_{\rm in}^{-2}$ is obtained as rather large, e.g. $\sim 10^3$ km. Although we need a caution about large systematic errors in the estimation of $R_{\rm in}$, this suggests again rather high BH masses via equation 2.9. This structure has been confirmed with a number of typical ULXs in nearby galaxies, including two ULXs in NGC1313 (Miller et al. 2003a), four brightest ULXs in Antenna galaxies (Miller et al. 2004b), Holmberg IX X-1 (Miller et al. 2004a), NGC5204 X-1 (Roberts et al. 2005), and Holmberg II X-1 (Goad et al. 2005). Furthermore, the apparently PL-like continua (except for the soft excess) have been found to be curved, rather than extending up to higher energy ranges, as originally found in IC342 Source 1 by Kubota et al. (2003), and then in NGC1313 Source A (Dewangan et al. 2006a) and Holmberg IX X-1 (Dewangan et al. 2006b). As mentioned in §§2.2.1, Galactic BHBs also show an exponential cutoff in their hard tails, though at significantly higher energies ($\sim$ 100 keV) than that of ULXs. These cool cutoff energies of ULXs may be explained if the postulated thermal electrons, interacting with soft photons via Comptonization, have a very low temperature ($\sim$ 6 keV).

As a summary, at lower luminosity ($\sim 10^{39-40}$ erg s^{-1}) than in the MCD-type spectrum, ULXs exhibit a PL-dominant spectrum, with a weak soft excess component ($\sim$ 0.3 keV) and an exponential cutoff at $\sim$ 6 keV. If these PL-type ULXs are interpreted to correspond to the VHS of Galactic BHBs, this assignment would successfully explain their luminosities $L_{\rm X} \sim 10^{39-40}$ erg s^{-1} are close to the Eddington limit, although a cutoff energy in their spectra is significantly lower than that observed in Galactic BHBs.

2.6 X-ray Timing Properties of ULXs

ULXs often exhibit significant time variability on time scales from several hours to years, by up to a factor of ∼10, as observed from e.g., IC342 Source 1 (Okada et al. 1998), M81 X-9 (Ezoe et al. 2001), and ULXs in M51 (Terashima & Wilson 2003). As already mentioned in §2.3, these variations have demonstrated that most of them are single compact objects, rather than a sum of numerous lower luminosity objects. We believe ULXs to be variable on shorter time scales as well, but the detection is hampered by their low count rates.

2.6.1 Power Density Spectra (PDS)

The rapid X-ray variations of Galactic BHB are characterized by a power-density spectrum (PDS) which scales with frequency ν as $\propto \nu^0$ (i.e., white noise) below a certain "break" frequency $\nu_b \sim 0.1$ Hz while as $\propto \nu^{-1.5}$ above ν_c. Although these is yet no conprehensive explanation for ν_b, it is empirically believed to scale inversely with the central BH mass.

Because search for the characteristic break frequencies is a productive way of determining the nature of ULX, their PDS have been studied, in particular, with *XMM–Newton* utilizing its large photon-collecting area. Some ULXs were found to show the same characteristic PDS as observed from Galactic BHBs and AGNs, with $\nu_b \sim 28$ mHz in NGC4559 X-7 (Cropper et al. 2004), 2.5 mHz in NGC5408 X-1 (Soria et al. 2004), and 34 mHz in M82 X-1 (Dewangan et al. 2006). Since these values of ν_b are 3∼30 times lower than those ($\nu_b \sim 0.1$ Hz) measured from BHBs, we infer that these ULXs are as massive as 30∼300 $M_\odot$, if ν_b is really inversely proportional to the BH mass. However, many of other ULXs, including Holmberg IX X-1, do not have such a characteristic PDS (e.g. Mushotzky 2006).

2.6.2 Quasi-Periodic Occilations (QPOs)

A second feature of PDS that may help us understand the nature of ULXs is quasi-periodic oscillations (QPOs): these are enigmatic sharp peaks in the PSD, observed at 0.8–6 Hz from a number of BHB particularly in their VHS. Strohmayer & Mushotzky (2003) discovered ∼50–100 mHz QPOs from the brightest ULX in M82, using *XMM–Newton* and *RXTE* data. Although the origin of QPOs is not yet fixed, they are almost certainly related some physical phenomena in thin accretion disks and associated coronae

(van der Klis 1995; Di Matteo & Psaltis 1999), their detection from ULXs indicates similar disk geometries between BHBs and ULXs, and argues against the substantial radiation beaming, which is one possible explanations of ULXs (§§2.4.2). Furthermore, like the case of ν_b, the QPO frequency scales roughly as $1/M$, a mass of the order of 100–300 $M_\odot$would be needed to explain these QPOs. Later, QPO detections have also been achieved from a handful ohter ULXs including $\sim$200 mHz ones in Holmberg IX (Dewangan et al. 2006), and those with $\sim$20 mHz in NGC5408 X-1 (Strohmayer et al. 2007). Although the QPOs have yet been observed from a few ULXs so far, their energy spectra show a power-law dominant shape. These may support that ULXs with PL-type spectra are in the VHS, because QPOs from Galactic BHBs are often observed when they are in the VHS.

2.6.3 Possible orbital periodicities

Adding to the rapid variabilities described in the previous subsection, possible long periodicities have been observed from some ULXs, 106 days in M33 X-8 (Dubus et al. 1997), 30$\sim$40 hours in IC342 Source 2 (Sugiho et al. 2001), 7.5 hours in Circinus Galaxy X-1 (Weisskopf et al. 2004), 2.1 hours in M51 X-1 (Liu et al. 2002), and others. Although the exact nature of these periodicities are not yet clear, some of them could be binary (orbital) periods. According to Sugiho et al. (2001), the 30$\sim$40 hour period, if orbital, is consistent with a rather massive nature of the X-ray emitter in IC342 Source 2.

2.7 ULX Studies in Other Wavelengths

ULXs indeed release their radiative energy predominantly in the X-ray bandpass. However, their studies in other wavelengths well give us useful information on their physical nature and environment.

2.7.1 Optical identifications

If a ULX is a mass-accreting compact object, it must have a mass-donating stellar companion. The companion is likely to be a massive star, because it must have a young population signature as evidenced by the ULX environment, and it must supply the sufficient fuel to power the BH. If we could achieve a firm optical identification of a single ULX, and measured its radial velosity, we would be able to estimate the BH mass with the highest reliabitily, just as was performed on Cyg X-1 30 years ago (§§2.2.1). However, optical identifications of ULXs are difficult, because only the most luminous stars can be recognized at <15 Mpc even using the *Hubble Space Telescope* (HST), and there is often no unique optical counterpart to ULXs (Cropper et al. 2004), even within sub-arcsecond X-ray error regions

Under such difficulties, so far, several ULXs have allowed possible optical identifications. These include M81 X-6 (Liu et al. 2002), NGC 1313 X-2 (Zampieri et al. 2004), Holmberg II (Kaaret et al. 2004), and NGC 5204 X-1 (Liu et al. 2004). The colors and magnitudes of these possible counterparts indicate young massive stars, in particular O or B stars. This confirms that ULXs are very young objects. On the other hand, some ULXs have been optically identified with possible globular clusters (Wu et al. 2002; Angelini et al. 2001; Maccarone et al. 2003). There is not yet any radial velocity measurements from any of these optical counterparts.

2.7.2 Ionized nebulae

Adding to the search for counterparts of ULXs, their optical studies also inform us of environments around them. Pakull & Mirioni (2002; 2003) found that optical nebulae are associated with several brightest ULXs, including those in Holmgerg II and IX, two ULXs in NGC1313, and NGC5204 X-1. Most of the reported optical nebulae are very large $\sim$ 200–600 pc in diameter. These nebulae are estimated to be rather massive (a few handred

$M_{\odot}$), and their measured expansion velosity, typically $\sim$80 km s^{-1} imply very large kinetic energies of $\sim 10^{52-53}$ erg, much more than those of ordinary SNRs. These nebulae emit strong OIII, NeIII and HeII, as well as lower ionization lines of OI and SII. These optical emission lines are excited by either shocks, or by high energy photons via photoionization. Among these nebulae, the one associated with the ULX in the dwarf galaxy Holmberg II emits strong HeII 4686 and OI 6300 lines. Since HeII is produced by recombination, the measured line intensity requires a strong high energy source of photoionization with an isotropic luminosity of $> 3 \times 10^{39}$ erg s^{-1}. This argues strongly against the radiation beaming scenario for ULXs (§§2.4.2), because the surrounding nebulae would not be energized if their X-rays are predominantly beamed toward us.

2.7.3 Radio studies

Radio observations provide a powerful tool to achieve an excellent angular resolution, and to identify X-ray sources as SNRs, AGNs, and HII regions. Therefore, radio studies of ULXs have been conducted by several authors (e.g. Sanchez-Sutil et al. 2006; Kording et al. 2005), especially, under a speculation that unresolved, compact radio emission is consistent with beaming toward the observer, whereas extended emission rules out this possibility. Using *Australia Telescopes Compact Array* (ATCA), Kaaret et al. (2003) detected radio emissions from a bright ULX in the dwarf galaxy NGC5408. They suggested that the detected radio emission is probably from a relativistic jet, and the X-rays from this ULX could be a result of inverse-Compton scattering of visible photons form the companion by electron in the jet. On the other hand, Mushotzky (2004) searched several ULXs for radio counterparts using the *Very Large Array* (VLA) data, and found that a significant fraction of the suggested radio counterparts to the ULX sources are resolved rather than point-like. This provides a strong argument against the relativistic beaming models. Furthermore, they found that their radio, optical, and X-ray flux ratios are not like those of most Bl Lac objects; this also weaken the beaming scenario.

2.8 ULXs and the Present Thesis

2.8.1 A tentative scenario

Given the overview of ULXs, we begin their research utilizing the latest X-ray data. For that purpose, we employ the IMBH scenario as the most promising working hypothesis among the three possible explanations for ULXs; the IMBH scenario (§§2.4.1), the beamed emission scenario (§§2.4.2), and the super-Eddington emission scenario (§§2.4.3). This standpoint is based on the following four reasons.

1. ULXs with the MCD-type spectra are considered to correspond to the slim-disk state of Galactic BHBs, because of the successful spectral modeling with $p \sim 0.6$ and the $L \propto T_{\rm in}^2$ behavior. Although the mass accretion rate may well be super critical in the slim-disk state, the X-ray luminosity is considered not to largely exceed $L_{\rm E}$, as represented by figure 2.10 where the luminosity of XTE J1550−564 is seen to saturate, in its slim-disk state, at $\sim 5 \times 10^{38}$ erg s^{-1} ; this is $\sim 0.5 L_{\rm E}$. Then, ULXs are also considered to be sub-Eddington, or at most, mildly super-Eddington.

2. The properties observed from PL-type ULXs are thought to correspond to those of Galactic BHBs in the VHS. Therefore, the emission is again considered sub-Eddington.

3. The QPOs observed from ULXs have significantly lower frequencies from BHB, thus suggesting much higher masses than ordinary stellar BHs.

4. The large and energetic optical nebulae, associated with many ULXs, suggest that the ULXs radiate isotropically; this argues strongly against the radiation beaming scenario.

2.8.2 How to make ULXs?

In order to complement our standpoint as presented above, we need to explain whether such IMBHs can really be formed by some plausible mechanisms. Although this is somewhat beyond the scope of the present thesis, we may briefly mention two possible scenarios.

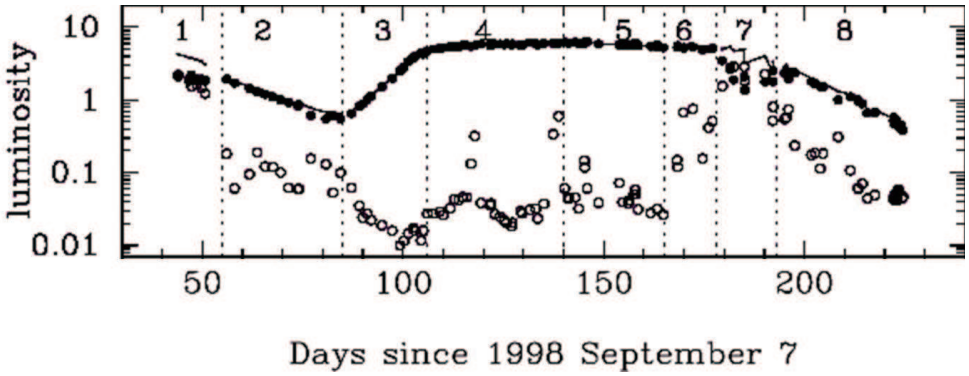

Figure 2.10: Luminosity evolution of the transient BHB XTE J1550−564 from Kubota et al. (2004), in units of 10^{38} erg s^{-1} . Luminosities of the MCD and PL components, and their sum, are shown with filled circles, open circles, and solid line, respectively. Periods 4 through 6 are identified with the slim-disk state.

One is the picture proposed by e.g. Ebisuzaki et al. (2001); in dense stellar clusters, massive stars would merge together to form an unusually massive single star. If this process proceeds fast enough, the object would collapse into a massive BH before the progenitor evolves along the ordinary stellar evolution tracks and loses its mass into stellar winds.

The other is growth via accretion. As widely known, the mass of any BH will grow exponentially on a time scale of 4×10^8 year, if the mass accretion at the Eddington rate is sustained. Let us suppose that an ordinary-mass stellar BH forms a close companion with a massive (say, $40 M_\odot$) star, and swallows the gas from it at a 20 times the Eddington rate. Then, the BH mass would be tripled in 10^7 year on which the companion evolves, but the emergent X-ray luminosity would be nearly saturated at most a few times $L_{\rm E}$, as suggested by figure 2.10.

A natural consequence from both these two scenarios is that the resulting BH should be rapidly spinning. This may revive the Kerr-BH scenario of ULXs, as first suggested by Makishima et al. (2000), and subsequently reinforced by a *Suzaku* observation of a transient ULX in NGC4945 (Isobe et al. 2007).

2.8.3 Objectives of the present thesis

Our IMBHs scenario has been strengthened by the recent studies. However, the other alternatives have not been ruled out yet. This is because ULXs are much ($\sim 10^3$ times) farther than Galactic BHBs, so that the available X-ray spectra are of much poorer quality, and their detection has been limited to < 10 keV. Furthermore, the number of observations of each source remained rather small, and hence the study of spectral changes was limited.

In the present thesis, we challenge the above limitations from two aspects. One is to utilize a large amount of archival data from the European *XMM–Newton* satellite, which has been in orbit for nearly 8 years. We can now study luminosity-related spectral changes of a fair number of ULXs. The other is to utilize our *Suzaku* , which allows us wide-band observations with an unprecedented sensitivity.

Chapter 3

INSTRUMENTATION

3.1 *XMM–Newton*

3.1.1 An overview

The *XMM–Newton* satellite of the European Space Agency (ESA), with *XMM* standing for X-ray Multi-Mirror Mission, is the second "cornerstone" missions defined in the Horizon 2000 Programme. It was launched on 1999 December 10 by an Ariane-5 rocket, and was placed in a highly elliptical orbit of 47.8 hours period, 7000 km perigee and 114000 km apogee. As an imaging spectroscopic cosmic X-ray sutellite working over an energy range of 0.2–10 keV, *XMM–Newton* is designed to provide a large photon-collecting area of $\sim$2000 cm^2 (combined with focal-plane instruments at 1.5 keV), together with a good angular resolution of 15″ (half power diameter). Is also has a high ($E/\Delta E$ $\sim$300) and moderate ($E/\Delta E$ $\sim$20–50) energy resolutions utilizing reflecting gratings (0.3–2.5 keV) and X-ray CCDs at 0.2–10 keV, respectively, where E is the X-ray energy and ΔE is the energy resolution. It can also conduct simultaneous optical/UV observations.

We present a schematic drawing of in-orbit configuration of *XMM–Newton* in figure 3.1. It weighs $\sim$3800 kg and its focal length is $\sim$7.5 m. It is equipped with three X-ray telescopes, each coupled on the focal plane to one of three CCD camera arrays called European Photon Imaging Camera (EPIC) for X-ray imaging spectroscopy. Is also has a 30 cm optical/UV telescope, called Optical Monitor (OM). Two of the three CCD cameras utilize Metal Oxide Semi-conductor type CCDs (EPIC MOS), while the other p-n junction type ones (EPIC PN). Just behind each of the two X-ray telescopes coupled to

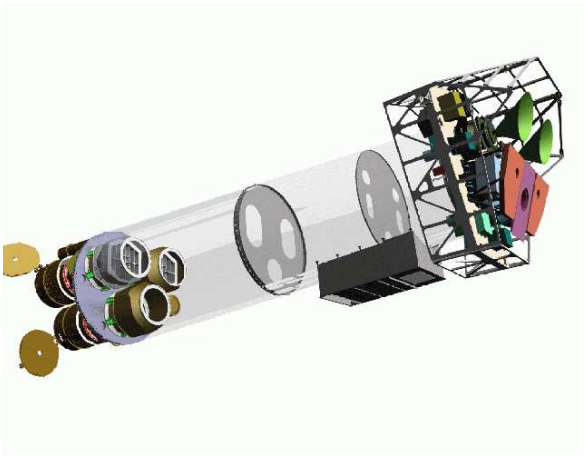

Figure 3.1: A sketch of the *XMM–Newton* payload. The mirror modules, two of which are equipped with RGS, are visible at the lower left. At the right end of the assembly, the focal X-ray instruments, the EPIC MOS cameras, the EPIC pn camera and the RGS detectors, are shown. The OM telescope is obscured by the lower mirror module.

the EPIC MOS, a reflective grating (Reflection Grating Spectrometer, RGS) is fixed, by which incident X-rays are dispersed and detected by two other CCD (MOS type) arrays in a off-focal plane. In subsequent sections, we describe characteristics of the X-ray telescope (§§3.1.2), and the EPIC (§§3.1.3), which are involved in the present thesis.

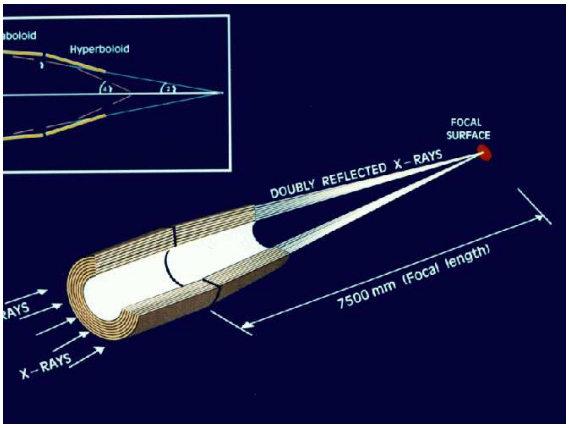

Figure 3.2: A half-cut view of an X-ray telescope onboard *XMM–Newton* , and its light path.

3.1.2 X-ray telescopes

The three X-ray telescopes onboard *XMM–Newton* reflect incoming X-rays with energies up to ∼10 keV, and produce X-ray images on the respective focal planes. Each of them consists of 58 pairs of Wolter-I grazing-incident mirror shells which are nested in a coaxial and co-focal configuration. The design of the optics was driven by the requirement of obtaining the largest possible effective area over a wide range of energies. Mirrors were replicated from super-polished gold-coated mandrels using a nickel electroforming technique. The telescopes focal length is 7.5 meters and the diameter of the largest mirrors is 70 cm. As shown in figure 3.2, one telescope is designed to work with the PN camera on the focus. The two others have grating assemblies in their light paths, where about 44% of the incoming X-rays passes to the primary MOS focus while 40% of the incident light is intercepted by grating plates of the RGS. The three telescopes are otherwise identical.

Figure 3.3 shows the imaging characteristics of the *XMM–Newton* X-ray telescopes. For on-axis sources, high energy photons are reflected and focused predominantly by the inner shells of the X-ray telescope, which apparently give better focus than the average of all shells. As a result, the fractional encircled energy increases with the increasing photon energy. The half power diameter is 15″.1 for EPIC PN, 13″.6 for EPIC MOS1, and 12″.8 for MOS2. This difference is mainly related to individual performance of the X-ray telescopes.

Figure 3.4 left panel shows the spectral effective areas of the X-ray telescopes with

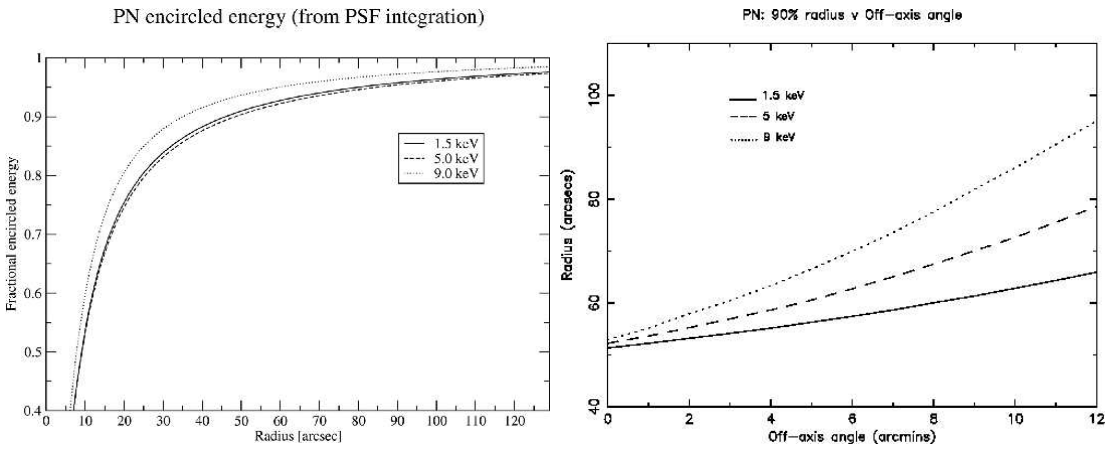

Figure 3.3: (left) The PN fractional encircled energy as a function of the angular radius (on-axis) at different energies. (right) The 90% energy encircled radius of a point source observed with the PN camera as a function of the off-axis angle at different energies.

all instruments. The sharp decrease in these effective areas above $\leq$10 keV is due to the fact that the total reflection by the mirror shells hit the critical angle at energies up to $\sim$10 keV (depending on the shell nesting position). The feature near 2 keV is due to Au M-edge of the telescopes. The effective area of EPIC MOS is less than half that of EPIC PN, because of the presence of the reflecting gratings. As presented in the right panel of figure 3.4, the telescope effective area decreases the incident angle (measured from the optical axis) increases. This property, called "vignetting", is rather severe. At the edge of the FOV ($\sim$30$''$) which is defined by CCD's physical size, the effective area thus decreases to $\sim$30% of the on-axis value.

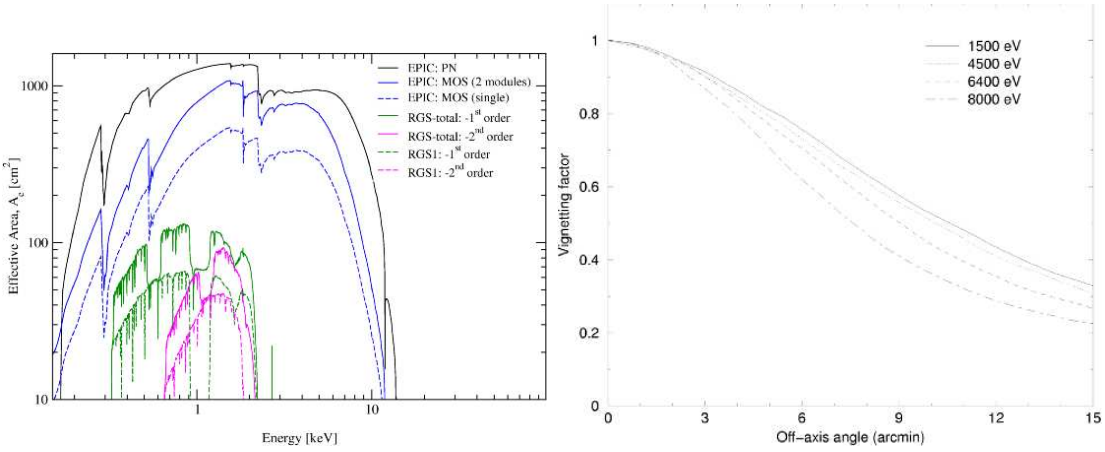

Figure 3.4: (left) The net effective area of all *XMM–Newton* X-ray telescopes, when coupled to the EPIC and RGS. (right) Vignetting function as a function of the off-axis angle (0′–15′, based on simulations), at a few selected energies, of the X-ray telescope in front of the PN camera.

3.1.3 European photon imaging camera (EPIC)

We show in figure 3.5 the focal-plane arrangement of the two type of EPIC, MOS and PN. The two EPIC MOS cameras, MOS1 and MOS2, are rotated by 90° with respect to each other. Each MOS camera consists of 7 front-illuminated CCD chips of 600×600 pixels each. The PN camera utilizes an array of 2×6 back-illuminated CCDs, each having 200×64 pixels. The pixel size of PN CCDs, 150 μm, is larger than that of the MOS CCDs, 40 μm. The readout of the PN chips is much faster than that of the MOS cameras, because each pixels column has its own readout node. The two types of instruments cover roughly the same FOV of ∼30′ in diameter.

In order to suppress the contamination of infrared, visible and ultraviolet photons to which the EPIC CCDs are also sensitive, the EPIC camera incorporate aluminized optical blocking filters. The filters are selective among 3 separate types, “thick”, “medium”, and “thin”. The influence of the filter to the low-energy effective area is illustrated in figure 3.6. Since the PN CCDs are back-illuminated and have thicker depletion layers, they yield a higher quantum efficiency than the MOS chips.

The nominal operating mode of the EPIC is called Full frame mode, which provides imaging spectroscopy over the FOV of 30′ diameter, using full pixels of all CCDs. The

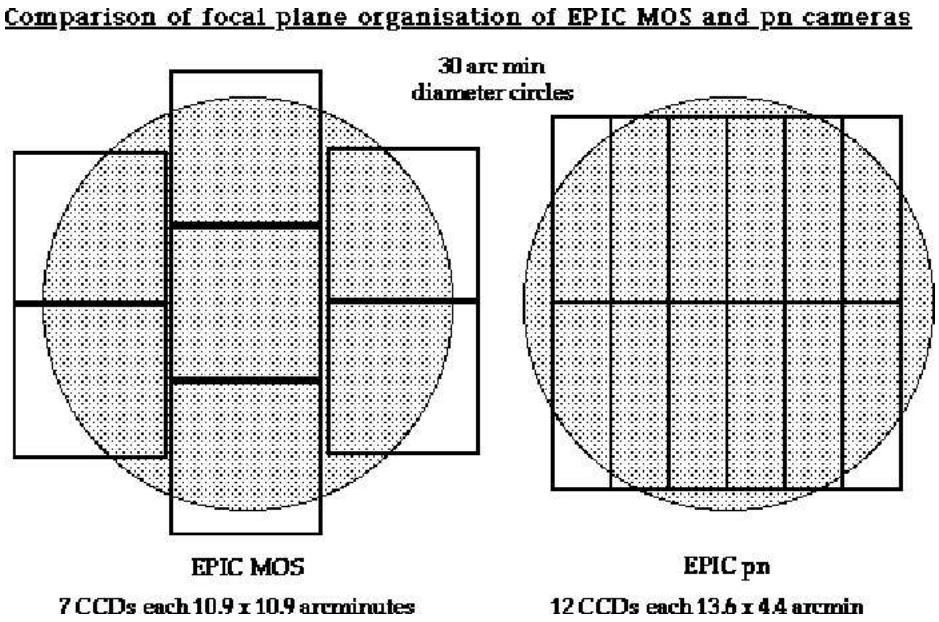

Figure 3.5: A rough sketch of the field of view of the two types of EPIC cameras; MOS (left) and PN (right). The shaded circle depicts a 30′ diameter area.

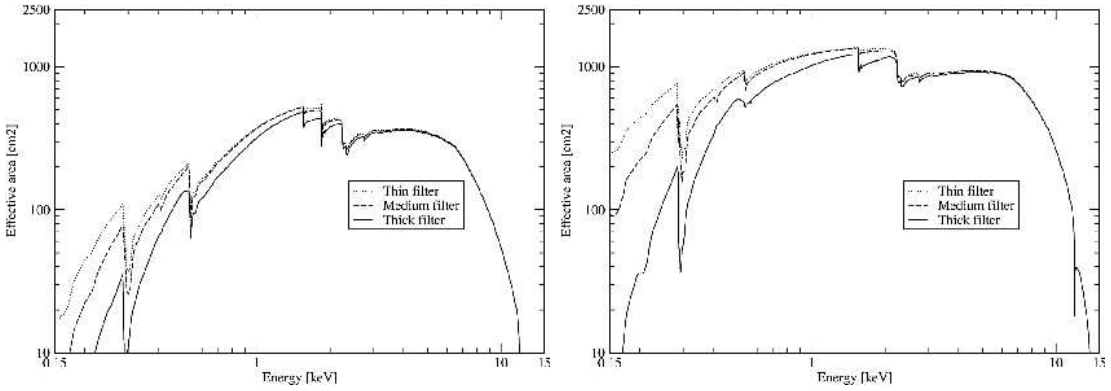

Figure 3.6: The effective areas of EPIC MOS (left) and PN (right), for each of the optical blocking filters.

Table 3.1: Basic numbers for the science modes of EPIC.

MOS (central CCD; pixels)	Time resolution	Max. count rate[a]
Full frame (600×600)	2.6 s	0.70
Large window (300×300)	0.9 s	1.8
Small window (100×100)	0.3 s	5
Timing (100×600)	1.75 ms	100
PN (central CCD; pixels)		
Full frame (376×384)	73.4 ms	6
Large window (198×384)	48 ms	10
Small window (63×64)	6 ms	100
Timing (64×200)	0.03 ms	800

[a] The count rate where the pile-up fraction is ∼1% for a point source.

central CCD of the MOS and all chips of the PN allow several other modes of data acquisition, partial window and timing (non-imaging) mode, to provide a finer time resolution and capability to avoid the pile-up. The basic operating modes are summarized in table 3.1. We can independently choose the operating modes of MOS and PN.

In figure 3.7, we show the spectral resolution of EPIC MOS and PN after corrections for "charge transfer inefficiency (CTI)", namely partial loss of charges during its transfer. The energy-resolving power of these cameras is determined by the intrinsic energy resolution of the individual pixels. The energy resolution of MOS (∼70 eV at 1 keV) has degraded approximately by 13% since the launch, while that of the PN camera has been stable, retaining an FWHM resolution of ∼80 eV at 1 keV.

As shown in figure 3.8, the EPIC background light curves during the observation often exhibit "flaring" behavior characterized by strong and rapid variability, due to charge particles. As studied by Japanese users (Katayama et al. 2004), the remaining "quiescent" background component is stable within ∼10%. In the analysis, we discard time regions where the background flares are observed. Figure 3.9 shows the quiescent background spectra of the MOS and PN, the counting rate of which becomes ∼0.5 counts s^{-1}/chip.

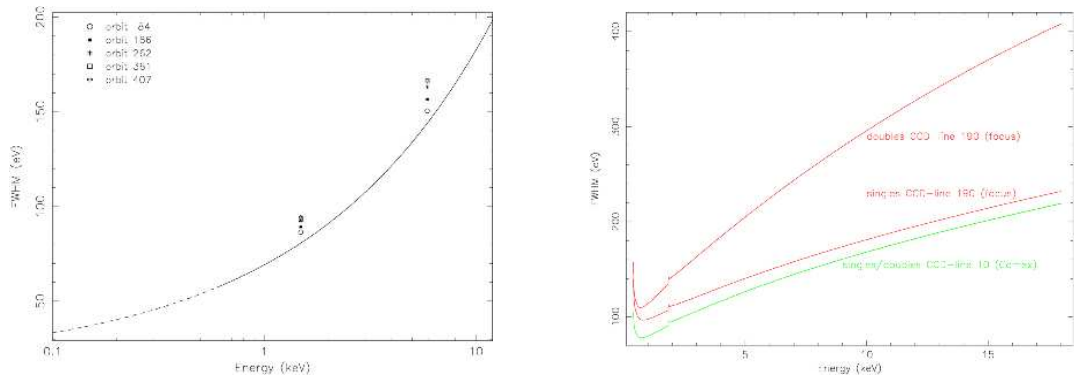

Figure 3.7: (left) The EPIC MOS energy resolution (FWHM) as a function of energy. The solid curve is a best-fit $E^{0.5}$ function to ground calibration data between 0.1–12.0 keV, together with the plots of the measured in-flight FWHM of the Al Kα (1.487 keV) and Mn Kα (5.893 keV) lines. (right) That of EPIC PN, where curves are given for single and double events (full frame mode) at the focus position as well as at a position 10 pixels away from the readout node.

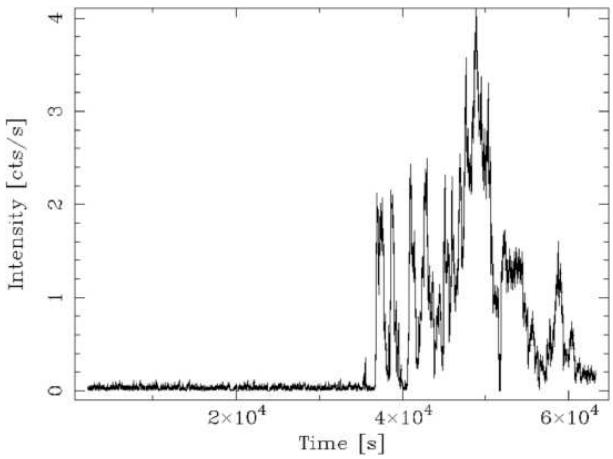

Figure 3.8: A lightcurve from a MOS1 observation badly affected by soft proton flares.

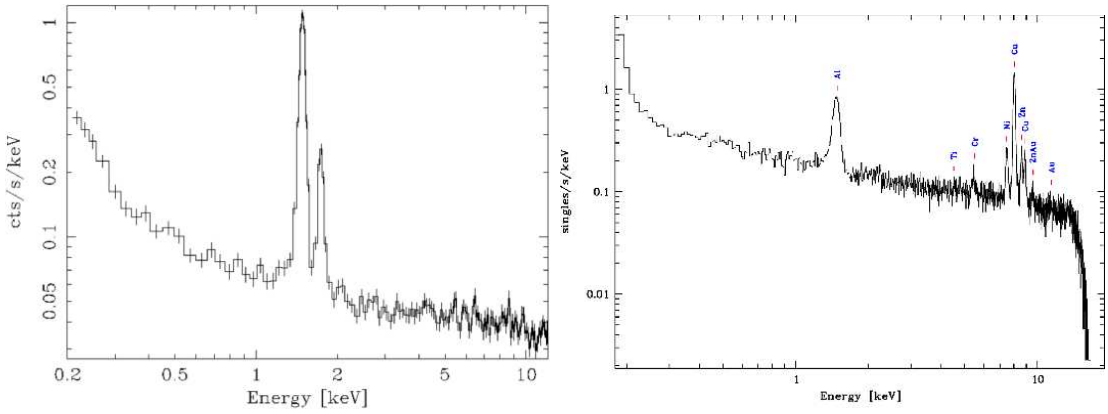

Figure 3.9: Background spectra of the MOS (left) and PN (right) cameras during an observation with the filter wheel closed. The line features are due to fluorescence from materials surrounding the detectors.

3.2 *Suzaku* Satellite

3.2.1 An overview

The scientific satellite *Suzaku* (Mitsuda et al. 2007) is the Japanese fifth X-ray astrophysical mission, following *Hakucho* (1979), *Tenma* (1983), *Ginga* (1987), and *ASCA* (1993). *Suzaku* , also called *Astro-EII*, is a project of the Institute of Space and Astronautical Science (ISAS/JAXA), developed under a Japan-US collaborations, and is a re-challenge mission of *Astro-E* which was launched by the M-V rocket unit no.4 on 2000 February 10 but failed in orbit injection by the combustion disorder of the first step rocket. The satellite was launched on 2005 July 10 with the M-V rocket unit no.6 from the Uchinoura Space Center (USC) of ISAS/JAXA at Kagoshima, and successfully thrown into a near-circular orbit with an apogee of 568 km, an inclination of 31.9 degrees, and an orbital period of about 96 minutes.

We show a schematic view of *Suzaku* in figure 3.10, which weighs about 1680 kg and has an octagonal-shaped body of a 2.1 m diameter and a height of 6.5 m with an extendible optical bench (EOB). At the top of the EOB, five sets of X-ray telescopes (XRTs, Serlemitsos et al. 2007) are placed. One of the five XRTs is dedicated for an X-ray micro calorimeter (X-ray Spectrometer, or XRS, Kelley et al. 2007) settled on its focal-plane, which is no longer operational due to lost of liquid helium to cool the device.

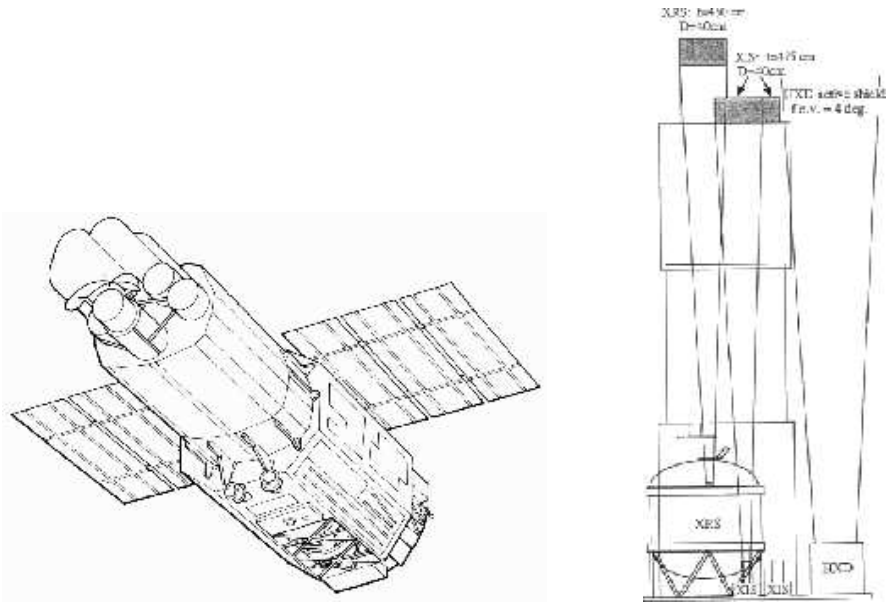

Figure 3.10: (left) A schematic picture of the bottom of the *Suzaku* satellite in orbit. Both solar paddles and the EOB are deployed. On the top, the XRT-S for the XRS, and the four XRT-Is for the XISs can be seen. (right) A side view of the instrument and telescopes on *Suzaku* .

The other four XRTs are aligned along the satellite Z axis with a common focal length of 4.75 m and four X-ray sensitive imaging CCD cameras (X-ray Imaging Spectrometers, or XISs, Koyama et al. 2007) are settled on their focal-planes, which consist of three front-illuminated (FI; energy range 0.4–12 keV) and one back-illuminated (BI; energy range 0.2–12 keV). There is the non-imaging, collimated Hard X-ray Detector (HXD, Takahashi et al. 2007; Kokubun et al. 2007), which extends the bandpass of the observatory to much higher energies with its 10–600 keV pointed bandpass. With these instruments *Suzaku* can provide high-quality spectra simultaneously in a wide energy range of 0.2–600 keV.

3.2.2 X-ray telescope (XRT)

X-Ray Telescopes (XRTs) on board *Suzaku* have been developed jointly by NASA/GSFC, Nagoya University, Tokyo Metropolitan University, and ISAS/JAXA. The XRTs are arranged on the EOB on the spacecraft in the manner shown in the left panel of figure 3.11, and consist of five telescopes, four of which (XRT-I) are used on the XIS and the other one (XRT-S) is for the XRS. Parameters of XRTs are summarized in table 3.2.

The XRTs are grazing-incidence reflective Wolter-I type optics, which consist of closely nested thin-foil reflectors, reflecting X-ray at small grazing angles. As shown in the right panel of figure 3.11, an XRT is a cylindrical structure, and are composed of thermal shields at the entrance aperture to help maintain a uniform temperature, pre-collimators mounted on metal rings for stray light elimination, primary stages for the first X-ray reflection, secondary stages for the second X-ray reflection, and base rings for structural integrity and interface with the EOB of the spacecraft. All these components, except the base rings, are constructed in 90° segments. Four of these quadrants are coupled together by interconnect-couplers and also by the top and base rings. The telescope housings are made of aluminum for an optimal strength to mass ratio. Each reflector consists of a substrate also made of aluminum and an epoxy layer that couples the reflecting gold surface to the substrate. With radii extending approximately from 60 mm at the inner part to 200 mm at the outer part, the reflectors are nominally 178 μm in thickness and positioned with grooved alignment bars, which hold the foils at their circular edges. The pre-collimators, which block off stray light that otherwise would enter the detector at a larger angle than intended, consist of concentrically nested aluminum foils similar to that of the reflector substrates, and installed on top of their respective primary reflectors along the axial direction. They are shorter, 22 mm in length, and thinner, 120 micrometers in thickness. The thermal shields, designed to function in a thermal environment of 20 ± 7.5°C, are integrated on top of the pre-collimator stage to provide the needed thermal control.

The XRTs provide large effective area in the energy range of 0.2–12 keV, typically 440 cm^2 at 1.5 keV and 250 cm^2 at 8 keV with a field of view (FOV) for XRT-Is of about $17'$ at 1.5 keV and $13'$ at 8 keV. Figure 3.12 shows the total effective area of the XRT combined with the XIS, which includes features due to the elemental composition of the XIS and XRT. K-shell absorption edges from the oxygen (0.54 keV) and aluminum (1.56 keV) in the blocking filters are present, as well as a number of weak M-shell features between 2–3

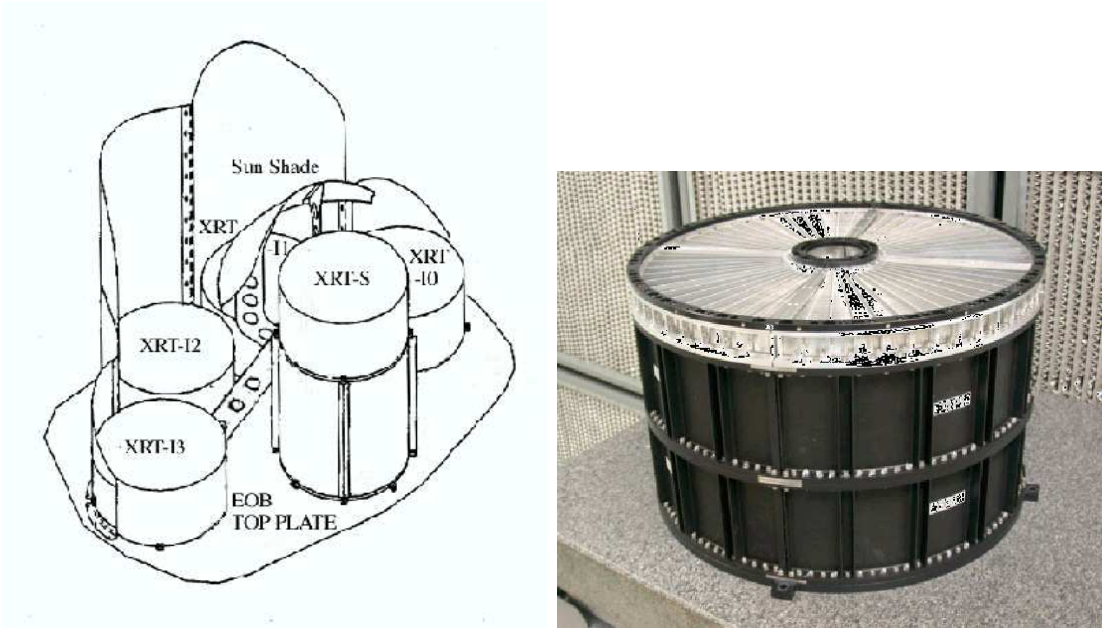

Figure 3.11: A layout of the XRTs on the *Suzaku* spacecraft (left) and an overview picture of the XRT (right).

Table 3.2: Parameters of *Suzaku* XRTs.

Focal length	4.75 m
Outer (Inner) Diameter	399 (118) mm
Height	279 mm
Mass/Telescope	19.5 kg
Geometric area/Telescope	873 cm^2
Reflecting surface	Gold
Substrate material	Aluminum
Substrate thickness	155 μm
Field of View	$17'$ at 1.5 keV $13'$ at 8 keV
Effective Area	440 cm^2 at 1.5 keV 250 cm^2 at 8 keV
Angular Resolution	$\sim 2'$ (HPD)

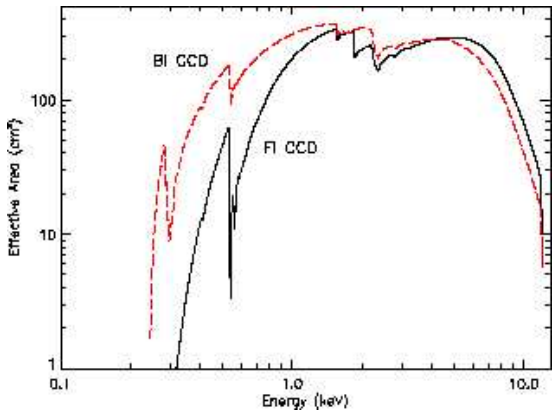

Figure 3.12: The effective area of one XRT + XIS system, for both the FI and BI chips.

keV arising from the gold in the XRT. The effective area of the four XRT modules at 7 keV is comparable to that of *XMM–Newton* mirrors, although the total weight is much smaller.

We show in figure 3.13 the vignetting curves calculated by the ray-tracing simulator, compared with the observed intensities of the Crab nebula at various off-axis angles. The abrupt drop of the model curves at $\sim 8'$ is due to the source approaching the detector edge. The observed vignetting is consistent with calculation within $\sim$10%.

Figure 3.14 shows the encircled-energy function (EEF) of one of the typical XRT quadrants at different energies measured at a beam line. The angular resolutions of the XRTs are $\sim 1.9'$ expressed in terms of half-power diameter (HPD), and they do not significantly depend on the energy of the incident X-ray in the energy range of *Suzaku* 0.2–12 keV. In the in-flight imaging calibration, the HPDs are in the range of $1'.8$–$2'.3$, which are consistent with that from the ground-based calibration.

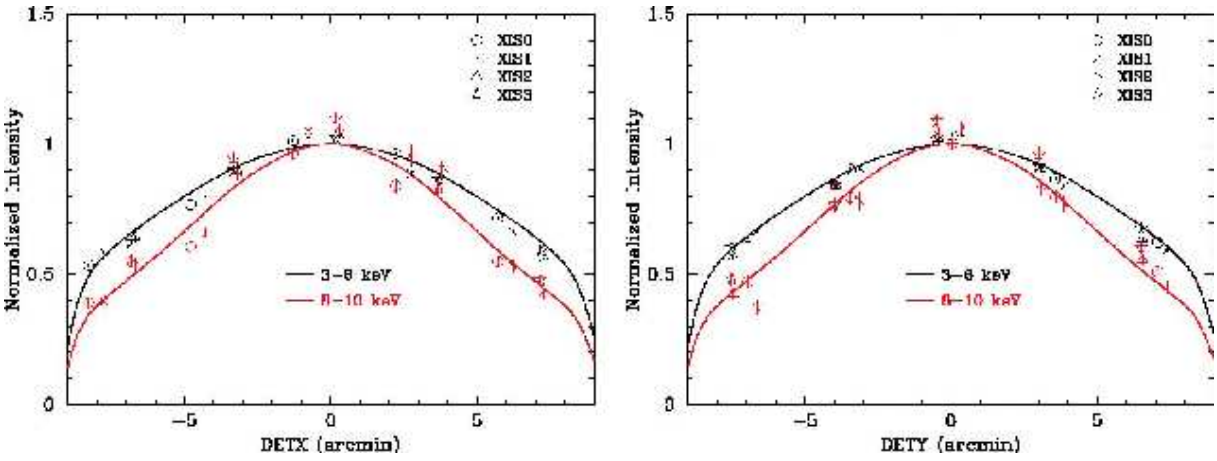

Figure 3.13: Vignetting of the four XRT-I modules using the data of the Crab nebula in the two energy bands 3–6 keV and 8–10 keV. The model curves are calculated with the ray-tracing simulator with the spectral parameters of the Crab nebula.

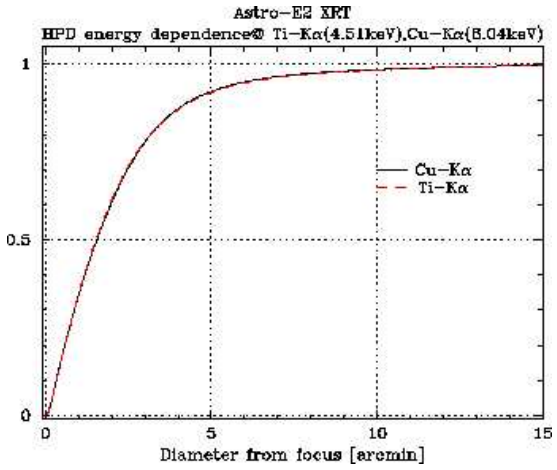

Figure 3.14: The EEF showing the fractional energy within a given radius for one quadrant of the XRT-I telescopes on *Suzaku* at 4.5 and 8.0 keV.

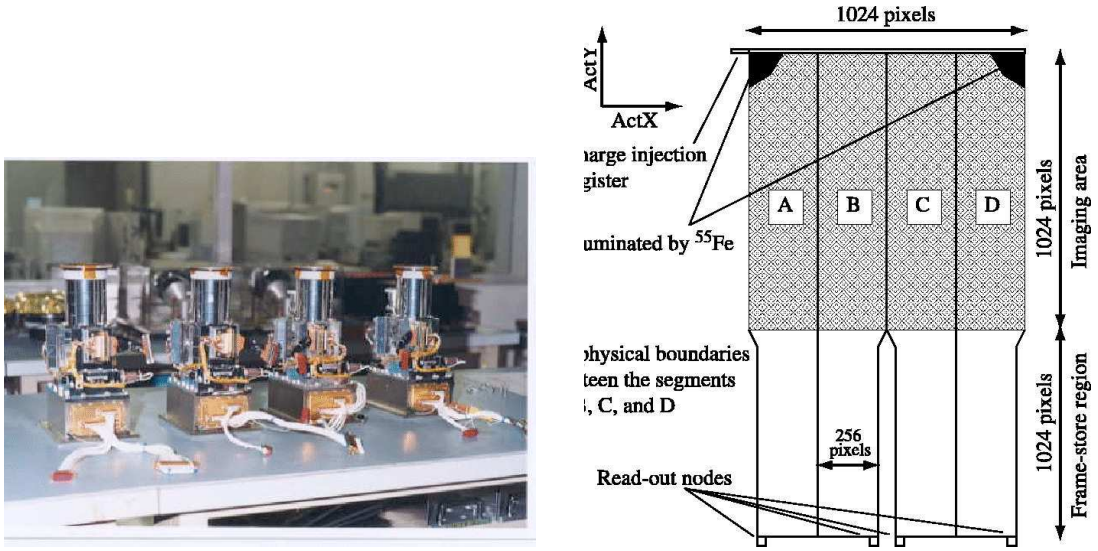

Figure 3.15: (left) The four XIS detectors before installation onto *Suzaku* . (right) Schematic view of the XIS CCD (top view). The CCD consists of four segments (A, B, C, and D), each with a dedicated read-out node.

3.2.3 X-ray imaging spectrometer (XIS)

Suzaku has four X-ray Imaging Spectrometers (XISs), which are shown in figure 3.15. These employ X-ray sensitive silicon charge-coupled devices (CCDs), which are operated in a photon-counting mode, similar to that used in the *ASCA* SIS, *Chandra* ACIS, and *XMM–Newton* EPIC. X-ray CCDs operate by converting an incident X-ray photon into a charge cloud, with the magnitude of charge proportional to the energy of the absorbed X-ray. The four *Suzaku* XISs are named XIS0, 1, 2 and 3, each located in the focal plane of an X-ray Telescope; those telescopes are known respectively as XRT-I0, XRT-I1, XRT-I2, and XRT-I3. As shown in table 3.3, each CCD camera has a single CCD chip with an array of 1024×1024 picture elements ("pixels"), and covers an region on the sky. Each pixel is 24 μm square, and the size of the CCD is 25×25 mm^2. One of the XISs, XIS1, uses a back-side illuminated CCD, while the other three use front-side illuminated CCDs. The XIS has been developed jointly by Kyoto University, Osaka University, Rikkyo University, Ehime University, ISAS, and MIT.

In order to reduce the total amount transmitted to ground, the CCD data are processed on-board. There are two clocking modes of Normal and Parallel Sum. In Normal mode,

Table 3.3: An overview of Suzaku XIS capabilities.

Field of View	$17.8' \times 17.8'$
Bandpass	0.2-12 keV
Pixel grid	1024×1024
Pixel size	24 μm× 24 μm
Energy Resolution	$\sim$ 130eV at 6 keV
Effective Area	340 cm^2 (FI), 390 cm^2 (BI) at 1.5 keV
(incl XRT-I)	150 cm^2 (FI), 100 cm^2 (BI) at 8 keV
Time Resolution	8 s (Normal mode), 7.8 ms (P-Sum mode)

two options (Window and Burst) may be used in combination with the Normal Mode. If neither Window nor Burst option is specified, the exposure time is 8 seconds, and all the pixels on the CCD are read out every 8 seconds. This can be combined with either of the 5×5, 3×3, and 2×2 editing modes. Parallel Sum mode can be used only with the Timing Editing mode, and the Y coordinate is used to determine the event arrival time. As a result, no spatial resolution is available in the Y-direction. The time resolution of the Parallel Sum Mode is 8 s/1024 7.8 ms. Table 3.4 indicates how the effective area and exposure time are modified by the Burst and Window options. In the Normal Clock mode, the Window and Burst options can modify the effective area and exposure time, respectively. The two options are independent, and may be used simultaneously.

We can use three observation modes (5×5, 3×3, and 2×2) are usable in normal modes, and only the timing mode in the P-Sum mode. We show in figure 3.16 the pixel pattern whose pulse height or 1-bit information is sent to the telemetry. In 5×5 mode, all the pulse heights of the 25 pixels centered at the event center are sent to the telemetry. This is used with the Normal Clock mode, and in 3×3 mode, pulse heights of the 9 pixels centered at the event center are sent to the telemetry with the 1-bit information (pulse height larger than the Split Threshold Outer or not) for the surrounding 16 pixels. This is used with the Normal Clock mode. In 2×2 mode, the central 4 pixels are selected to include the second and the third (or fourth) highest pixels among the 5 pixels in a cross centered at the event center.

All four XISs have low backgrounds, due to a combination of the Suzaku orbit and

Table 3.4: The effective area and exposure time for different burst and window options.

Option	Effective area	Exposure time
None	1024×1024	8 s
Burst	1024×1024	$(8/2^n)$ s ×1 exposure
Window	256×1024	2 s ×4 exposure
	128×1024	1 s ×8 exposure
Burst & Window	256×1024	$(2/2^n)$ s ×4 exposure
	128×1024	$(1/2^n)$ s ×8 exposure

n is an integer.

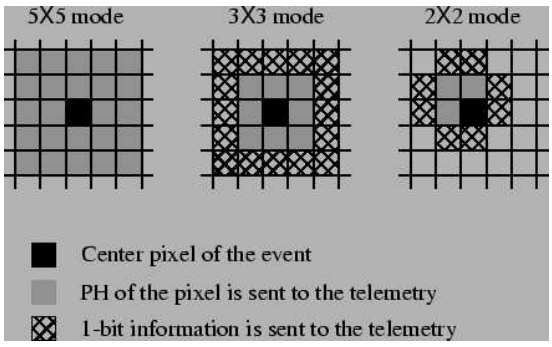

Figure 3.16: Information sent to the telemetry is shown for 5×5, 3×3, and 2×2 modes. 1-bit information means whether or not the PH of the pixel exceeds the outer split threshold.

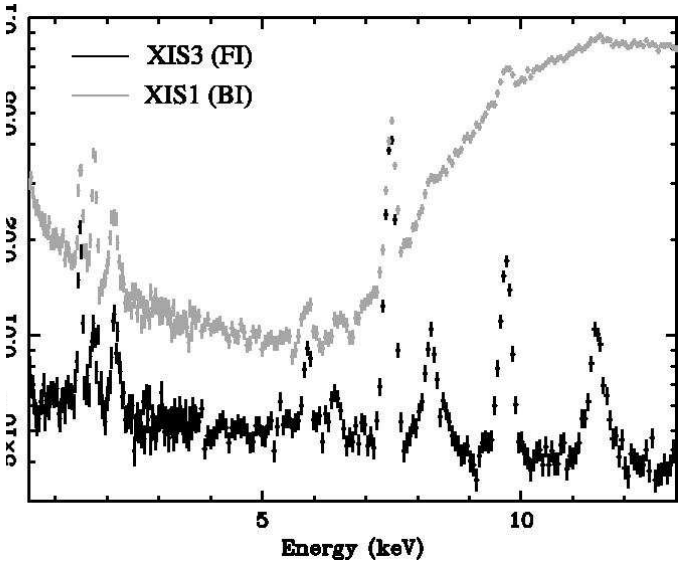

Figure 3.17: The night Earth spectra with the FI and BI CCDs.

the instrumental design. The background originates from the cosmic X-ray background (CXB) combined with charged particles (the non-X-ray background, or NXB). When observing the dark earth (i.e. the NXB), the background rate between 0.4–12 keV in is 0.1–0.2 cts/s in the FI CCDs and 0.3–0.6 cts/s in the BI CCD. We show in figure 3.17 the NXB spectra for each sensor. There are also fluorescence features arising from the calibration source as well as material in the XIS and XRTs.

3.2.4 Hard X-ray detector (HXD)

The Hard X-ray Detector (HXD), shown in figure 3.18, is a non-imaging, collimated hard X-ray scintillating instrument sensitive in the ∼10 keV to ∼600 keV band. It has been developed jointly by the University of Tokyo, Aoyama Gakuin University, Hiroshima University, ISAS/JAXA, Kanazawa University, Osaka University, Saitama University, SLAC, and RIKEN. Its main purpose is to extend the bandpass of the *Suzaku* observatory to the highest feasible energies, thus allowing broad-band studies of celestial objects.

The HXD sensor (HXD-S) is a compound-eye detector instrument, consisting of 16 main detectors (arranged as a 4×4 array) and the surrounding 20 crystal scintillators for active shielding. Each unit actually consists of two types of detectors: a GSO/BGO phoswich counter, and 2 mm-thick PIN silicon diodes located inside the well, but in front of the GSO scintillator. The PIN diodes are mainly sensitive below ∼60 keV, while the GSO/BGO phoswich counter (scintillator) is sensitive above ∼40 keV. The scintillator signals are read out by photomultiplier tubes (PMTs). The schematic drawing of the HXD is given in figure 3.18. The HXD features an effective area of ∼160 cm^2 at 20 keV, and ∼260 cm^2 at 100 keV, shown in figure 3.19. The energy resolution is ∼4.0 keV (FWHM) for the PIN diodes, and $7.6/\sqrt{E}\%$ (FWHM) for the scintillators where E is energy in MeV, and the time resolution is 61 μs. We show the HXD capabilities in table 3.5.

Each main detector unit is of a well-type design with active anti-coincidence shields. The shields and the coarse collimator itself are made of Bismuth Germanate (BGO; $Bi_4Ge_3O_{12}$) crystals, while the X-ray sensing material "inside the well" is GSO (Gadolinium Silicate, or $Gd_2SiO_5(Ce)$) crystal. Each unit thus forms a 2 × 2 matrix, containing four 24 mm × 24 mm, 5 mm thick GSO crystals, each placed behind the PIN diode. The BGO crystals are also placed underneath the GSO sensors, and thus each well is a five-sided anti-coincidence system.

The low energy response of the HXD is provided by 2 mm thick PIN silicon diodes, placed in front of each GSO crystal. The geometrical area of the diode is 21.5 × 21.5 mm^2, while the effective area is limited to be ∼16.5 × 16.5 mm^2 by the guard ring structure. The PIN diodes are of course also actively shielded from particle events by the BGO shields, as they are placed inside the deep BGO wells. In addition, to reduce the contamination by the cosmic X-ray background, passive shields called "fine collimators", made of 50 μm

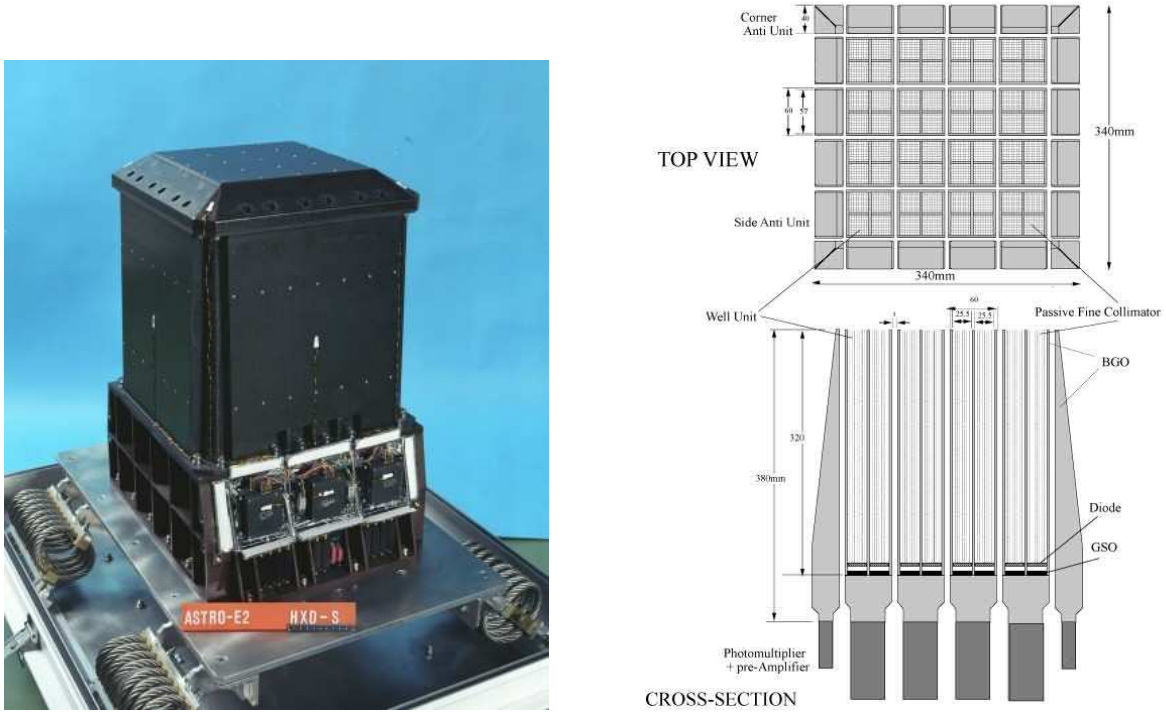

Figure 3.18: (left) The Hard X-ray Detector before installation. (right) Schematic picture of the HXD instrument.

thick phosphor bronze sheet, are inserted in the well-type BGO collimator above the PIN diodes.

Tight active shielding of HXD results in a large arrays of guard counters surrounding the main detector parts. These anti coincidence counters, made of ∼4 cm thick BGO crystals, have a large effective area for sub-MeV to MeV gamma-rays. With limited angular (∼5°) and energy (∼30% at 662 keV) resolutions, they works as a Wide-band All-sky Monitor (WAM). The WAM parameters are also shown in table 3.5.

The field of view of the HXD changes with incoming energy. Below ∼100 keV, the passive fine collimators define a $34' \times 34'$ FWHM square opening as shown in figure 3.20. The narrow field of view compared to *Beppo-SAX* PDS and *RXTE* HEXTE experiments is one of the key advantages of HXD observations. Above ∼100 keV, the fine collimators become transparent and the BGO active collimator defines a $4.5° \times 4.5°$FWHM square opening. In summary, all the PIN energy range and the lower quarter of the GSO range has a field of view of $34'$, while the GSO events above ∼100 keV have wider field of view,

Table 3.5: An overview of *Suzaku* HXD capabilities.

	PIN	GSO	WAM
Field of View	$34' \times 34'$	$34' \times 34'$ ($\leq$ 100 keV)	2π (no pointing)
		$4.5^\circ \times 4.5^\circ$ ($\geq$ 100 keV)	
Bandpass	10–70 keV	40–600 keV	50 keV – 5 MeV
Energy Resolution	$\sim$4 keV (FWHM)	$7.6/\sqrt{E}\%$ (FWHM)	
Effective Area	$\sim$160 cm^2 at 20 keV	$\sim$260 cm^2 at 100 keV	800 cm^2 at 100 keV
			400 cm^2 at 1 MeV
Time Resolution	61 μs	61 μs	31.25 ms for GRB
			1 s for All-Sky-Monitor

up to 4.5°.

Although the HXD is a non-imaging instrument, its instantaneous background can be reproduced through modeling, without requiring separate off-source observations. The HXD has been designed to achieve an extremely low in-orbit background ($\sim 10^{-4}$ counts s^{-1} cm^{-2} keV^{-1}). Figure 3.21 illustrates the comparison between detector backgrounds of hard X-ray missions. The lowest background level per effective area is achieved by the HXD at an energy range of 12–70 and 150–500 keV. The in-orbit sensitivity of the experiment can be roughly estimated by comparing the background level with celestial source intensities indicated by dotted lines. Below 30 keV, the level is smaller than 10 mCrab intensity.

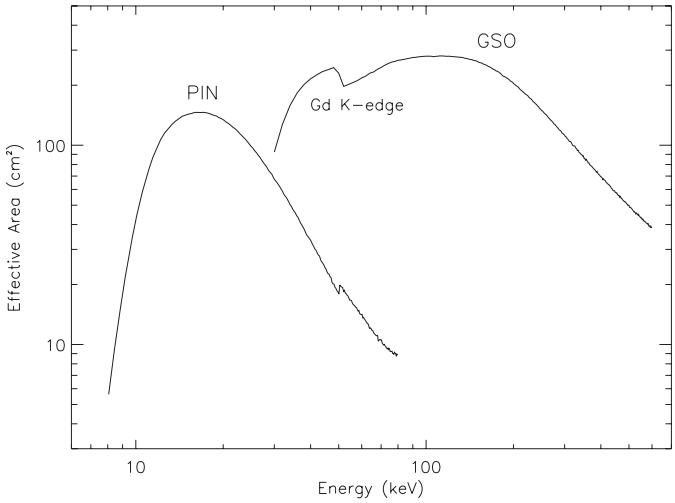

Figure 3.19: Total effective area of the HXD detectors, PIN and GSO, as a function of energy.

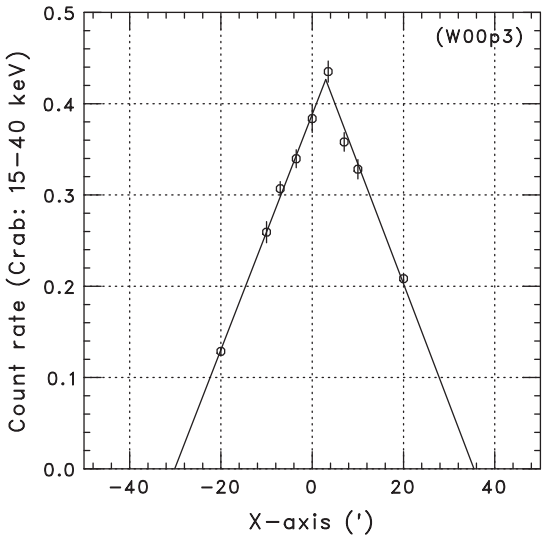

Figure 3.20: An angular response of single fine-collimator along the satellite X-axis, obtained from offset observations on the Crab nebula.

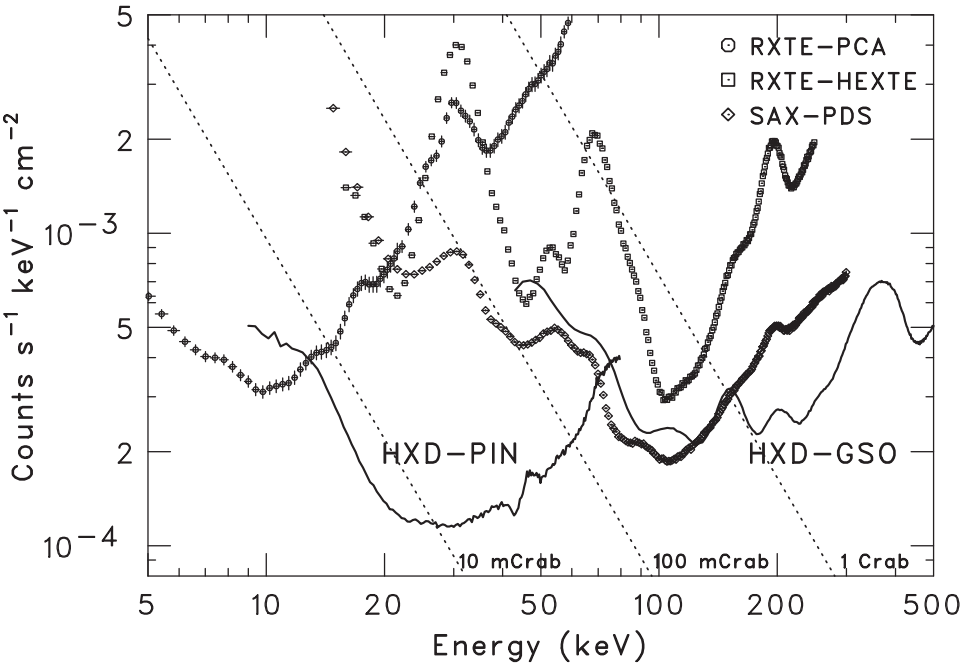

Figure 3.21: A comparison of the in-orbit detector background of the HXD PIN/GSO, with those of *RXTE* PCA, *RXTE* HEXTE, and *BeppoSAX* PDS. Dotted lines indicate 1 Crab, 100 mCrab, and 10 mCrab intensities.

Chapter 4

OBSERVATION

4.1 Targets

4.1.1 Target selection

As mentioned in §2.3, a large number of nearby galaxies were so far observed with the past X-ray observatories, and a number of ULXs were found in them. Although their X-ray data are now pulbicly available in abundance, we need to deliberately select appropriate strategies to utilize such X-ray archives. Among such a large number of ULXs, we first selected objects whose X-ray luminosity reaches $\geq 5 \times 10^{39}$ erg s^{-1} assuming isotropically radiation: this value corresponds to the Eddington limit for a ~ 30 $M_{\odot}$BHB, and largely exceeds the actually recorded luminosities of ordinary-mass (≤ 20 $M_{\odot}$) BHBs residing in our Galaxy and the Magellanic Clouds. Second, we limited our study to those objects which are located within 5 Mpc from us, in order to analyze their spectra under abundant photon fluxes. Third, to study luminosity-dependent spectral changes, we selected objects which were observed more than three times with *XMM–Newton* or *Suzaku* . After these selections, we have obtain a sample of the following 8 objects; M81 X-6, Holmberg IX X-1, Holmberg II X-1, M82 X-1, NGC1313 Source A and Source B, IC342 Source 1, and NGC5204 X-1. Basic parameters of these selected targets are tabulated in table 4.1, and their properties are described in the next subsection. We utilize those X-ray data of our sample galaxies which became publicly available by 2007 August; the logs of their observations are given in table 4.2 (*XMM–Newton*) and table 4.3 (*Suzaku*).

Because these *XMM–Newton* and *Suzaku* observations were conducted originally to

Table 4.1: Basic parameters of the target ULXs.

Host galaxy	Distance (Mpc)	$N_{\rm H}$ [a]	Source name	R.A.	Dec.
M81	3.6	4.1	X-6	09:55:33.0	+69:00:33.4
Holmberg IX	3.6	4.1	X-1	09:57:53.3	+69:03:48.0
Holmberg II	3.6	4.1	X-1	08:19:29.0	+70:42:19.3
M82	3.6	4.1	X-1	9:55:50.05	+69:40:46.3
NGC1313	3.7	4.0	Source A	03:18:20.0	-66:29:11.1
			Source B	03:18:22.2	-66:36:02.9
IC342	3.9	30.3	Source 1	03:45:55.7	+68:04:54.7
			Source 2	03:46:15.1	+68:11:13.0
NGC5204	4.8	1.4	X-1	13:29:38.6	+58:25:05.5

[a] Galactic hydrogen column density, in units of 10^{20} cm^{-2} (from NASA Goddard space flight center).

detect relatively bright X-ray targets (either the ULXs themselves or other objects in the same host galaxies), our ULX sample cannot be either complete or unbiased. However, our study is not largely dependent on the completeness of sample selection.

Table 4.2: Log of *XMM–Newton* observations of our ULX sample.

Galaxy	ObsID	R.A.	Dec.	Observation Start yy-mm-dd hh:mm:ss	Exposure (ks)
M81	0111800101	09 55 33.00	+69 03 55.0	2001-04-22 09:59:16	132.7
	0112521001	09 57 40.90	+69 03 55.0	2002-04-10 16:58:14	10.7
	0112521101	09 57 40.61	+69 03 48.9	2002-04-16 16:53:38	11.5
	0200980101	09 58 04.66	+69 03 19.5	2004-09-26 06:55:52	119.2
Holmberg II	0112520601	08 19 15.53	+70 42 08.7	2002-04-10 12:31:19	12.6
	0112520701	08 19 15.89	+70 42 06.2	2002-04-16 12:06:26	13.9
	0112520901	08 19 42.20	+70 42 06.0	2002-09-18 02:10:13	6.9
	0200470101	08 19 15.71	+70 42 02.2	2004-04-15 20:08:43	104.7
NGC1313	0106860101	03 18 14.00	-66 30 00.0	2000-10-17 00:53:58	41.3
	0150280101	03 18 24.59	-66 36 58.9	2003-11-25 00:50:59	35.6
	0150280201	03 18 22.28	-66 37 02.0	2003-12-09 05:49:18	20.7
	0150280301	03 18 20.30	-66 37 03.2	2003-12-21 01:54:45	12.2
	0150280401	03 18 19.69	-66 37 02.0	2003-12-23 04:50:43	20.8
	0150280501	03 18 19.26	-66 37 01.3	2003-12-25 04:24:32	21.4
	0150280701	03 18 18.86	-66 36 59.5	2003-12-27 03:46:05	21.5
	0150280601	03 18 16.60	-66 36 56.1	2004-01-08 03:30:34	21.8
	0150281101	03 18 14.90	-66 36 51.6	2004-01-16 23:38:52	8.9
	0205230201	03 18 16.81	-66 34 54.4	2004-05-01 21:28:43	13.8
	0205230301	03 18 19.98	-66 34 48.8	2004-06-05 06:08:51	17.2
	0205230401	03 18 31.90	-66 35 33.1	2004-08-23 05:44:43	18.0
	0205230501	03 18 25.09	-66 36 59.5	2004-11-23 06:59:33	16.0
	0205230601	03 18 12.06	-66 36 31.1	2005-02-07 11:35:10	14.3
	0301860101	03 17 27.38	-66 33 08.0	2006-03-06 16:43:12	21.8
IC342	0093640901	03 46 49.40	+68 05 38.9	2001-02-11 00:02:27	11.2
	0206890101	03 45 56.41	+68 07 23.7	2004-02-20 06:30:24	23.9
	0206890201	03 46 15.92	+68 08 43.6	2004-08-17 18:48:16	23.9

Table 4.2: Continued.

Galaxy	ObsID	R.A.	Dec.	Observation Start	Exposure
				yy-mm-dd hh:mm:ss	(ks)
	0206890401	03 45 55.66	+68 07 31.8	2005-02-10 17:26:36	23.9
NGC5204	0142770101	13 29 47.08	+58 25 19.9	2003-01-06 01:07:32	31.8
	0142770301	13 29 35.52	+58 26 08.5	2003-04-25 13:38:46	18.4
	0150650301	13 29 32.96	+58 26 09.6	2003-05-01 04:25:37	10.9

Table 4.3: Log of *Suzaku* observations of our ULX sample.

Galaxy	ObsID	R.A.	Dec.	Observation Start	Exposure (ks)[a]	
				yy-mm-dd hh:mm:ss	XIS	HXD-PIN
M81	701022010	09 55 21.02	+68 59 10.3	2006-05-07 14:53:36	91.7	
NGC1313	100032010	03 18 05.88	-66 32 06.7	2005-10-15 13:21:13	25.6	
M82	100033010	09 55 33.43	+69 45 55.8	2005-10-04 12:10:29	32.6	25.8
	100033020	09 55 34.56	+69 45 51.5	2005-10-19 00:57:47	40.5	35.1
	100033030	09 55 33.24	+69 45 54.7	2005-10-27 11:14:05	30.0	25.4

[a] Effective exposure after data screenings (§§4.2.2) are applied.

4.1.2 Comments on the sample ULXs and their host galaxies

Here, we describe basic properties of our sample galaxies and ULXs which they host. We present in figure 4.1 optical images of the sample galaxies and locations of the sample ULXs.

M81 (NGC3031) X-6

M81 is a famous inclined Sb-type spiral galaxy with a prominent bulge and well-defined spiral arms. Its distance, 3.6 Mpc, has been determined by the Cepheid measurements (Freedman et al. 1994). It hosts a typical low-luminosity AGN of $L_{\rm X} \sim 10^{40}$ erg s^{-1} (Ishisaki et al. 1996). The most luminous off-center source is called X-6 (Fabbiano et al. 1989), with a luminosity of $L_{\rm X} \sim 3$–5×10^{39} erg s^{-1} (Makishima et al. 2000; Mizuno 2000; Sugiho 2003). Due to the explosion of the supernova SN 1993J (Uno et al. 2002), located at $\sim 1'$ west from X-6, this source was frequently observed with *ASCA* . As a result, X-6 has been recognized as a typical MCD-type ULX, whose inner-disk temperature ($T_{\rm in} \sim 1.3$–1.6 keV) roughly follows a relation of $L \propto T_{\rm in}^2$ (Mizuno et al. 2001). This ULX was observed once by *Suzaku* and forth by *XMM–Newton* , and the first *XMM–Newton* observation was already analyzed by Sugiho (2003). In §§5.1, we analyze the X-6 spectra taken with *XMM–Newton* and *Suzaku* .

Holmberg IX X-1 (= M81 X-9)

Holmberg IX is a dwarf irregular galaxy which belongs to the M81 group. It hosts a bright ULX, called Holmberg IX X-1, or alternatively M81 X-9 (Fabbiano et al. 1989), although it does not in reality belong to M81. With a luminosity varying between 5–20 $\times 10^{39}$ erg s^{-1} , this ULX was long known as an enigmatic X-ray source, and was once thought to be a distant active galactic nucleus (Ezoe et al. 2001). However, it has later been recognized as a ULX in Holmberg IX (La Parola et al. 2001; Wang et al. 2003; Dewangan et al. 2006; Tsunoda et al. 2006; Sugiho 2003). It stayed in the typical PL-type state through a large part of the *ASCA* mission life time, but in 1999 it made a transition to the MCD-type state (§§2.5.2; Ezoe et al. 2001; La Parola et al. 2001; Wang et al. 2003). Analyzing the *XMM–Newton* data, Sugiho (2003) and Tsunoda et al. (2006) found that its spectrum is successfully reproduced by a variable-p model with $p \sim 0.6$. Furthermore, a soft excess component of ~ 0.3 keV (Miller et al. 2004) and an exponential cutoff at ~ 6 keV (Dewangan et al. 2006) were observed, as described in

§§2.5.4. Following M82 X-1 (§§2.6.2), this ULX is the second example showing a QPO at ∼200 mHz (Dewangan et al. 2006). In §§5.3, we spectrally study this ULX using four *XMM–Newton* observations (table 4.2).

Holmberg II X-1

This dwarf irregular galaxy is also associated with the M81 group, and hosts a ULX called X-1 with its luminosity reaching $L_{\rm X} \sim 10^{40}$ erg s^{-1} (Miyaji et al. 2001; Miller et al. 2004; Dewangan et al. 2004; Lehmann et al. 2004; Goad et al. 2005). The ULX is located in an HII complex which shows strong He II λ4686. As described in §§2.7.2, the large luminosity ($\sim 10^{40}$ erg s^{-1}) required to excite the HeII emission argues against beaming of the X-ray emission (Pakull & Mirioni 2002). We study this bright ULX in §§5.5.1 using the four *XMM–Newton* observations.

IC342 Source 1

IC342 is a face-on Scd-type galaxy at a distance of 3.9 Mpc (Tully 1988). Two ULXs, called Source 1 and Source 2 (Fabbiano & Trinchieri 1987), are located at its spiral arms. The two sources are both variable over a range of $L_{\rm X} \sim$ 5–20 $\times 10^{39}$ erg s^{-1}. *ASCA* observations of these two objects yielded the first clear evidence for spectral transitions of ULXs (§§2.5.2; Kubota et al. 2001). We study X-ray spectra of Source 1 obtained by the four *XMM–Newton* observations. We do not however investigate Source 2 since its spectrum suffers too heavy low-energy absorption ($N_{\rm H} \sim 2 \times 10^{22}$ cm^{-2}) to be compared with those of other ULXs over a sufficiently wide energy range.

NGC1313 Source A and Source B

This Scd-type galaxy, at a distance of 3.7 Mpc (Tully 1988), harbours two ULXs, Source A ($L_{\rm X} \sim$ 5–20 $\times 10^{39}$ erg s^{-1}) and Source B ($L_{\rm X} \sim$ 2–7 $\times 10^{39}$ erg s^{-1}), together with SN 1978K. These two ULXs have been extensively studied with *ASCA* (Petre et al. 1994; Makishima et al. 2000; Mizuno et al. 2001), *XMM–Newton* , and *Suzaku* .

Between two *ASCA* observations, Source A varied both in the intensity and spectrum. In the first observation made in 1993, it exhibited a PL-type spectrum with $\Gamma \sim$ 1.8, together with a 0.5–10 keV luminosity of $L_{\rm X} \sim 7 \times 10^{39}$ erg s^{-1}. In the second *ASCA* observation made in 1995, its spectrum steepened to $\Gamma \sim 2.8$, and its luminosity decreased to $L_{\rm X} \sim 5 \times 10^{39}$ erg s^{-1} (Petre et al. 1994; Mizuno 2000). Contrary to Source A, Source B exhibited on both occasions convex spectra which can be successfully

represented by the MCD model, and its luminosity ($L_{\rm X} \sim 6 \times 10^{39}$ erg s^{-1} in 1993 and $\sim 2 \times 10^{39}$ erg s^{-1} in 1995) changed apparently obeying the relation of $T_{\rm in}^2$ ($\sim$1.5 keV in 1993 and $\sim$1.1 keV in 1995).

This galaxy was observed once with *Suzaku* , and 15 times with *XMM–Newton* . The first *XMM–Newton* data were already analyzed and the properties of the two ULXs were reported (Sugiho 2003; Miller et al. 2003; Zampieri et al. 2004; Dewangan et al. 2006; Turolla et al. 2006). Furthermore, we already analyzed the *Suzaku* data of NGC1313 Source A and Source B, and published the obtained results as Mizuno et al. (2007). Including re-analysis of the *Suzaku* data, we analyze the Source A (§§5.4) and B (§§5.2) spectra, and investigate their spectral changes through these multiple observations with *Suzaku* and *XMM–Newton* .

In analyzing the *XMM–Newton* data, we excluded those periods which are affected by the background flares (§§4.2.1), and also excluded the data where on-source regions fall onto CCD gaps. As a result, we did not utilized 8 observations (2003-11-25, 2003-12-09, 2003-12-21, 2003-12-23, 2003-12-25, 2003-12-27, 2004-05-01, and 2006-03-06) for Source A, and 4 observations (2003-11-25, 2003-12-09, 2003-12-27, and 2004-05-01) for Source B. The spectra were hence extracted from the remaining 7 (Source A) and 11 (Source B) observations.

NGC5204 X-1

NGC5204 is a Magellanic irregular galaxy at a distance of 4.8 Mpc (Tully 1988). One ULX called X-1 is located $\sim 15''$ from the center of this galaxy, and exhibits a typical X-ray luminosity of $L_{\rm X} \sim$ 2–6 $\times 10^{39}$ erg s^{-1} (Roberts et al. 2004; Roberts et al. 2005). Using three *XMM–Newton* observations, we re-analyze its spectrum in §§5.5.2.

M82 (NGC3034) X-1

M82 is a prototypical star-burst irregular galaxy, located $\sim 37'$ north of M81. It has been observed repeatedly with the past X-ray observatories, due to its nearby location ($\sim$ 3.6 Mpc; Freedman et al. 1994) and its active star formation. As noted in §§2.3, this galaxy hosts the brightest source, so-called X-1, which shows the peak luminosity reaching 10^{41} erg s^{-1} (Matsumoto et al. 2001). Thus, combined with the discovery of $\sim$ 50 mHz QPOs (§§2.6.2), M82 X-1 is considered to be the most promising candidate for an intermediate-mass BH.

Spectral studies of M82 X-1 have so far been conducted extensively. With *ASCA* and *XMM–Newton* , spectral studies of X-1 were limited to energies above $\sim$ 2 keV, because of the surrounding bright diffuse thermal X-rays from this galaxy (e.g. Tsuru et al. 1997; Moran et al. 1997; Griffiths et al. 2000; Stevens et al. 2003; Ranalli et al. 2006; Strickland & Heckman 2007), and a number of compact X-ray sources at its center region. As a result, the observed spectra were reproduced by a variety of spectral models, including a simple PL of $\Gamma = 1.7$–2.5 (Matsumoto et al. 1999; Dewangan et al. 2006), a thermal plasma emission model with a temperature 4–11 keV (Matsumoto et al. 1999), an unsaturated Comptonization model (Fiorito & Titarchuk 2004; Agrawal & Misra 2006), and a slim-disk emission (Okajima et al. 2006). Using *Chandra* , Kaaret et al. (2006), successfully obtained an almost contamination-free spectrum of X-1, and reported that the X-1 spectrum in the 0.3–8 keV band is rather featureless, and can be represented by a PL model of $\Gamma \sim 1.7$.

Prior to these imaging observations in energies below $\sim$ 10 keV, the Large Area Counter onboard *Ginga* , which is a non-imaging detector sensitive over the 2–30 keV energy band, had detected signals up to $\sim$20 keV from the M82 galaxy. The obtained spectrum was better described by a thermal bremsstrahlung model of temperature $\sim$ 5.7 keV, rather than by a single PL model (Tsuru 1992). At that time, the signal was thought to originate from hot plasmas associated with M82, but it is more appropriate today to consider that the *Ginga* signals were dominated by harder photons from X-1 itself. Subsequently, spatially-integrated signals above $\sim$ 10 keV were also detected with *BeppoSAX* and *RXTE* (Cappi et al. 1999; Rephaeli & Gruber 2002).

These existing results in energies above $\sim$ 10 keV commonly indicate mildly curving broad-band spectra, rather than a power-law like one. Therefore, the PL-shaped 0.7–7 keV spectrum detected with *Chandra* is inferred to be gradually bending toward higher energies. However, the FOVs of these non-imaging instruments also contained the spiral galaxy M81, hosting a low-luminosity AGN (Ishisaki et al. 1996; Pellegrini et al. 2000; La Parola et al. 2004), located $37'$ away from M82. Therefore, possible contamination to the observed signal was not excluded. In Chapter 6, we analyze the *Chandra* and *Suzaku* data of M82, reporting on a successful detection of M82 X-1 up to $\sim$ 20 keV with little contamination from M81.

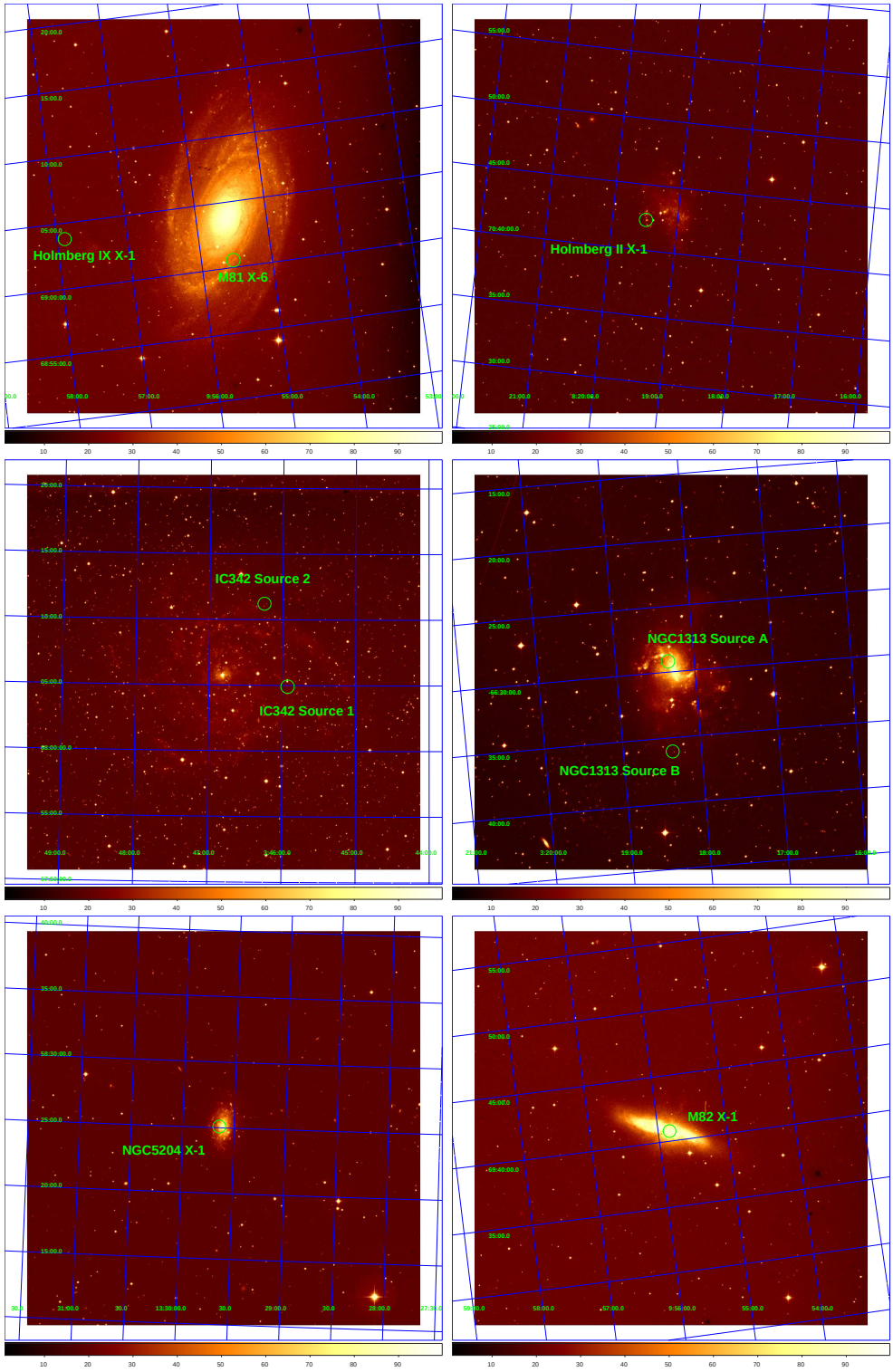

Figure 4.1: Optical images from DSS (Digitized Sky Survey) of the sample galaxies. The locations of the sample ULXs are shown in each panel.

4.2 Data Reduction

In Chapter 5 and 6, we analyze the *Suzaku* and *XMM–Newton* spectra of the sample ULXs selected in §§4.1.1. Since the procedure of extracting an X-ray spectrum of an aimed object is common to all the targets to be studied, we devote this section to its description.

4.2.1 *XMM–Newton* EPIC data screenig

Reformatted telemetry data of the *XMM–Newton* EPIC (§3.1) are available in so-called Observation Data Files (ODFs). The ODFs of individual observations were processed to produce calibrated event lists, using the *XMM–Newton* Science Analysis System (SAS) version 7.1.0 package, and the calibration file released on 2007 August 23. Specifically, the event lists of EPIC cameras (§§3.1.3) were generated using the SAS tasks called "emchain" and "epchain". The events were then corrected for the CTI and attitude of the sattelite, and cleaned by removing out-of-FOV, hot pixel and bad grade events. We used X-ray events corresponding to pattern 0–12 (single, double, triple, and quadruple pixel events) for the MOS cameras, and pattern 0–4 (single and double) for the PN camera.

In order to remove sporadic background flares described in §§3.1.3, we generated for each camera a light curve of > 10 keV events accumulated over the whole FOV. The reason for using the > 10 keV band is because this band is no longer sensitive to signal X-ray (due to the mirror reflectivity; §§3.1.2) but highly sensitive to background particles. Figure 4.2 exemplify the > 10 keV light curves of the PN and MOS CCDs from an observation of M82. Several epochs of "background flares" are clearly visible in all three cameras. We accordingly excluded those time periods when the > 10 keV count rate is typically twice or more higher than the quiescent background count rate.

As shown in figure 4.3, to analyze the spectra of individual sources, we accumulate on-source events separately for the three EPIC instruments, PN, MOS1, and MOS2, over circular regions of $30''$ radius, which corresponds to the 90% energy encircled radius of the on-axis PSF of the *XMM–Newton* X-ray telescopes (§§3.1.2). These regions are large enough to collect most of the signal photons, except in a few case: we adopt $1'$ radius for an extremely off-axis source, M81 X-9, while we employ a smaller radius of $18''$ for M82 X-1 to avoid the surrounding X-ray sources. The background spectrum of each camera is

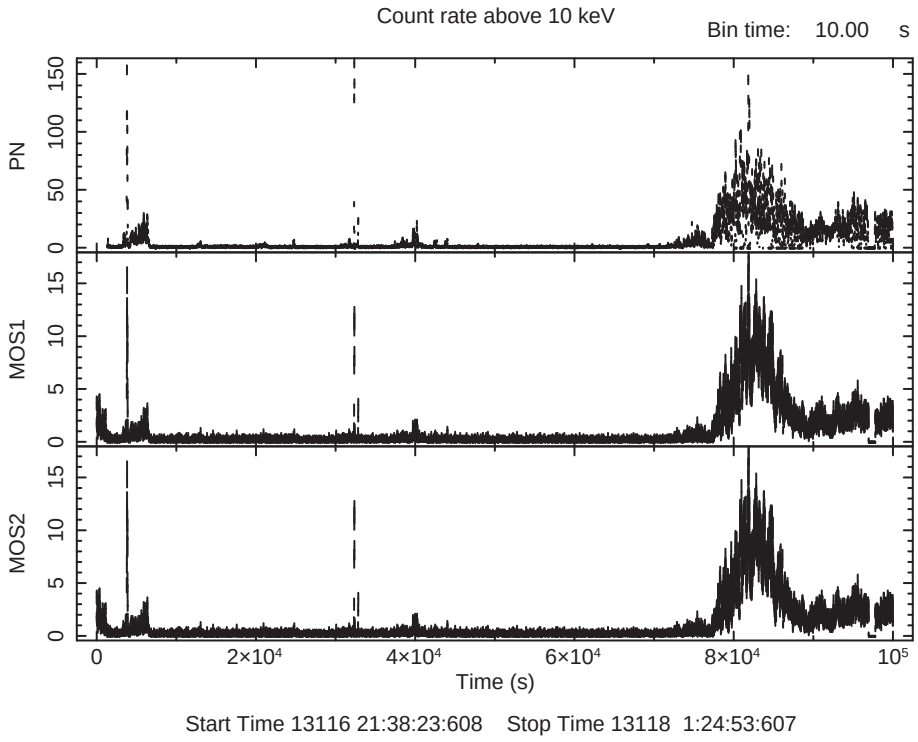

Figure 4.2: The EPIC PN (upper panel), MOS1 (middle panel), and MOS2 (lower panel) light curves (counts s^{-1}) in the > 10 keV band, acquired in the 2004 April 21 observation of M82. Events are integrated over the entire FOV of the respective cameras.

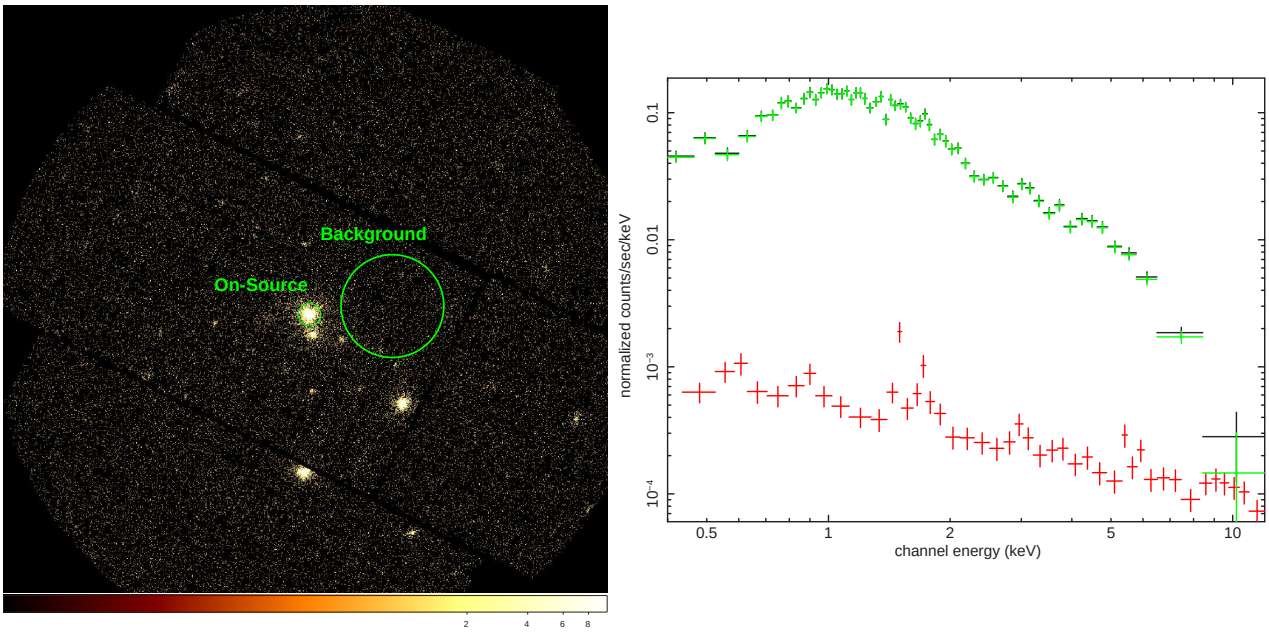

Figure 4.3: *XMM–Newton* MOS1 image in 0.5–10 keV band (left) and spectra (right), obtained from the NGC1313 2000-10-17 observation. In the left panel, the on-source and background regions used for spectral analysis of Source A are shown in green circles. In the right panel, background-inclusive, background, and background-subtracted spectra are shown in black, red, and green, respectively.

obtained from a source-free region with a larger radius of 135″, and is scaled to the same area of the on-source region.

4.2.2 *Suzaku* XIS data screening

We utilize *Suzaku* XIS data of four ULXs in three galaxies; NGC1313 Source A, NGC1313 Source B, M81 X-6, and M82 X-1. The original XIS data (§§3.2.3) acquired on-board includes several types of false events that should be rejected in the course of data analysis in order to achieve a good signal-to-noise ratio. Therefore, XIS datasets were screened by the revision 1.2 pipeline processing and HEADAS version 6.3.1 using the standard criteria as follows:

1. The telemetry saturated data are removed.

2. Hot and flickering pixels are removed by “cleansis” task, which identify such pixels based on a Poissonian analysis.

3. Events are examined for their "Grade", which are determined from the distribution of pulse heights among the 5x5 (or 3x3 or 2x2) pixels (§§3.2.3). We utilize the standard selection of Grade 0,2,3,4, and 6.

4. We exclude those data which were taken while the spacecraft is in the South Atlantic Anomaly (SAA), or within 500 seconds of an exit out of the SAA, because the high particle flux makes these data unusable.

5. We further discard data taken in regions where geomagnetic cutoff rigidity (COR) of cosmic rays is lower than 6 GeV. This is to avoid high particle background.

6. Data are discarded if the target elevation angle above the night Earth is lower than 5°, or that above the sunlit Earth is less than 20°. The latter is to avoid atmospheric scattering of solar X-rays.

The above procedure gives a set of "screened events". Since each event is tagged with energy, timing, and two-dimentional position, we can sort the events to produce light curves, images, and spectra using the software package xselect version 2.4. For two ULXs in NGC 1313 and M82 X-1, the on-source spectra are extrected over circular regions of $3'$ radius, and the background spectra are obtained over source-free regions. Only in the case of M81 X-6, we extract its spectrum over a circular region of $1'$ radius, in order to minimize contributions from the M81 nucleus, located $\sim 4'$ north of this ULX. For the same reason, the background spectrum of M81 X-6 is obtained from another $1'$ radius region, at the same distance from the nucleus as the on-source region. Since the three FI sensors (XIS0, 2, and 3) have nearly the same properties, we co-added their data into a single spectrum. The events from the BI sensor (XIS1) from another spectrum. In studying each ULX, we thus jointly analyze an FI spectrum and a BI spectrum.

4.2.3 Model fitting to X-ray spectra

After obtaining the background-subtracted spectra of our sample ULXs, in the present thesis, we quantitatively analyze them via so-called spectral model fitting in the following steps. We first take a model spectrum (e.g., a power-law) with a small number of free parameters (e.g., photon index and normalization). We then convolve the model with the known detector response, to produce a simulated spectrum which is binned into

the same manner as the actual spectrum. Finally, we adjust the model parameters, so that the difference between the data and model is minimized. Here, we utilize the standard χ^2 minimization. We calculate the response matrix (including the effective area) for each source separately in the standard manner for *XMM–Newton* EPIC and *Suzaku* XIS, because the response is dependent on the position of the detector, due to the energy-dependent vignetting of the mirror (§§3.1.2 and §§3.2.2). We never try to remove the detector responses from the observed spectra, because the results of such "deconvolution" process is known to be highly unstable, and the associated errors are very difficult to estimate. We jointly fitted the spectra of PN, MOS1, and MOS2 for the *XMM–Newton* data and FI and BI for the *Suzaku* XIS data, assuming the same spectral model in all detectors, and evaluating the chi-square summed over the three spectra.

Chapter 5

SPECTRAL STUDIES OF ULXS

In this Chapter, we describe spectral analyses of the sample ULXs selected in the previous Chapter (§4.1).

5.1 M81 X-6

5.1.1 Spectral properties of *Suzaku* and *XMM–Newton* data

We start our analysis from M81 X-6, a typical ULX showing $L_{\rm X} = (3\text{–}5) \times 10^{39}$ erg s^{-1} (§§2.5.3, §§4.1.2). Previous observations all found this object in a typical MCD-type state (§§4.1.2), so our objective is to reconfirm (or modify) this view based on newer observations. Its observation was described in §§4.1.1.

Figure 5.1 shows background-subtracted spectra of M81 X-6 obtained by the *Suzaku* and *XMM–Newton* observations. The spectra were extracted through the procedure described in §§4.2.1 and §§4.2.2. Although an *XMM–Newton* observation generally provides three CCD spectra (PN, MOS1, and MOS2), we discarded the PN and MOS1 data on 2001-04-22 and the PN data on 2004-09-26, because the source was outside the FOV of these detectors. As is customary in X-ray astrophysics, the spectra in figure 5.1 are presented without removing the instrumental response, so that the spectrum does not become flat even when the incident photons have an energy-independent flux density. The spectra show a steeper decrease toward lower energies than is explained by the instrumental photoelectric absorption, indicating the presence of a significant column density for photoelectric absorption. This is partly due to the line-of-sight hydrogen column density within

our Galaxy, $N_{\rm H} \sim 4.1 \times 10^{20}$ cm^2, but an additional contribution from the host galaxy is suggested. The spectra of M81 X-6 are featureless, except an instrumental structure at ∼2.3 keV due to the Au M-edge in the mirror coating. The steep flux decrease above ∼ 4 keV is partially intrinsic to the source, but is enhanced by the decreasing mirror reflectivity and the increasing CCD transparency.

In order to grossly evaluate these featureless spectral continua, we derived the spectrum into three energy ranges of 1–2 keV, 2–4 keV, and 4–10 keV, and calculated ratios of the signal photons therein; these are called "hardness ratios". Hereafter, the (2–4 keV) / (1–2 keV) ratio is refered to as "hardness ratio 1" (HR1), while that in (4–10 keV) / (2–4 keV) as "hardness ratio 2" (HR2). Since the hardness ratio is an instrument-dependent quantity, the four types of detectors (BI and FI of the *Suzaku* XIS, and PN and MOS of the *XMM–Newton* EPIC) give slightly different values even for the same incident spectrum. However, the difference is at most 30% for representative spectra. Figure 5.2 (left), called color-color plot (CCP), provides a scatter plot between HR1 and HR2 as a measure of spectral shape changes, and figure 5.2 (right) their dependence on the 0.5–10 keV X-ray luminosity, called luminosity-color plot (LCP) hereafter. The luminosities are in the range of $L_{\rm X} = (4\text{–}7) \times 10^{39}$ erg s^{-1}, and the hardness ratios are obtained at HR1 ∼ 0.6 and HR2 ∼ 0.5–0.6.

5.1.2 Spectral fitting

In order to complement the qualitative examination carried out in the previous subsection, we need more quantitative anaylsis. This is usually done through a process of spectral "fitting", where we start from a simple spectral model, convolve it with the detector response, compare the convolved model with the data, and optimize the model parameters via chi-square minimization. We therefore applied this procedure to the 5 sets of spectra, using several representative models for the X-ray continuum.

Firstly, we tried a power-law (PL) model, of the form

$$\propto E^{-\Gamma}, \tag{5.1}$$

where E is the energy and Γ is photon index; this gives an empirical representation of none-thermal emission from, e.g., AGNs, pulsars, and hard-state BHBs. We multiplied this spectral model with photoelectric absorption in low energies, described by a free

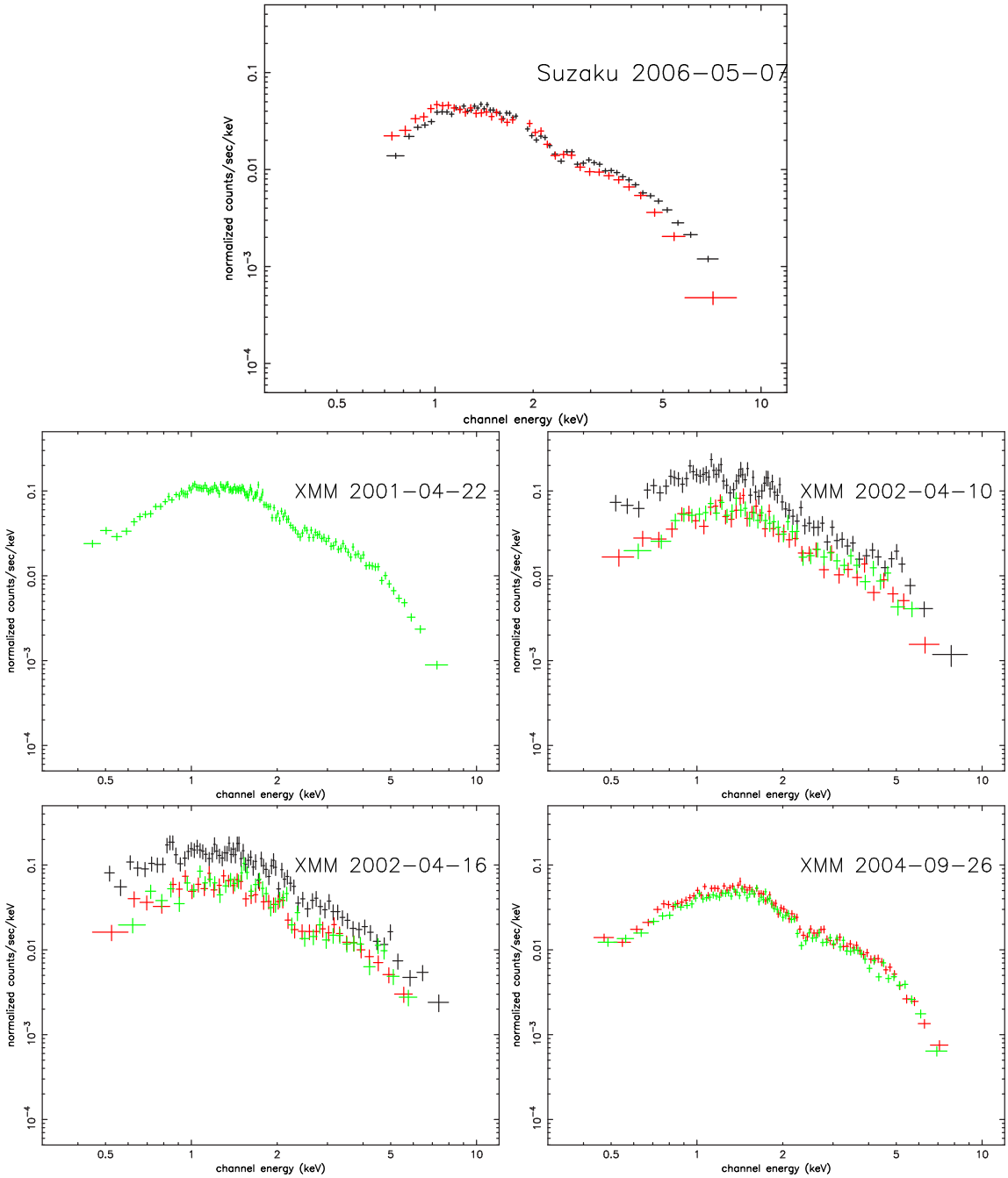

Figure 5.1: Background-subtracted spectra of M81 X-6 from the *Suzaku* observation (2006-05-07, top) and from the four *XMM–Newton* observations (dates indicated in individual panels). Each spectrum includes the instrumental response. In the *Suzaku* spectra, the FI (three cameras averaged) and BI CCD data are shown in black and red, respectively. In the *XMM–Newton* spectra, the PN, MOS1, and MOS2 data are shown in black, red, and green, respectively.

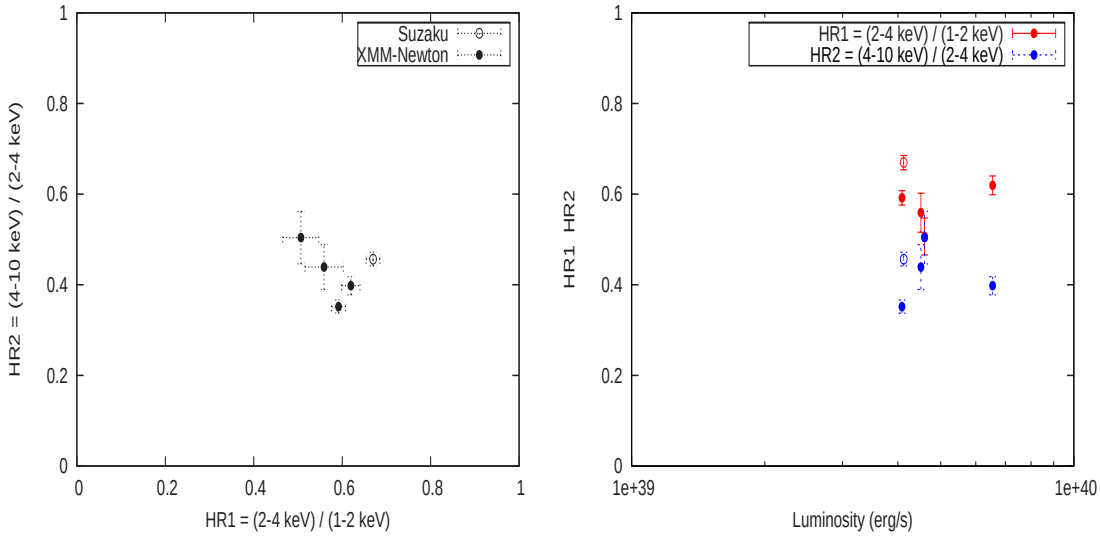

Figure 5.2: The color-color plot (CCP; left) and the luminosity-color plot (LCP; right) of M81 X-6 acquired by the *XMM–Newton* and *Suzaku* observations. One data point represents an observation.

value of $N_{\rm H}$ which represents column density of the intervening material (including the interstellar gas within our Galaxy and that associated with M81). We show in figure 5.3 (upper left) the *Suzaku* spectra fitted with the absorbed PL model, and summarize the derived parameters in table 5.1. Here, we jointly fitted the spectra of FI (three FIs are averaged) and BI, assuming the same spectral model in both detectors, and evaluating the chi-square summed over the two spectra. As the obtained reduced chi-square is relatively large ($\chi^2/\nu = 416.1/89$), the PL fit is unacceptable; the fit residuals show that the spectrum has a more convex shape compared to the straight PL model, especially in the higher energy range.

As an alternative spectral model, we employed a multi-color disk (MCD) model from standard accretion disks. As described in §§2.2.2, the MCD model has a moderately curved shape, and successfully expresses the ultrasoft emission from optically thick accretion disks typically observed in Galactic BHBs and NSBs. As shown in figure 5.3 (top), the MCD fit with an inner-disk temperature of $T_{\rm in} \sim 1.3$ keV gave a better fit with $\Delta\chi^2 = -295.2$ than the PL model. The derived luminosity and $T_{\rm in}$ are typical for this source, and are consistent in particular with those acquired with *ASCA* (Mizuno 2000; Makishima et al. 2000; Mizuno et al. 2001). We therefore reconfirm that this object is

an MCD-type ULX.

While the spectra favor the MCD model with $T_{\rm in} \sim 1.3$ keV, the fit is not yet fully successful. We have accordingly examined the variable-p disk model, shown in figure 5.3 (bottom). As described in §§2.2.4, the temperature profile in this model is assumed to scale as $T(r) \propto r^{-p}$ with a free parameter p, instead of the $T(r) \propto r^{-0.75}$ scaling of the MCD model. A smaller value of p gives a spectrum with a less convex curvature. In fact, the variable-p model has given a still better fit with $\chi^2/\nu = 114.8/88$, and indicated $p = 0.67^{+0.05}_{-0.04}$ (table 5.1), which is significantly different from that of the MCD model ($p = 0.75$). According to an F-test, the improvement from the MCD fit to the variable-p disk fit is significant at the $\sim 96\%$ confidence limit.

Although the variable-p disk provides a significantly better fit to the data than the other two models, the fit is not fully successful; the probability of this fit being acceptable is 3%. Actually, the residuals in figure 5.3 (bottom) become significantly belows 1 keV, and a line-like structure is seen at ~ 1 keV. Such a feature is reminiscent of highly ionized Fe-L line complex, observed from a wide variety of cosmic hot plasmas. Therefore, we add a thin thermal plasma model, so-called "mekal" in xspec, to the variable-p disk fit. The metal abundance of the plasma was assumed to be the solar values. As a result, the fit was improved by $\Delta\chi^2 = -13.6$ to $\chi^2/\nu = 101.2/86$ (with a probability of 13% for this fit to be acceptable), while the parameters of the variable-p disk model remained unchanged within errors. The obtained 0.5–10 keV plasma luminosity is $\sim 8 \times 10^{37}$ erg s^{-1}, with a temperature of $1.2^{+0.4}_{-0.3}$ keV. Such a thin thermal plasma component has been detected from several other ULXs, and interpreted as X-ray luminous young supernova remnants possibly associated with the ULXs (Dewangan et al. 2004, Soria et al. 2006, Strohmayer et al. 2007), or large-scale diffuse plasma distributed within M81.

We applied the same spectral fits to the four observations with *XMM–Newton* ; by the PL, MCD, and variable-p disk models. As summarized in table 5.1, the fitting results are consistent with that of *Suzaku* : the spectra prefer the MCD model to the PL model, and the variable-p disk model further improves the fits. More specifically, the spectra in the first (2001-04-22), second (2002-04-10), and third (2002-04-16) *XMM–Newton* observations are nearly consistent with that acquired by *Suzaku* , with the luminosity of $L_{\rm X} \sim 4 \times 10^{39}$ erg s^{-1}. They are successfully ($\chi^2/\nu = 1.01$–1.05) fitted by the variable-p disk model, with the inner-disk temperature $T_{\rm in} \sim 1.4$ keV and $p \sim 0.6$. In the

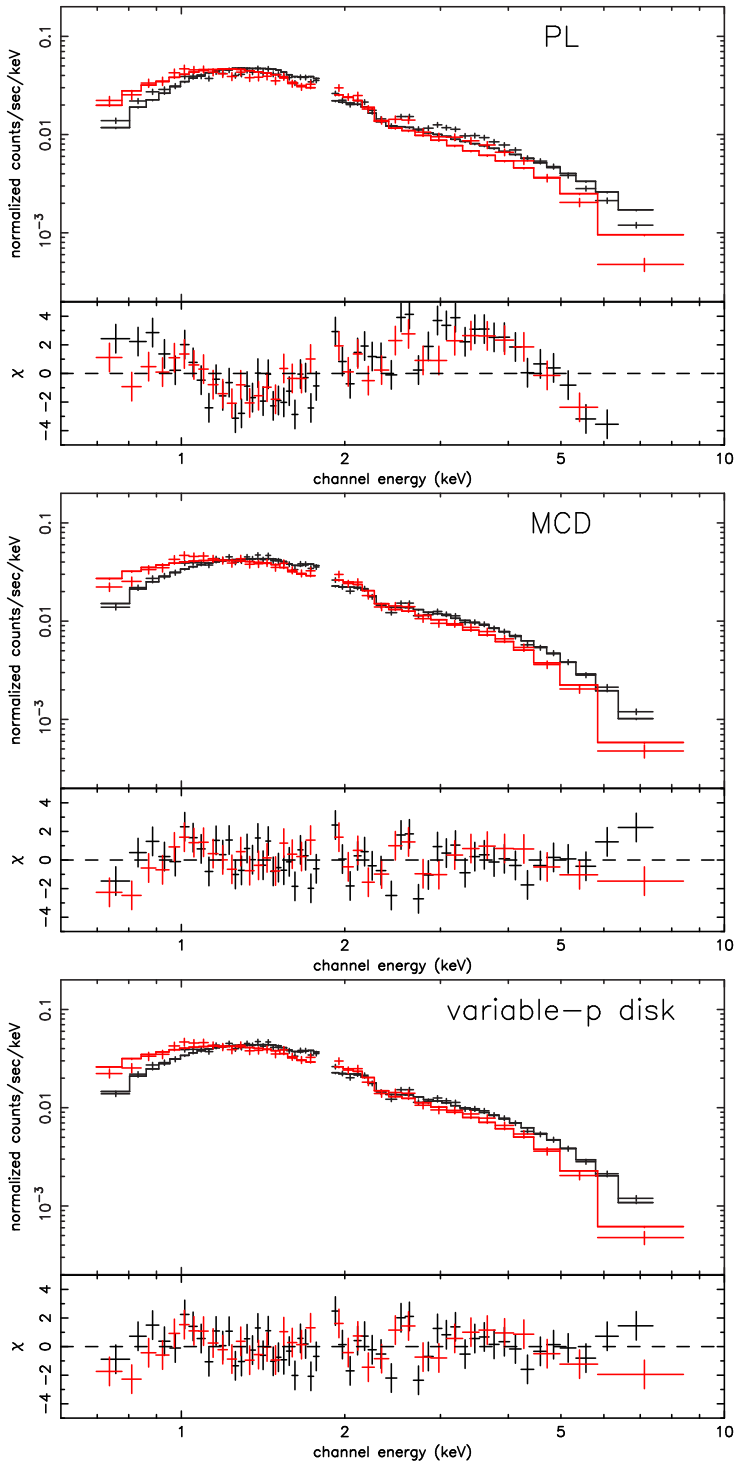

Figure 5.3: Background-subtracted and response-inclusive spectra of M81 X-6 obtained with *Suzaku* , presented together with the best-fit convolved models. The bottom half of each panel shows the fit residuals. The FI and BI data are fitted simultaneously, and are shown in black and red, respectively. The employed model is a power-law (PL; top), a multi-color disk (MCD; middle), and a variable-p disk (bottom). These models are multiplied by photoelectric absorption, and then convolved with the detector response.

Table 5.1: Summary of model fits to the *Suzaku* and *XMM–Newton* spectra of M81 X-6. [a,b]

	Model	$N_{\rm H}$ (10^{22} cm^{-2})	Parameters	$F_{\rm X}$ [c]	$L_{\rm X}$ [c]	χ^2/ν
			Suzaku			
2006-05-07	PL [d]	0.37	$\Gamma = 2.17$	2.6	4.2	416.1/89
	MCD	$0.03^{+0.01}_{-0.01}$	$T_{\rm in} = 1.34^{+0.03}_{-0.03}$	2.6	4.2	120.5/89
	variable-p	$0.08^{+0.04}_{-0.04}$	$T_{\rm in} = 1.43^{+0.08}_{-0.07}$ / $p = 0.67^{+0.05}_{-0.04}$	2.6	4.2	114.8/88
			XMM–Newton			
2001-04-22	PL [d]	0.32	$\Gamma = 2.00$	2.8	4.5	267.4/128
	MCD	$0.11^{+0.01}_{-0.01}$	$T_{\rm in} = 1.35^{+0.03}_{-0.03}$	2.5	4.0	168.5/128
	variable-p	$0.20^{+0.02}_{-0.02}$	$T_{\rm in} = 1.69^{+0.14}_{-0.11}$ / $p = 0.60^{+0.03}_{-0.02}$	2.6	4.2	128.0/127
2002-04-10	PL	$0.29^{+0.03}_{-0.03}$	$\Gamma = 1.76^{+0.08}_{-0.07}$	3.1	5.0	177.0/153
	MCD	$0.11^{+0.02}_{-0.02}$	$T_{\rm in} = 1.59^{+0.10}_{-0.09}$	2.8	4.5	171.4/153
	variable-p	$0.20^{+0.05}_{-0.04}$	$T_{\rm in} = 2.11^{+0.71}_{-0.29}$ / $p = 0.61^{+0.05}_{-0.04}$	2.9	4.6	159.2/152
2002-04-16	PL	$0.27^{+0.03}_{-0.03}$	$\Gamma = 1.73^{+0.08}_{-0.07}$	3.1	5.0	173.4/161
	MCD	$0.10^{+0.02}_{-0.02}$	$T_{\rm in} = 1.57^{+0.10}_{-0.09}$	2.7	4.3	172.3/161
	variable-p	$0.19^{+0.06}_{-0.04}$	$T_{\rm in} = 2.09^{+0.96}_{-0.31}$ / $p = 0.61^{+0.05}_{-0.05}$	2.8	4.5	162.0/160
2004-09-26	PL	$0.29^{+0.02}_{-0.02}$	$\Gamma = 1.68^{+0.04}_{-0.04}$	4.5	7.2	216.0/159
	MCD	$0.12^{+0.01}_{-0.01}$	$T_{\rm in} = 1.62^{+0.05}_{-0.05}$	3.8	6.1	218.3/159
	variable-p	$0.22^{+0.02}_{-0.02}$	$T_{\rm in} = 2.32^{+0.35}_{-0.25}$ / $p = 0.60^{+0.02}_{-0.02}$	4.1	6.6	170.7/158

[a] All quoted errors are 90% confidence regions.

[b] The temperatures of parameters are in the units of keV.

[c] The 0.5–10 keV absorption uncorrected flux in 10^{-12} erg s^{-1}cm^{-2} and luminosity in 10^{39} erg s^{-1} .

[d] Errors are not shown since the fit is far from acceptable.

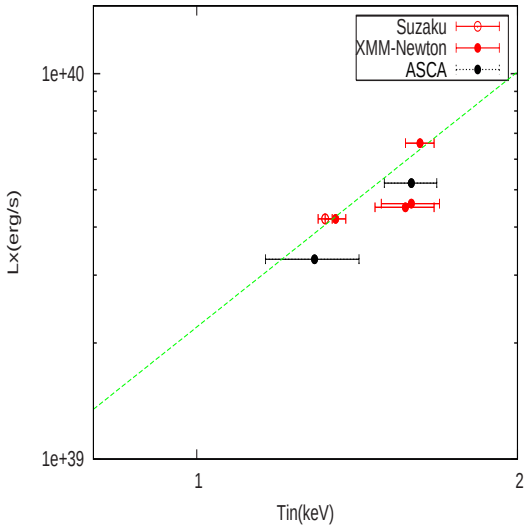

Figure 5.4: The luminosity vs. $T_{\rm in}$ relation of M81 X-6 among the *Suzaku* , *XMM–Newton* , and *ASCA* observations, when the spectra are fitted by the MCD model. The green dashed line expresses the bestfit $L_{\rm X} \propto T_{\rm in}^{2.2}$.

forth observation (2004-09-26), the source became more luminous by about 50%. Nevertheless, the spectra are again reproduced successfully ($\chi^2/\nu = 1.08$) by the variable-p disk model, with a higher $T_{\rm in}$(~ 2.3 keV).

The relation between the X-ray luminosity and $T_{\rm in}$ is presented in figure 5.4. Here, we also include the *ASCA* results referring to Mizuno (2000). By fitting the plot by a function of $L \propto T_{\rm in}^{\alpha}$ where α is a parameter, we obtained $\alpha = 2.2 \pm 0.8$ (the error being the 90% confidence region). As described in §§2.5.3, this property, namely a value of α which is significantly smaller than 4, agrees with those observed from MCD-type ULXs in general (Mizuno 2000; Mizuno et al. 2000; Sugiho 2003), and the behavior of Galactic BHBs in the slim disk state (Kubota et al. 2004; Abe et al. 2005). Thus, our results on the *Suzaku* and *XMM–Newton* observations strengthen the view (Sugiho 2003; Tsunoda et al. 2006) that this MCD-type ULX corrresponds to BHBs in the slim-disk state.

Finally, in figure 5.5 we show the spectra unfolded utilizing the best-fit variable-p disk model, so that the spectra observed with the different instruments can be directly compared. These are given in so-called "νF_ν" form, where the inferred incident photon-number spectrum is multiplied by E^2 for the purpose of presentation. Among the five spectra obtained from *Suzaku* and *XMM–Newton* , we omitted those from the second and

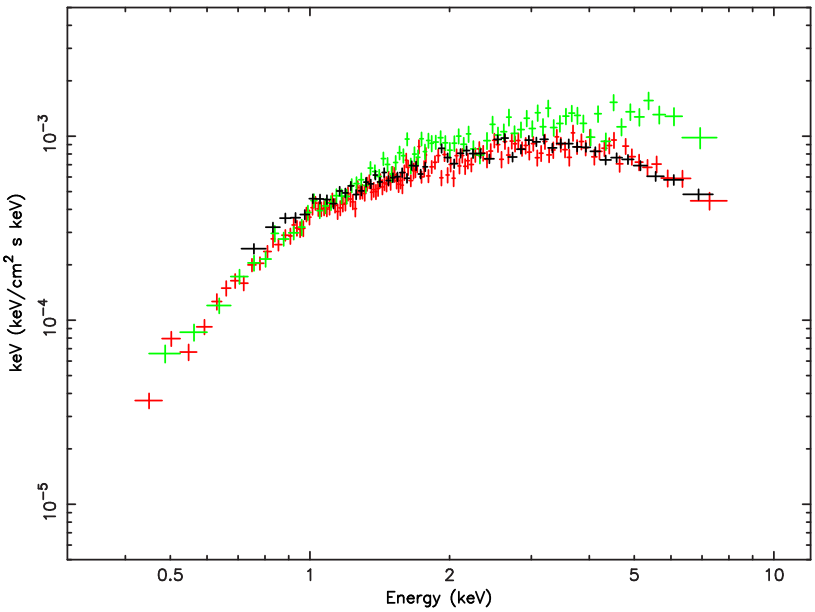

Figure 5.5: Unfolded νF_ν spectra of M81 X-6. The black spectrum is from the FI CCD data of the *Suzaku* 2006-05-07 observation, while the red and green spectra are from the MOS2 CCD data of the *XMM–Newton* 2001-04-22 and 2004-09-26 observations, respectively.

third *XMM–Newton* observations, because they are statistically poorer than the others, and are nearly identical to the first *XMM–Newton* spectrum. We can clearly see in figure 5.5 that all the spectra are significantly more convex than straight power-law forms. The *Suzaku* and the first *XMM–Newton* spectra are almost the same, while the fourth *XMM–Newton* spectrum is brighter particularly in higher energy ranges above 2 keV. This is represented quantitatively by the significant higher values of $T_{\rm in}$ in table 5.1. Around ~ 0.9 keV, the *Suzaku* spectrum shows a local excess above those from *XMM–Newton* , due probably to the thin-thermal component. Its absence in the *XMM–Newton* spectra suggests that the plasma is more extended than $\sim 5''$ (or ~ 100 pc), rather than localized to the close vicinity of X-6.

From the spectral analysis of M81 X-6 using the *Suzaku* and *XMM–Newton* observations, we have obtained the following results:

1. The spectra obtained from the *Suzaku* and *XMM–Newton* data were of MCD-type, rather than PL-type, in agreement with the *ASCA* results.

2. The luminosity changes nearly proportional to $T_{\rm in}^2$, and the variable-p disk model

with $p \sim 0.6$ gives a better (and nearly acceptable) fit than the simple MCD model. Therefore, this ULX is considered to reside in the slim-disk state.

5.2 NGC1313 Source B

As the next target, we analyze the *XMM–Newton* and *Suzaku* data of the ULX called NGC1313 Source B, because this source exhibits the MCD-type spectra (§§4.1.2), like M81 X-6 studied in the previous subsection. Although preliminary results from the *Suzaku* observation were already published as Mizuno et al. (2007), we perform a more detailed and unified analysis of the *Suzaku* data, together with those from *XMM–Newton* .

5.2.1 Spectral properties on the CCP

In order to evaluate the overall spectral features, we first extracted hardness ratios from individual *Suzaku* and *XMM–Newton* observations (§§4.1.1), and arranged them on a CCP and an LCP, similarly to M81 X-6 in the previous subsection. As seen in figure 5.6, the flux from this source varied by $\sim 30\%$ during the *Suzaku* observation; therefore, we divided the *Suzaku* -XIS data into two periods, namely brighter (the former ~ 20 ks) and fainter (the latter ~ 8 ks) phases, and analyzed their spectra separately. The derived CCP and LCP are presented in the left and right panels of figure 5.7, respectively.

As shown in the CCP (figure 5.7 left), the data points are roughly separated into two groups. One is located at HR1 ~ 0.6 and HR2 ~ 0.5–0.6, while the other at HR1 ~ 0.4 and HR2 ~ 0.3–0.5. From the LCP (figure 5.7 right), the data points of the former group are found to concentrate at a higher luminosity range of $L_{\rm X} \sim 6$–$7\ \times 10^{39}$ erg s^{-1} , and those of the latter group exhibit lower luminosities as $L_{\rm X} \sim 1.3$–$2\ 10^{39}$ erg s^{-1} . Because the location of the former group on the CCP is similar to that observed from M81 X-6 (the previous section), we speculate that the spectra in this group exhibit an MCD-like shape. On the other hand, the data in the latter group are thought to exhibit a different spectral shape. In other words, spectral transitions are suggested.

5.2.2 Spectral fitting

In order to investigate our inference mode in the previous subsection, we conducted the spectral fitting for each observation. First, we show in figure 5.8 (top left) the spectrum obtained by the *Suzaku* brighter phase, together with a best-fit PL model. While the PL model thus gives an unacceptable fit with $\chi^2/\nu = 158.0/91$, the spectrum is well described by an MCD model with $T_{\rm in} \sim 1.6$ keV and $\chi^2/\nu = 91.0/91$ (with a probability of 48%

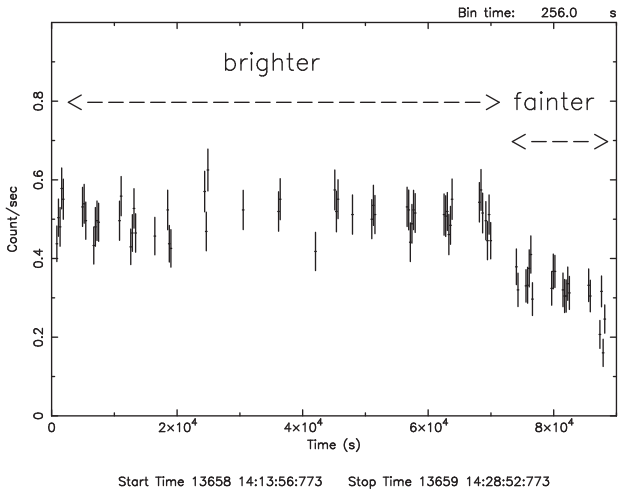

Figure 5.6: The background-subtracted 0.5–10 keV lightcurve of NGC1313 Source B obtained by the *Suzaku* XIS (three FIs co-added).

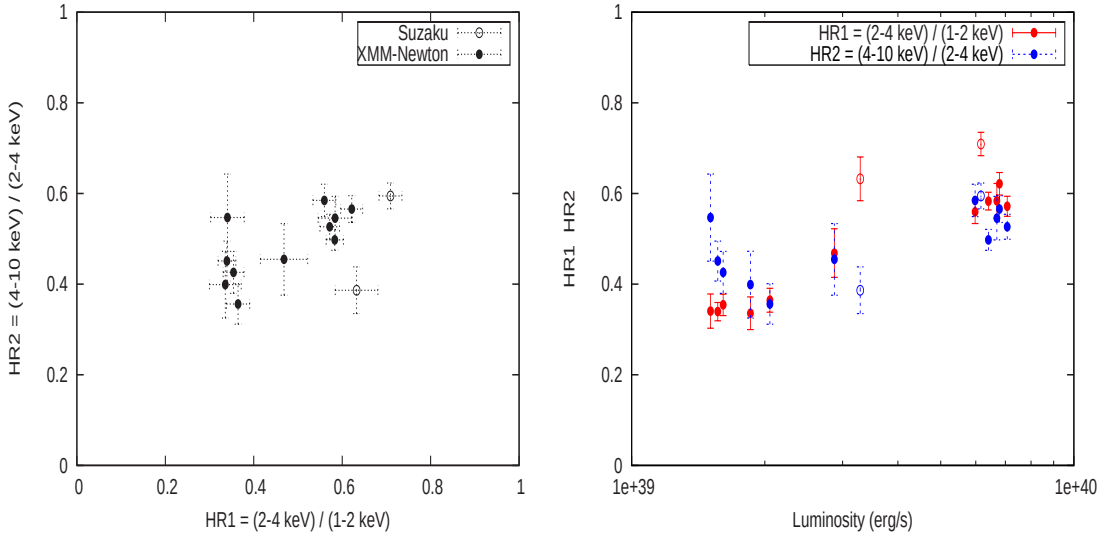

Figure 5.7: The CCP (left) and LCP (right) of NGC1313 Source B, acquired in the *XMM–Newton* and *Suzaku* observations.

for this fit to be acceptable), as shown in figure 5.8 (top right) and summarized in table 5.2. Thus, as already suggested by the CCP, the source shows an MCD-type spectra on this occasion like the spectrum observed from M81 X-6. This reconfirms Mizuno et al. (2001).

Figure 5.8 (bottom left) shows the spectrum from the first *XMM–Newton* observation, when the source exhibited a lower luminosity of $L_{\rm X} \sim 1.5 \times 10^{39}$ erg s^{-1} . As represented by the bottom two panels of figure 5.8, the spectrum was fitted successfully by a PL model of $\Gamma \sim 2.2$ with $\chi^2/\nu = 121.3/115$ (with a probability of 33% to be acceptable), but the MCD model failed with $\chi^2/\nu = 355.3/115$. Similarly, we conducted the spectral fitting to the spectra on the other occasions. Figure 5.9 shows $\Delta\chi^2$ as a function of luminosity, where $\Delta\chi^2$ is as a difference between χ^2 obtained by the PL model and that by the MCD model; positive values mean an MCD-preferred spectrum, and negative values a PL-preferred one. We can see that the spectra while the source is dim ($L_{\rm X} \sim$ 1.2–3 $\times 10^{39}$ erg s^{-1}) favor an PL model rather than a MCD model, while those in the higher luminosity ($L_{\rm X} \sim$ 3–7 $\times 10^{39}$ erg s^{-1}) are well fitted by an MCD model. We summarized the fitting parameters in table 5.2. Thus, this ULX is found to exhibit an MCD-type spectrum in its brighter phase, and an PL-type one in the fainter phase.

In table 5.2, the value of $N_{\rm H}$ scatters among observations, with a clear tendency that the MCD fit yields a systematically lower value than the PL fit. Since $N_{\rm H}$ is unlikely to vary with time, we regard this as an artifact caused by different model shapes. When the source is in the PL-type state, we consistently observe $N_{\rm H} =$ 2–3 $\times 10^{21}$ cm^{-2}, which we regard as a realistic estimate.

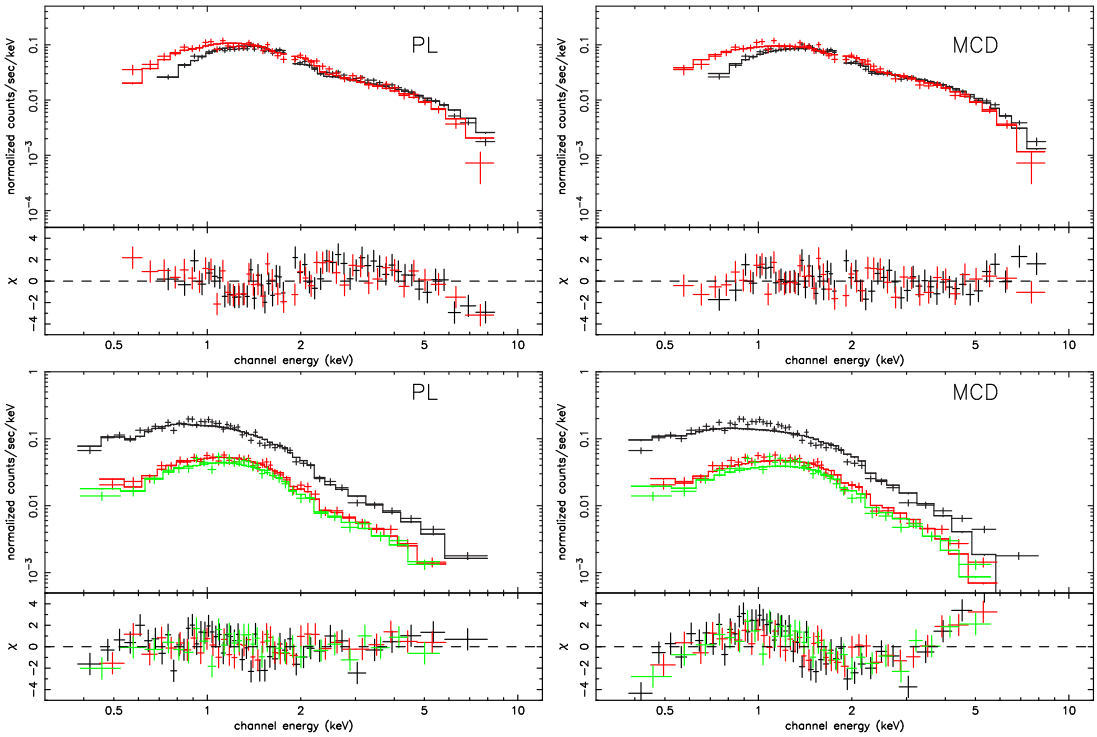

Figure 5.8: Spectra of NGC1313 Source B. The *Suzaku* XIS spectra of the brigher phase are shown with the best-fit PL (top left) and MCD (top right) models. The *XMM–Newton* EPIC spectra obtained from the first observation (2000-10-17) are shown with the best-fit PL (bottom left) and MCD (bottom right) models.

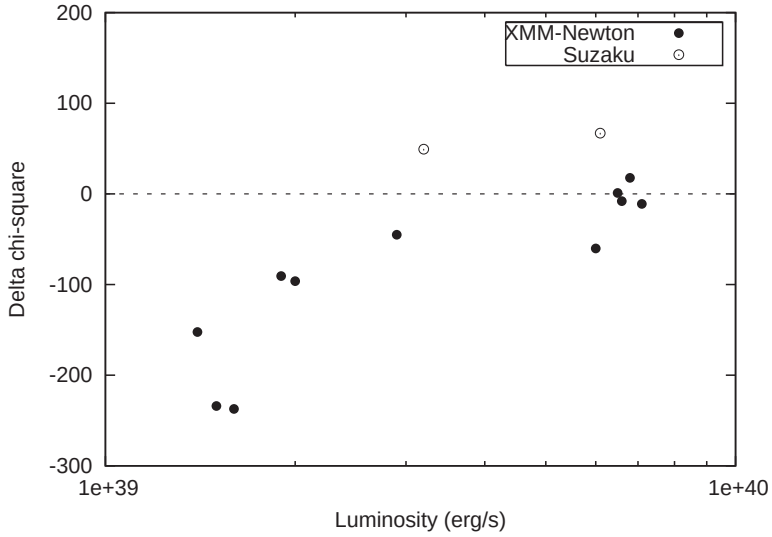

Figure 5.9: The difference in the fit goodness between the MCD and PL models, namely $\Delta\chi^2 \equiv \chi^2_{PL} - \chi^2_{MCD}$, plotted as a function of the 0.5–10 keV luminosity.

Table 5.2: Summary of model fits to the *XMM–Newton* and *Suzaku* spectra of NGC1313 Source B. [a,b]

	Model	$N_{\rm H}$ (10^{22} cm^{-2})	Parameters	$F_{\rm X}$ [c]	$L_{\rm X}$ [c]	χ^2/ν
			Suzaku 2005-10-15			
brighter	PL	$0.33^{+0.03}_{-0.03}$	$\Gamma = 1.88^{+0.05}_{-0.04}$	3.9	6.6	158.0/91
	MCD	$0.07^{+0.02}_{-0.02}$	$T_{\rm in} = 1.58^{+0.05}_{-0.05}$	3.6	6.1	91.0/91
	variable-p	$0.16^{+0.04}_{-0.04}$	$T_{\rm in} = 1.87^{+0.21}_{-0.16}$ / $p = 0.63^{+0.04}_{-0.03}$	3.6	6.1	78.0/90
fainter	PL	$0.37^{+0.06}_{-0.06}$	$\Gamma = 2.22^{+0.08}_{-0.07}$	2.1	3.6	130.3/97
	MCD	$0.08^{+0.03}_{-0.03}$	$T_{\rm in} = 1.21^{+0.07}_{-0.07}$	1.9	3.2	81.0/97
	variable-p	$0.08^{+0.08}_{-0.09}$	$T_{\rm in} = 1.21^{+0.19}_{-0.15}$ / $p = 0.75^{+0.25}_{-0.13}$	1.9	3.2	81.0/96
			XMM–Newton			
2000-10-17	PL	$0.26^{+0.02}_{-0.02}$	$\Gamma = 2.41^{+0.06}_{-0.07}$	0.89	1.5	121.3/115
	MCD [d]	0.05	$T_{\rm in} = 0.91$	0.74	1.3	355.3/115
2003-12-21	PL	$0.25^{+0.02}_{-0.02}$	$\Gamma = 1.72^{+0.04}_{-0.04}$	3.7	6.3	128.5/109
	MCD	$0.09^{+0.01}_{-0.01}$	$T_{\rm in} = 1.59^{+0.06}_{-0.05}$	3.3	5.6	188.7/109
	variable-p	$0.21^{+0.02}_{-0.01}$	$T_{\rm in} = 2.78^{+0.72}_{-0.39}$ / $p = 0.57^{+0.02}_{-0.02}$	3.5	6.0	108.9/108
2003-12-23	PL	$0.26^{+0.02}_{-0.02}$	$\Gamma = 1.71^{+0.05}_{-0.05}$	4.2	7.1	179.2/149
	MCD	$0.10^{+0.01}_{-0.01}$	$T_{\rm in} = 1.64^{+0.07}_{-0.06}$	3.7	6.3	187.2/149
	variable-p	$0.20^{+0.03}_{-0.03}$	$T_{\rm in} = 2.40^{+0.54}_{-0.32}$ / $p = 0.60^{+0.03}_{-0.03}$	3.9	6.6	154.9/148
2003-12-25	PL	$0.26^{+0.03}_{-0.03}$	$\Gamma = 2.18^{+0.09}_{-0.09}$	1.7	2.9	124.2/136
	MCD	$0.07^{+0.02}_{-0.02}$	$T_{\rm in} = 1.06^{+0.06}_{-0.06}$	1.4	2.4	169.3/136
2004-01-08	PL	$0.28^{+0.02}_{-0.02}$	$\Gamma = 2.36^{+0.08}_{-0.07}$	1.2	2.0	119.9/114
	MCD	$0.08^{+0.01}_{-0.01}$	$T_{\rm in} = 0.92^{+0.04}_{-0.04}$	1.0	1.7	216.1/114
2004-01-16	PL	$0.28^{+0.03}_{-0.03}$	$\Gamma = 2.38^{+0.10}_{-0.10}$	1.1	1.9	115.4/122
	MCD	$0.07^{+0.02}_{-0.01}$	$T_{\rm in} = 0.95^{+0.06}_{-0.06}$	0.91	1.5	206.0/122
2004-06-05	PL	$0.30^{+0.02}_{-0.01}$	$\Gamma = 1.79^{+0.04}_{-0.04}$	4.4	7.5	185.0/138
	MCD	$0.11^{+0.01}_{-0.01}$	$T_{\rm in} = 1.62^{+0.05}_{-0.05}$	4.0	6.8	196.0/138
	variable-p	$0.22^{+0.02}_{-0.02}$	$T_{\rm in} = 2.40^{+0.34}_{-0.19}$ / $p = 0.59^{+0.02}_{-0.02}$	4.2	7.1	111.6/137
2004-08-23	PL	$0.21^{+0.02}_{-0.02}$	$\Gamma = 2.28^{+0.10}_{-0.09}$	0.83	1.4	163.5/153
	MCD [d]	0.03	$T_{\rm in} = 0.96$	0.67	1.1	315.9/153
2004-11-23	PL	$0.25^{+0.02}_{-0.02}$	$\Gamma = 2.38^{+0.07}_{-0.07}$	0.92	1.6	207.3/170
	MCD [d]	0.06	$T_{\rm in} = 0.92$	0.76	1.3	444.6/170
2005-02-07	PL	$0.27^{+0.01}_{-0.01}$	$\Gamma = 1.66^{+0.04}_{-0.04}$	4.3	7.3	225.8/141
	MCD	$0.11^{+0.01}_{-0.01}$	$T_{\rm in} = 1.72^{+0.05}_{-0.05}$	3.8	6.5	208.1/141
	variable-p	$0.20^{+0.02}_{-0.02}$	$T_{\rm in} = 2.37^{+0.30}_{-0.23}$ / $p = 0.61^{+0.02}_{-0.02}$	4.0	6.8	161.8/140
2006-03-06	PL	$0.30^{+0.01}_{-0.01}$	$\Gamma = 1.78^{+0.04}_{-0.04}$	4.1	7.0	226.0/141
	MCD	$0.12^{+0.01}_{-0.01}$	$T_{\rm in} = 1.58^{+0.04}_{-0.04}$	3.6	6.1	225.0/141
	variable-p	$0.23^{+0.02}_{-0.02}$	$T_{\rm in} = 2.24^{+0.27}_{-0.20}$ / $p = 0.59^{+0.02}_{-0.02}$	3.8	6.5	162.5/140

[a,b,c,d] The same as table 5.1.

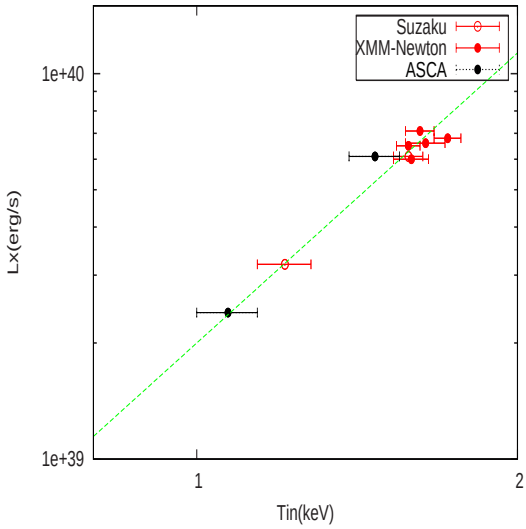

Figure 5.10: The same as figure 5.4, but for NGC1313 Source B, while they are in the MCD-type state.

Figure 5.10 shows the relation between $L_{\rm X}$ and $T_{\rm in}$. Similarly to M81 X-6, we can see that $T_{\rm in}$ increases as the luminosity increases. By fitting the plot by a function of $L \propto T_{\rm in}^{\alpha}$, we obtained $\alpha = 2.5 \pm 0.5$, which is again significantly smaller than the value, 4, of the standard disk. Furthermore, many of the MCD-type spectra are not completely reproduced by the MCD model. We therefore applied a variable-p disk model to them, as well as to those spectra which do not give a clear preference between the PL and MD models. Then, as already reported by Mizuno et al. (2007), the bright-phase *Suzaku* spectra, which exhibits the curvature most prominently, has been reproduced more successfully with ($\chi^2_{\nu} = 0.87$). Furthermore, the variable-p disk model has given acceptable fits to the faint-phase *Suzaku* data, which has an intermediate luminosity. Except for this faint-phase *Suzaku* data, these successful variable-p fits gave the value of $N_{\rm H}$ at $\sim 2 \times 10^{21}$ cm^{-2}, which is consistent with those measured from the lower luminosity spectra using the PL modeling. As plotted in figure 5.11, the obtained value of p is consistent with 0.75 when the source is relatively dim at $L_{\rm X} \sim 3.6 \times 10^{39}$ erg s^{-1}, whereas p decreases to ~ 0.6 when its luminosity increases to $L_{\rm X} \sim 6$–7×10^{39} erg s^{-1}. This property of the MCD-type spectra of this ULX agree with that predicted for the slim-disk state (Watarai et al. 2000).

When the source luminosity is low ($\leq 3 \times 10^{39}$ erg s^{-1}), the EPIC spectra are generally

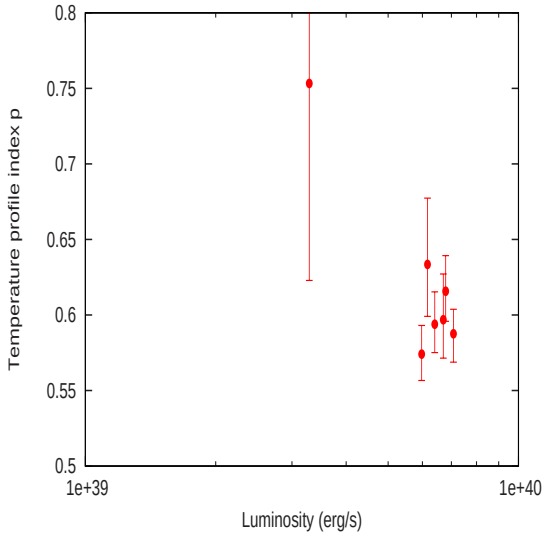

Figure 5.11: The luminosity vs. p relation of NGC1313 Source B, when their spectra in the MCD-type state are fitted by the variable-p disk model.

reproduced well by PL models with $\Gamma = 2.2$–2.4, toghter with $N_{\rm H} \sim 2.7 \times 10^{21}$ cm^{-2}. However, those at the lowest luminosity ($\sim 1.5 \times 10^{39}$ erg s^{-1}), acquired in the first *XMM–Newton* observation, need some caution. In the CCP (figure 5.7), this particular data point has a larger value of HR2 than the other PL-type data sets, while HR1 is not much different. Thus, the spectrum is suggested to be even concave. Indeed, the PL fit in figure 5.8 (bottom left) suggests the same deviation from a single absorbed PL, thus making χ^2_ν marginally large (1.1 for $\nu = 115$). Furthermroe, the value of $N_{\rm H} \sim 2.1 \times 10^{21}$ cm^{-2} from the PL fit is significantly lower than those from the other PL-type spectra. These properties suggest the presence of weak soft excess. This agrees with the previous report by Miller et al. (2003) and Sugiho (2003), that the spectrum from this particular observation exhibits a weak soft excess component described by an MCD model of $T_{\rm in} \sim 0.3$ keV, veiled by the overall PL component.

In order to confirm this suggestion, we re-fitted the dimmest *XMM–Newton* spectrum by a PL plus a cool MCD component. Then, we obtained a better fit with χ^2 decreasing by ~ 15, together with $T_{\rm in} \sim 0.3$ keV. The MCD normalization is subject to large errors as 4^{+43}_{-3}, which translates via eq.2.6 to 700^{+1800}_{-400} km at the assumed 3.7 Mpc. These results are fully consistent with those by Miller et al. (2003). Although our final model to this spectrum invokes an MCD component, it appears as a minor component at the softest end

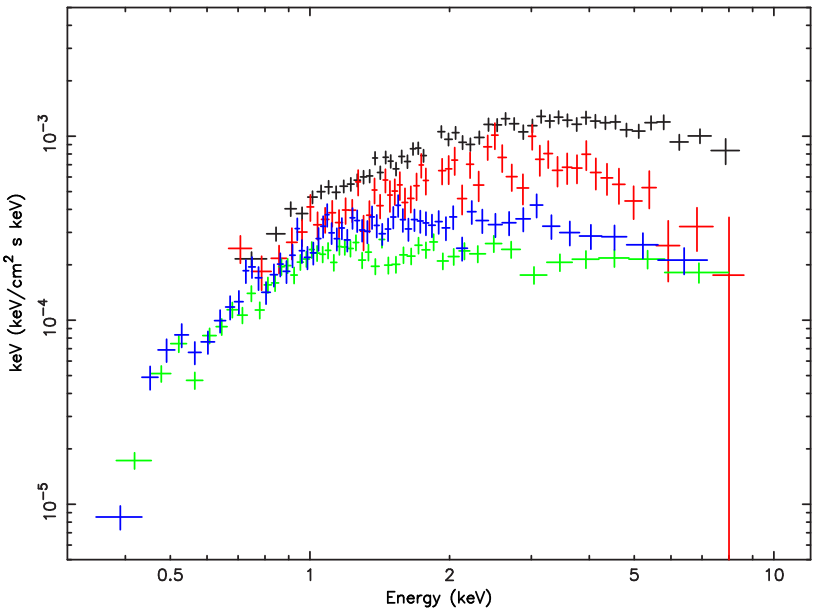

Figure 5.12: The unfolded νF_ν spectra of NGC1313 Source B. The black and red spectra are from the FI CCD data of the *Suzaku* brighter and fainter phases, respectively. The green and blue spectra are from the PN CCD data of the *XMM–Newton* 2000-10-17 and 2004-01-08 observations, respectively.

of the spectrum, in contrast to MCD-type state spectra where the MCD (or variable-p) component with a much higher temperature dominates the entire energy range.

Finally, we present in figure 5.12 the spectra of NGC1313 Source B from typical observations, after unfolding them utilizing their best-fit models. As visualized there, the present analysis of the NGC1313 Source B spectra from the multiple *Suzaku* and *XMM–Newton* observations has given the following results.

1. The spectra prefer the MCD modeling when the source is luminous ($L_{\rm X} \sim 3$–7×10^{39} erg s^{-1}), while the PL modeling when it is dim ($L_{\rm X} \sim 1.3$–3×10^{39} erg s^{-1}).

2. The MCD-type spectra exhibit $T_{\rm in} \sim 1.2$–2 keV, which scales as $L \propto T_{\rm in}^2$. The spectra are reproduced better by a variable-p disk model with $p \sim 0.6$.

3. The PL-type spectra exhibit the photon index of $\Gamma \sim 2.3$. The spectrum obtained at the lowest luminosity exhibits a weak soft excess, which can be described by a cool MCD model with $T_{\rm in} \sim 0.3$ keV.

4. The successful modelings (either PL or variable-p) consistently indicate $N_{\rm H} = 2$–3

$\times 10^{21}$ cm^{-2}.

5.3 Holmberg IX X-1 (M81 X-9)

As described in §§4.1.2, this ULX, sometimes called M81 X-9, was observed a large number of times with *ASCA* , leading to the detection of a clear spectral transition. Here, we analyze four data sets acquired with *XMM–Newton* .

5.3.1 The highest-luminosity data set

Following the same procedure as for the previous two targets, we calculated the hardness ratios from individual observations, and plotted them on the CCP and LCP of figure 5.13. Thus, HR2 significantly decreases when the luminosity increases up to $L_{\rm X} \sim 2 \times 10^{40}$ erg s^{-1} . This indicates that the spectrum in energies above ~ 4 keV becomes softer when the source becomes more luminous.

In order to further evaluate spectral properties, we conducted spectral fitting to the four *XMM–Newton* data sets. First, we fitted the spectrum obtained from the first observation (2001-04-22), which gave the highest luminosity ($L_{\rm X} \sim 2 \times 10^{40}$ erg s^{-1}) among the four occasions; this value is close to the highest luminosity observed with *ASCA* (La Parola et al. 2001, Wang et al. 2001). This particular data set was already analyzed briefly by Sugiho (2003), and in further details by Tsunoda et al. (2006). Similarly to the two ULXs previous analyzed, we tried a PL and an MCD model for its spectral fitting. As summarized in table 5.3, the spectrum prefers an MCD model ($\chi^2/\nu = 379.4/195$) to a PL model ($\chi^2/\nu = 307.0/195$). Furthermore, a variable-p disk fit significantly improves the fit to an acceptable level with $\chi^2/\nu = 209.4/194$ (with a probability of 21% to be acceptable). According to an F-test, the improvement from the MCD fit to the variable-p disk fit is significant with >99%. We show in figure 5.14 (top left) the spectrum together with the best-fit variable-p disk model. The fit again yielded $p = 0.59 \pm 0.02$ which is smaller than that ($p = 0.75$) of the MCD model. These features are consistent with those acquired from M81 X-6 (§5.1) and NGC1313 Source B (§5.2), so that this ULX is implied to have been in the slim-disk state on that occasion. This result is fully consistent with those by Sugiho (2003) and Tsunoda et al. (2006) who used the same dataset.

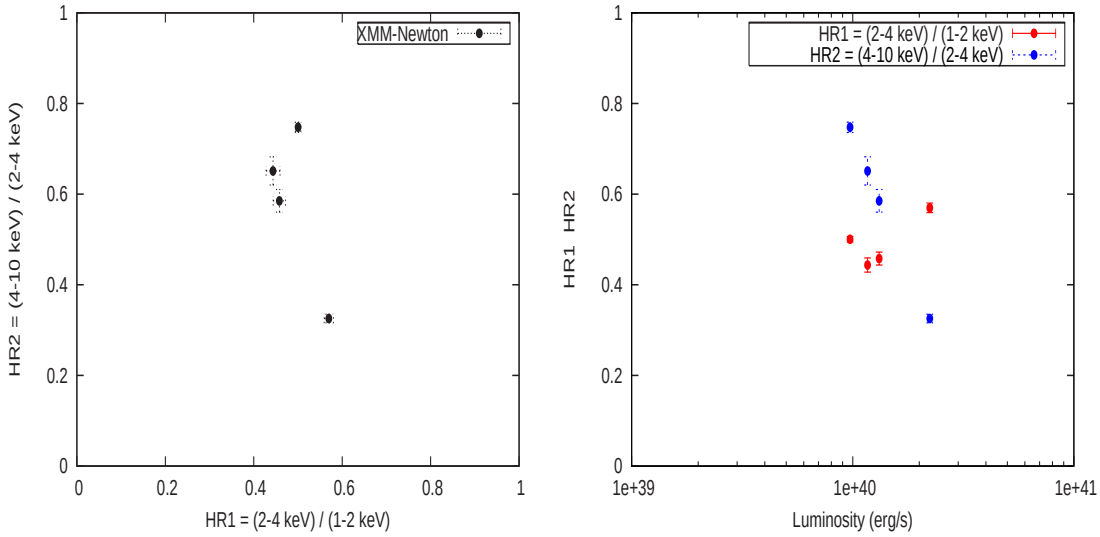

Figure 5.13: The CCP (left) and LCP (right) of Holmberg IX X-1, acquired by the four *XMM–Newton* observations.

5.3.2 Lower-luminosity data sets

Following the most luminous spectrum exhibiting the MCD-type property, we fitted the spectra from the fourth observation (2004-09-26), because it has a longer exposure ($\sim$ 100 ks) than the other two. This data set was already analyzed by Dewangan et al. (2006). On this occasion, the source was dimmest at $L_{\rm X} \sim 1 \times 10^{40}$ erg s^{-1}. As before, we first tried a PL and an MCD model, and obtained the results shown in figure 5.15 (left panels) in the form of spectral ratio to each model. As seen in the top two panels, the spectrum favors a PL rather than an MCD model, in contrast to the first observation. This implies that the spectrum corresponds to the PL-type. However, the fit is still unacceptable with $\chi^2/\nu = 1436.1/300$, as evidenced by a mild excess in the 0.5–2 keV range, and a flux decline above $\sim$ 6 keV.

In order to evaluate the high-energy spectral shape free from the soft-excess effect, we next restricted the energy band to $\geq$ 2 keV, and tried a PL model with the absorption fixed to 2×10^{21} cm^{-2}. As shown in the third panel in figure 5.15, the fit is unacceptable ($\chi^2/\nu = 215.2/115$) because of the mild flux decline above $\sim$ 6 keV. To reproduce this feature, we applied a so-called cutoff-PL model, which is a PL model multiplied by an exponential cutoff factor as,

$$\propto E^{-\Gamma} \times \exp(-E/E_{\rm cut}). \tag{5.2}$$

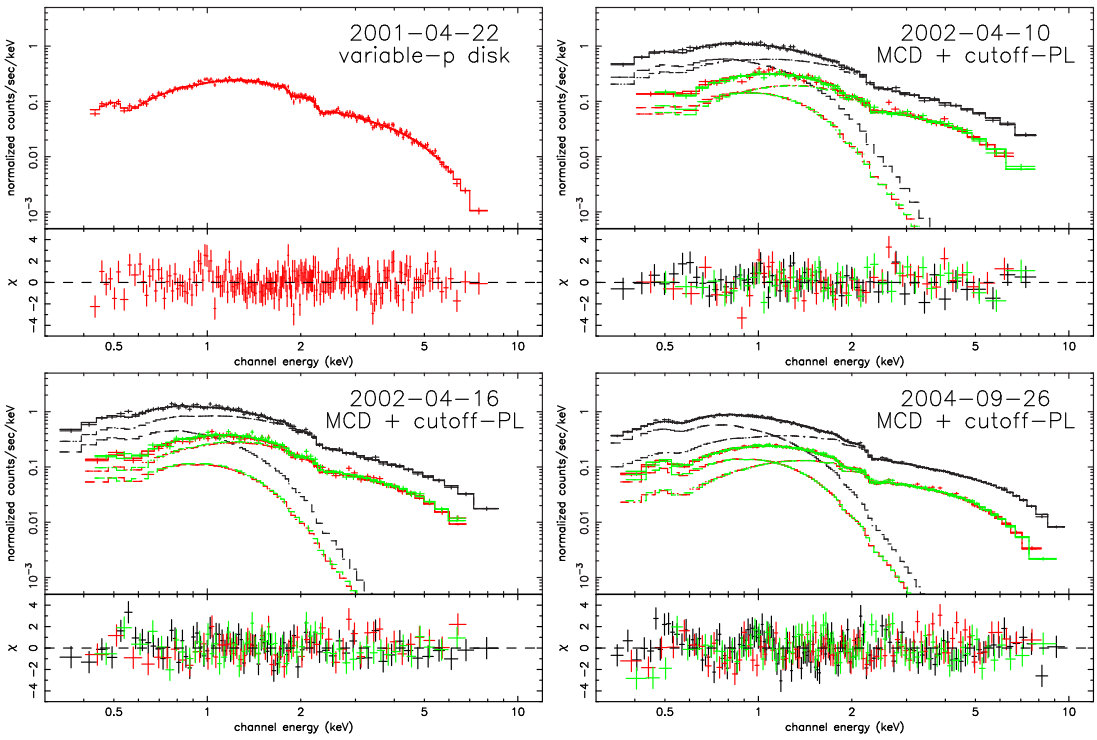

Figure 5.14: Background-subtracted spectra of Holmberg IX X-1 obtained with the *XMM–Newton* in four observations, together with the best-fit models (dates and best-fit models are indicated in individual panels). The PN, MOS1, and MOS2 data are shown in black, red, and green, respectively.

As shown in the forth panel in figure 5.15, we then obtained a better fit with $\chi^2/\nu = 157.8/114$, together with a cutoff energy of $E_{\rm cut} \sim 11$ keV. Using F-test, the fit improvement is significant with >99%. Thus, the continuum is inferred to exhibit a mildly curving shape toward higher energies, instead of a straight PL form.

Since the spectrum in the ≥ 2 keV band has been reproduced by the cutoff-PL model, we further evaluate the soft band continuum to account for the soft-excess effect. We tried to reproduce the soft-excess by adding a steep ($\Gamma \sim 4.7$) PL component on top of the fixed cutoff-PL model determined in the ≥ 2 keV band. However, as shown in the fifth panel in figure 5.15, the obtained fit is unacceptable ($\chi^2/\nu = 938.9/300$), because this modeling require a large absorption ($N_{\rm H} = 4.3 \times 10^{21}$ cm^{-2}) which over-predict the oxygen edge at 0.53 keV. Therefore, the soft excess should not be increasing as steeply toward lower energies as represented by such a soft PL. Accordingly, we applied an MCD model in place of the PL model. As shown in the lowest panel in figure 5.15, the fit has become approximately acceptable ($\chi^2/\nu = 437.6/300$), with $T_{\rm in} \sim 0.3$ keV. This suggests that the spectrum has a separate soft-excess component that can be reproduced successfully by an MCD model with $T_{\rm in} \sim 0.3$ keV.

Finally, we fit the overall 0.3–10 keV spectrum using the MCD plus cutoff-PL model, leaving all the model parameters free, as shown in figure 5.14 (bottom right). The obtained $\chi^2/\nu = 391.0/297$ is the smallest of our fits, and the cutoff energy and inner-disk temperature have been obtained as $E_{\rm cut} \sim 6$ keV and $T_{\rm in} \sim 0.3$ keV, respectively. The normalization of the MCD model, 11^{+3}_{-2}, yields the inner-disk radius as $R_{\rm in} = 1200^{+200}_{-100}$ km, assuming a distance of 3.6 Mpc and an inclination of 0°. The obtained absorption, $N_{\rm H} \simeq 1.4 \times 10^{21}$ cm^{-2}, is roughly the same as derived with the MCD-type spectrum.

Because the PL-type spectrum has thus been found to be accompanied by a soft-excess component and a high-energy cutoff factor, we evaluated the other two (2002-04-10 and 2002-04-16) spectra with the same MCD plus cutoff-PL model. The spectra are shown in figure 5.14 (top right and bottom left), and the fitting results are summarized in table 5.3, together with those from the other simple models; PL, MCD, and MCD plus PL. Again, the cool MCD plus cutoff-PL model is most successful on the second and third data sets. The absorbing column obtained from the dimmer (PL-type) spectra using the MCD + cutoff-PL model, $N_{\rm H} = (1.4$–$1.7) \times 10^{21}$ cm^{-2}, is roughly the same as that (1.8×10^{21} cm^{-2}) of the most luminous spectrum determined with the variable-p disk model. The

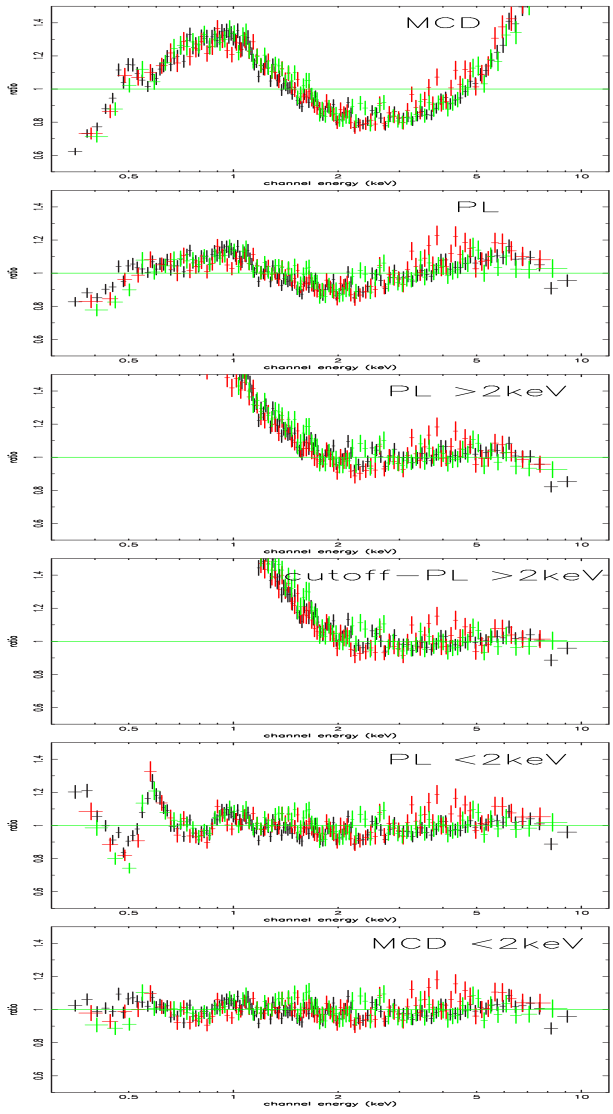

Figure 5.15: The XMM-EPIC spectral ratios to the model described in each panel (see text for details) of Holmberg IX X-1, obtained in the fourth observation.

Table 5.3: Summary of model fits to the *Suzaku* and *XMM–Newton* spectra of Holmberg IX X-1. [a,b]

	Model	$N_{\rm H}$ (10^{22} cm^{-2})	Parameters	$F_{\rm X}$ [c]	$L_{\rm X}$ [c]	χ^2/ν
			XMM–Newton			
2001-04-22	PL	$0.27^{+0.01}_{-0.01}$	$\Gamma = 1.89^{+0.03}_{-0.03}$	15	25	379.4/195
	MCD	$0.079^{+0.006}_{-0.006}$	$T_{\rm in} = 1.38^{+0.03}_{-0.03}$	13	21	307.0/195
	variable-p	$0.18^{+0.02}_{-0.03}$	$T_{\rm in} = 1.85^{+0.14}_{-0.11}$ / $p = 0.59^{+0.02}_{-0.02}$	14	22	209.4/194
2002-04-10	PL	$0.15^{+0.01}_{-0.01}$	$\Gamma = 1.78^{+0.03}_{-0.03}$	7.1	11	200.4/151
	MCD [d]	0.01	$T_{\rm in} = 1.48$	6.0	9.6	773.1/151
	MCD	$0.17^{+0.03}_{-0.01}$	$T_{\rm in} = 0.30^{+0.04}_{-0.06}$	0.45	0.72	158.2/149
	+ PL		$\Gamma = 1.61^{+0.08}_{-0.06}$	6.8	11	
	MCD	$0.15^{+0.03}_{-0.03}$	$T_{\rm in} = 0.33^{+0.05}_{-0.06}$	0.85	1.4	154.6/148
	+ cutoff-PL		$\Gamma = 1.03^{+0.55}_{-0.61}$ / $E_{\rm cut} = 7.2^{+78.0}_{-3.5}$	6.2	9.9	
2002-04-16	PL	$0.18^{+0.01}_{-0.01}$	$\Gamma = 1.84^{+0.03}_{-0.03}$	8.1	13	216.9/190
	MCD [d]	0.03	$T_{\rm in} = 1.43$	7.0	11	877.3/190
	MCD	$0.21^{+0.03}_{-0.02}$	$T_{\rm in} = 0.24^{+0.07}_{-0.05}$	0.26	0.42	199.2/188
	+ PL		$\Gamma = 1.78^{+0.05}_{-0.05}$	8.0	13	
	MCD	$0.17^{+0.04}_{-0.03}$	$T_{\rm in} = 0.31^{+0.08}_{-0.08}$	0.62	0.99	194.4/187
	+ cutoff-PL		$\Gamma = 1.31^{+0.37}_{-0.56}$ / $E_{\rm cut} = 9.0^{+23.0}_{-5.7}$	7.4	12	
2004-09-26	PL [d]	0.11	$\Gamma = 1.60$	6.0	9.6	1436.1/300
	MCD [d]	0	$T_{\rm in} = 1.81$	5.4	8.6	7064.1/300
	PL ($\geq$ 2 keV)	0.2(fixed)	$\Gamma = 1.48^{+0.02}_{-0.02}$			215.2/115
	cutoff-PL ($\geq$ 2 keV)	0.2(fixed)	$\Gamma = 1.11^{+0.08}_{-0.08}$ / $E_{\rm cut} = 11.1^{+3.1}_{-2.0}$			157.8/114
	PL ($\leq$ 2 keV) [d]	0.43	$\Gamma = 4.68$			938.9/300
	MCD ($\leq$ 2 keV)	$0.17^{+0.01}_{-0.01}$	$T_{\rm in} = 0.25^{+0.01}_{-0.01}$			437.6/300
	MCD	$0.14^{+0.01}_{-0.003}$	$T_{\rm in} = 0.31^{+0.01}_{-0.02}$	0.77	1.2	391.0/297
	+ cutoff-PL		$\Gamma = 0.70^{+0.15}_{-0.13}$ / $E_{\rm cut} = 6.0^{+1.3}_{-0.9}$	5.3	8.5	

[a] All quoted errors are 90% confidence regions.

[b] The temperatures of parameters are in the units of keV.

[c] The 0.5–10 keV absorption uncorrected flux in 10^{-12} erg s^{-1}cm^{-2} and luminosity in 10^{39} erg s^{-1} .

[d] Errors are not shown since the fit is far from acceptable.

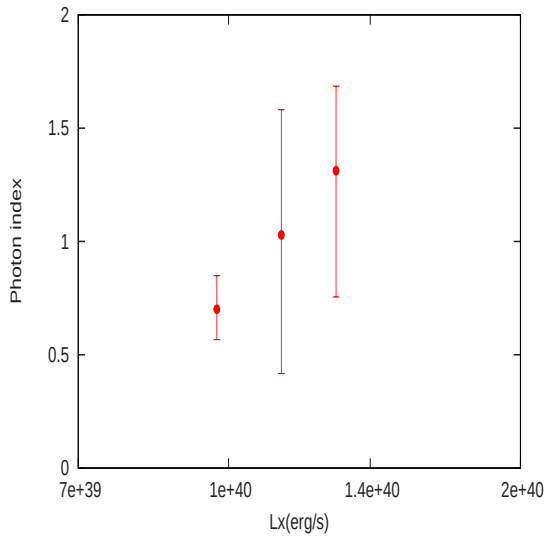

Figure 5.16: The photon index vs. luminosity relations of the three PL-type spectra.

temperature ($T_{\rm in} \sim 0.3$ keV) and luminosity (1.0–1.4 $\times 10^{39}$ erg s^{-1}) of the cool MCD component determined in this was are almost the same within errors as those of the forth observation, whereas the dominant cutoff-PL component increases from the fourth to the second, and then to the third observations. Figure 5.16 shows a relation between the luminosity and the photon index, where we can see that the photon index steepens as the source becomes more luminous, while the cutoff energy tends to increase, thus making the high energy continuum less convex. This feature is reflected in the CCP (figure 5.13) as a decrease in HR2 when the luminosity increases.

Finally, we show unfolded spectra of Holmberg IX X-1 in figure 5.17. From these, our results on Holmberg IX X-1 can be summarized in the following way.

1. Similar to NGC1313 Source B, this ULX exhibits a spectral bimodelity between the MCD-type ($L_{\rm X} \sim 2 \times 10^{40}$ erg s^{-1}) and the PL-type ($L_{\rm X} \sim 0.8$–1×10^{40} erg s^{-1}) states. The former was observed in the most luminous occasion, while the latter on the dimmer occasions.

2. The MCD-type spectrum (black in figure 5.17) is reproduced successfully by a variable-p disk model with $T_{\rm in} \sim 1.9$ keV and $p \sim 0.6$, which resembles those observed from Galactic BHBs in the slim-disk state.

3. The PL-type spectrum (blue in figure 5.17), obtained by a long observation, clearly

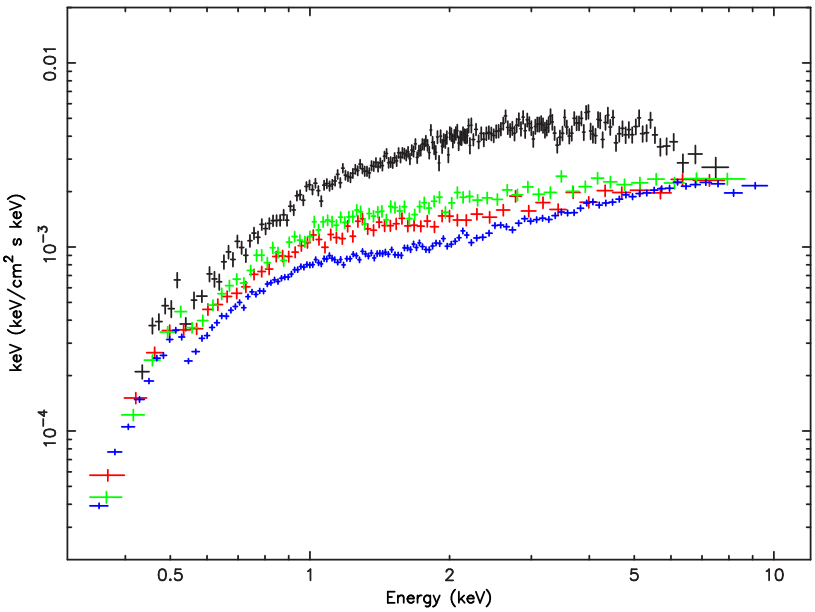

Figure 5.17: Unfolded spectra of Holmberg IX X-1 obtained with *XMM–Newton* . The black spectrum is from the MOS1 data of the first observation (2001-04-22), while the red, green, and blue spectra are from the PN data of the 2002-04-10, 2002-04-16, and 2004-09-26 observations, respectively.

exhibits a soft excess component represented by an MCD model with $T_{\rm in} \sim 0.3$ keV and $R_{\rm in} \sim 1200$ km. Furthermore, the spectrum also shows an exponential cutoff above ~ 6 keV.

4. The PL-type spectrum becomes softer when its luminosity increases (blue, red, and green in figure 5.17), in resemblance to the PL-type spectrum of NGC1313 Source B.

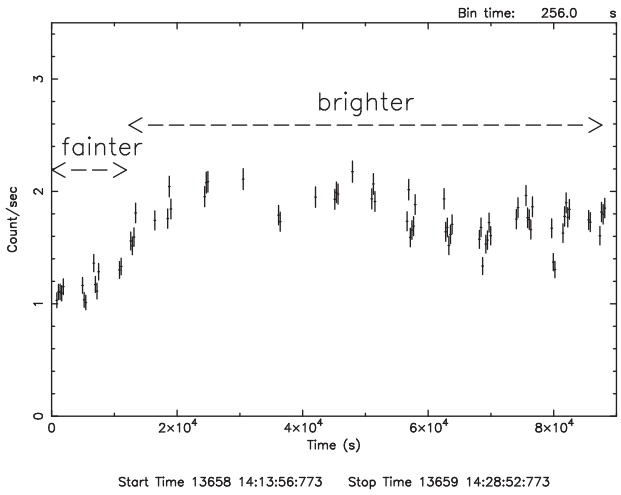

Figure 5.18: The background-subtracted 0.5–10 keV lightcurve of NGC1313 Source A obtained by the *Suzaku* XIS.

5.4 NGC1313 Source A

This ULX, called NGC1313 Source A, exhibits PL-like spectra (§§4.1.2) in contrast to Source B (§§5.2) in the same galaxy. Here, we analyze multiple data sets obtained with *Suzaku* and *XMM–Newton* . Like NGC1313 Source B, the *Suzaku* results were already published as Mizuno et al. (2007), but we perform a more detailed and unified analysis, together with those from *XMM–Newton* .

As shown in figure 5.18, during the *Suzaku* observation, this source became brighter by $\sim 50\%$; therefore, we divided the *Suzaku* -XIS data into two periods, namely fainter (the former ~ 6 ks) and brighter (the latter ~ 22 ks) phases, and analyzed their spectra separately. Like the previously analyzed three targets, we derived hardness ratios from the individual *Suzaku* and *XMM–Newton* observations (§§4.1.1), and plotted them on the CCP and LCP in figure 5.19.

As seen from figure 5.19, the luminosity of this ULX varied in the range of 3–10 $\times 10^{39}$ erg s^{-1} among the *XMM–Newton* observations. As the luminosity increases, the source varied on the CCP from HR2 ~ 0.7 to ~ 0.3 along a line of HR1 ~ 0.4, except for the data point in the faintest phase which is located at HR1 ~ 0.2 and HR2 ~ 0.2. In the *Suzaku* observation, in contrast, this ULX became more luminous to 1.5–2.2 $\times 10^{40}$ erg s^{-1} , and moved on the CCP to HR1 $\sim$ 0.6–0.8.

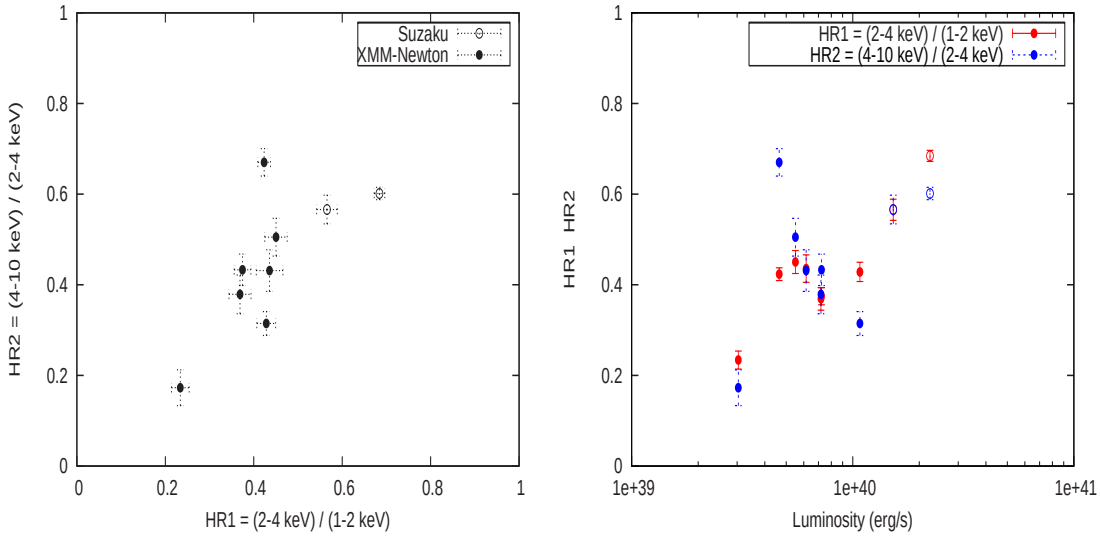

Figure 5.19: The CCP (left) and LCP (right) of NGC1313 Source A, acquired in the *XMM–Newton* and *Suzaku* observations.

5.4.1 *XMM–Newton* spectra

In order to more quantitatively evaluate the properties seen in the CCP and LCP, we conducted spectral fitting for the *XMM–Newton* data. As before, we first tried a PL model and an MCD model, multiplied by a model of photoelectric absorption. As summarized in table 5.4, all *XMM–Newton* spectra preferred a PL model to an MCD model, and the MCD fits were unacceptable. This suggests that the source was in the PL-type state in all these *XMM–Newton* observations.

Figure 5.20 (top left) presents the *XMM–Newton* spectra from the 1st observation, acquired at $L_{\rm X} \sim 5 \times 10^{39}$ erg s^{-1}. The PL fit, though much better than the MCD modeling (table 5.4), was not yet fully acceptable. The fit was much improved by adding a cool ($T_{\rm in} \sim 0.3$ keV) disk component, and further applying a high-energy cutoff (table 5.4). These features are similar to those observed from Holmberg IX X-1 in the previous section. In the 2nd, 3rd, and 4th *XMM–Newton* observations, this ULX became luminous at $\sim$ 7–10 $\times 10^{39}$ erg s^{-1}, and the spectra became softer ($\Gamma \sim 2.3$) as shown in figure 5.20 (top right). In the 5th observation (2004-08-23), this source in contrast became the dimmest at $\sim 3 \times 10^{39}$ erg s^{-1} (figure 5.20 bottom left). At that time the spectrum became very soft, represented by a PL model with $\Gamma \sim 2.8$ plus a cool MCD model with $T_{\rm in} \sim 0.2$ keV. On the 6th and 7th occasions (figure 5.20 bottom right), the luminosity was about

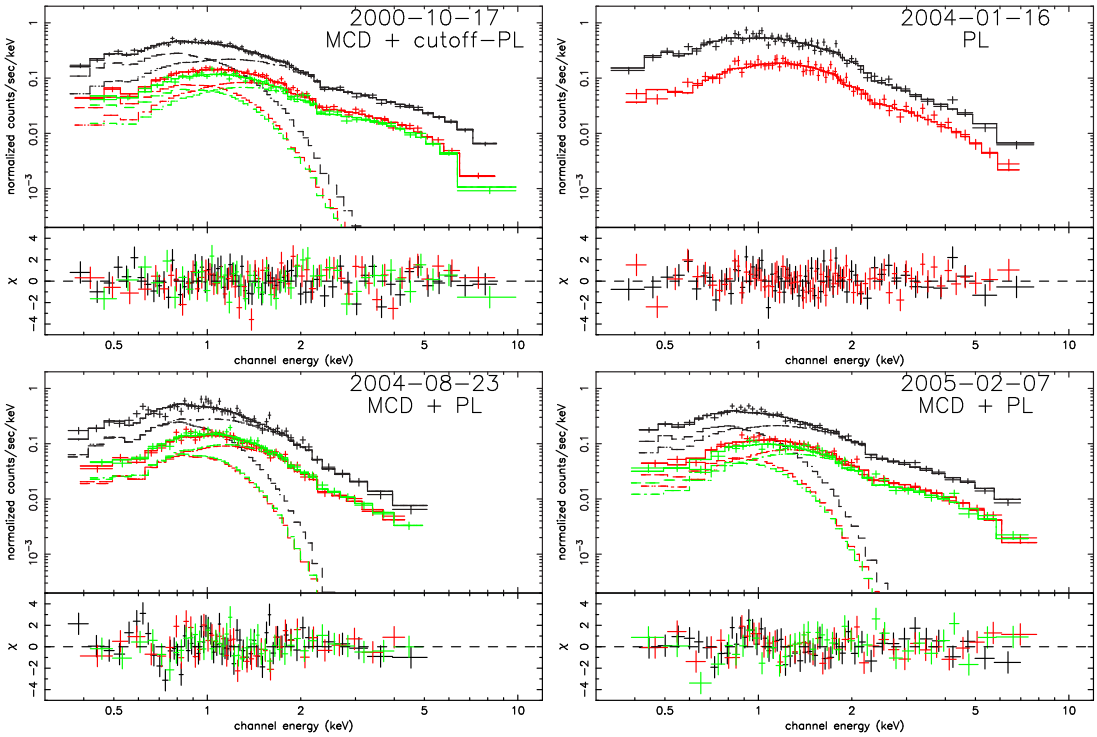

Figure 5.20: Background-subtracted spectra of NGC1313 Source A obtained with *XMM–Newton* in the four observations, shown together with the best-fit models. The dates and the best-fit models are indicated in individual panels. The PN, MOS1, and MOS2 data are shown in black, red, and green, respectively.

the same as the 1st one ($L_{\rm X} \sim 5 \times 10^{39}$ erg s^{-1}).

Among these *XMM–Newton* observations, the obtained temperature and luminosity of the MCD component are relatively constant at $T_{\rm in} \sim 0.2$–0.3 keV and $L_{\rm X} \sim 5$–8 $\times 10^{38}$ erg s^{-1} , respectively. On the contrary, the luminosity of the PL component varied over $L_{\rm X} \sim 3$–12 $\times 10^{39}$ erg s^{-1} . Figure 5.22 describes the relation between the photon index and luminosity of the PL component, obtained in the *XMM–Newton* observations. Thus, the photon index increases from ~ 1.2 to ~ 2.4 as the luminosity increases. However, at the faintest occasion the photon index becomes as large as ~ 2.8. From this feature, this ULX is inferred to be in another spectral state than the PL-type at its lowest luminosity.

In table 5.4, the value of $N_{\rm H}$ scatters 2–4 $\times 10^{21}$ cm^{-2} among observations even in the best-fit model. Since $N_{\rm H}$ is unlikely to vary with time, we regard this as an artifact caused by different model shapes.

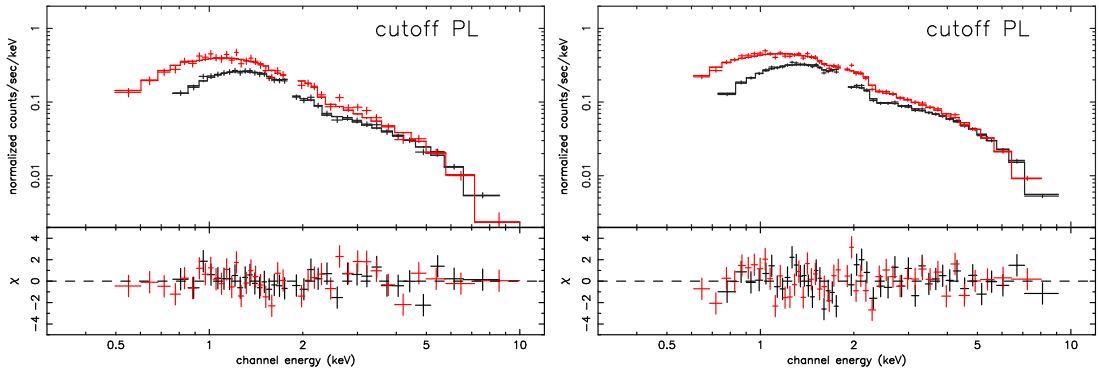

Figure 5.21: Background-subtracted *Suzaku* spectra of NGC1313 Source A obtained in the fainter (left) and brighter (right) phases, presented together with the best-fit cutoff-PL models. The FI and BI CCD data are shown in black and red, respectively.

5.4.2 *Suzaku* spectra

As seen in the CCP and LCP in figure 5.19, this ULX became considerably brighter in the *Suzaku* observation than in the *XMM–Newton* ones, and is expected to exhibit possibly different spectral states. As summarized in table 5.4, the fainter (former 6 ks) phase spectra were reproduced successfully by a PL model with $\Gamma \sim 2.0$ with $\chi^2/\nu = 77.5/70$ (with a probability of 25% to be acceptable), whereas the MCD model gave an unacceptable fit with $\chi^2/\nu = 183.1/70$. Furthermore, its spectra were slightly convex, rather than a simple PL. Accordingly, we re-fitted them with a cutoff-PL model, to find that the fit is improved with >99% significance by F-test with a cutoff energy of $E_{\rm cut} \sim 8$ keV. The spectrum with the best-fit cutoff-PL model is shown in figure 5.21 (left). This modeling is the same as the final solution adopted by Mizuno et al. (2007), and the parameters obtained here agree with theirs.

In the brighter (latter 22 ks) phase, the spectra became more convex, as already reported by Mizuno et al. (2007). Indeed, the PL fit to them was totally unsuccessful (table 5.4). Instead, they were well described by a cutoff-PL model ($\chi^2/\nu = 123.2/87$) with $E_{\rm cut} \sim 3.7$ keV, as shown in figure 5.21 (right). On the other hand, the variable-p disk model also reproduced the same XIS spectra with a comparable goodness ($\chi^2/\nu = 121.9/87$), yielding $T_{\rm in} \sim 2.1$ keV and $p \sim 0.6$, which are close to those from the MCD-type spectra described previouly (M81 X-6, NGC1313 Source B, and Holmberg IX X-1).

Table 5.4: Summary of model fits to the *XMM–Newton* and *Suzaku* spectra of NGC1313 Source A. [a,b]

	Model	$N_{\rm H}$ (10^{22} cm^{-2})	Parameters	$F_{\rm X}$ [c]	$L_{\rm X}$ [c]	χ^2/ν
			XMM–Newton			
2000-10-17	PL [d]	0.17	1.85	2.7	4.6	370.1/173
	MCD [d]	0.01	$T_{\rm in} = 1.46$	2.3	3.9	1236.4/173
	MCD	$0.25^{+0.04}_{-0.01}$	$T_{\rm in} = 0.23^{+0.02}_{-0.03}$	0.26	0.44	207.5/171
	+ PL		$\Gamma = 1.66^{+0.06}_{-0.04}$	2.5	4.3	
	MCD	$0.23^{+0.03}_{-0.03}$	$T_{\rm in} = 0.25^{+0.05}_{-0.03}$	0.35	0.60	200.7/170
	+ cutoff-PL		$\Gamma = 1.21^{+0.25}_{-0.25}$ / $E_{\rm cut} = 9.2^{+7.1}_{-4.4}$	2.4	4.1	
2004-01-08	PL	$0.29^{+0.02}_{-0.02}$	$2.27^{+0.07}_{-0.07}$	4.1	7.0	71.1/56
	MCD [d]	0.09	$T_{\rm in} = 1.03$	3.5	6.0	292.3/56
	MCD	$0.30^{+0.07}_{-0.04}$	$T_{\rm in} = 0.28^{+0.08}_{-0.08}$	0.41	0.70	53.9/54
	+ PL		$\Gamma = 2.02^{+0.16}_{-0.17}$	3.8	6.5	
2004-01-16	PL	$0.32^{+0.02}_{-0.02}$	$\Gamma = 2.36^{+0.07}_{-0.07}$	4.2	7.1	134.2/134
	MCD	$0.11^{+0.01}_{-0.01}$	$T_{\rm in} = 0.98^{+0.05}_{-0.04}$			254.8/134
2004-06-05	PL	$0.34^{+0.02}_{-0.02}$	$\Gamma = 2.32^{+0.06}_{-0.05}$	6.3	11	174.5/149
	MCD [d]	0.11	$T_{\rm in} = 1.04$	5.4	9.2	347.9/149
2004-08-23	PL	$0.39^{+0.02}_{-0.02}$	$\Gamma = 3.26^{+0.10}_{-0.10}$	1.7	2.9	220.3/136
	MCD [d]	0.12	$T_{\rm in} = 0.56$	1.5	2.6	396.5/136
	MCD	$0.41^{+0.05}_{-0.06}$	$T_{\rm in} = 0.18^{+0.04}_{-0.02}$	0.32	0.54	177.0/134
	+ PL		$\Gamma = 2.84^{+0.08}_{-0.11}$	1.5	2.6	
2004-11-23	PL	$0.23^{+0.02}_{-0.02}$	$2.05^{+0.08}_{-0.07}$	3.3	5.6	130.2/96
	MCD [d]	0.04	$T_{\rm in} = 1.17$	2.8	4.8	295.2/96
	MCD	$0.24^{+0.06}_{-0.04}$	$T_{\rm in} = 0.30^{+0.07}_{-0.07}$	0.46	0.78	99.4/94
	+ PL		$\Gamma = 1.65^{+0.19}_{-0.22}$	3.2	5.4	
2005-02-07	PL	$0.19^{+0.02}_{-0.01}$	$1.93^{+0.06}_{-0.05}$	3.1	5.3	199.2/126
	MCD [d]	0.02	$T_{\rm in} = 1.32$	2.6	4.4	440.9/126
	MCD	$0.30^{+0.08}_{-0.04}$	$T_{\rm in} = 0.21^{+0.03}_{-0.04}$	0.32	0.54	140.1/124
	+ PL		$\Gamma = 1.74^{+0.11}_{-0.08}$	2.9	4.9	
			Suzaku 2005-10-15			
brighter	PL [d]	0.31	1.89	14	24	416.5/88
	MCD [d]	0.04	$T_{\rm in} = 1.61$	13	22	275.2/88
	variable-p	$0.17^{+0.02}_{-0.02}$	$T_{\rm in} = 2.13^{+0.11}_{-0.10}$ / $p = 0.60^{+0.01}_{-0.01}$	13	22	121.9/87
	cutoff-PL	$0.14^{+0.02}_{-0.02}$	$\Gamma = 0.93^{+0.09}_{-0.10}$ / $E_{\rm cut} = 3.7^{+0.4}_{-0.3}$	13	22	123.2/87
fainter	PL	$0.27^{+0.02}_{-0.02}$	$2.04^{+0.05}_{-0.05}$	9.2	16	77.5/70
	MCD [d]	0.02	$T_{\rm in} = 1.37$	8.5	14	183.1/70
	cutoff-PL	$0.20^{+0.04}_{-0.04}$	$\Gamma = 1.61^{+0.22}_{-0.22}$ / $E_{\rm cut} = 7.7^{+7.3}_{-2.6}$	9.0	15	65.9/69

[a,b,c,d] The same as table 5.1.

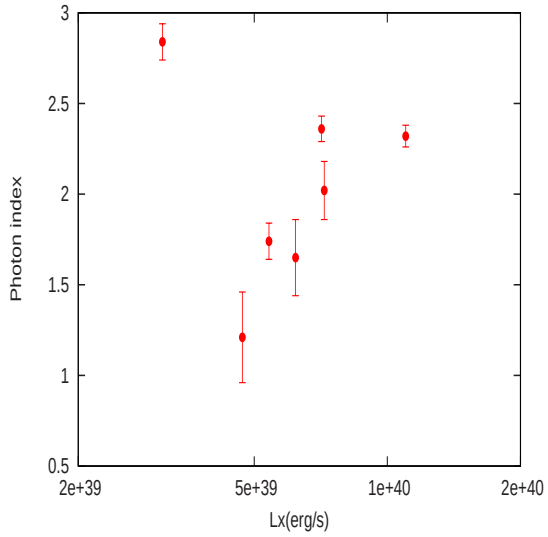

Figure 5.22: A scatter plot between the photon index and luminosity of the dominant PL component, measured in the *XMM–Newton* observations.

We present in figure 5.23 unfolded spectra from some typical data of NGC1313 Source A. From these spectral analysis, we have obtained the following results.

1. In the *XMM–Newton* observations (green, blue, and cyan in figure 5.23), this ULX exhibited a PL-type spectra, which are sometimes accompanied by a soft-excess component and a high-energy decline.

2. In the range of $\sim$ 5–10 $\times 10^{39}$ erg s^{-1}, the PL-type spectral slope becomes softer ($\Gamma \sim$ 1.2–2.4) as the luminosity increases (green and blue in figure 5.23).

3. When the luminosity becomes the lowest at $L_{\rm X} \sim 3 \times 10^{39}$ erg s^{-1}, its spectrum became very soft, described by an MCD ($T_{\rm in} \sim 0.2$ keV) plus a PL ($\Gamma \sim 2.8$) model, which may correspond to another spectral state.

4. In the *Suzaku* observation (black and red in figure 5.23), this ULX became rather luminous at $L_{\rm X} \sim$ 1.5–2.2 $\times 10^{40}$ erg s^{-1}. At the brighter phase, its spectra exhibited a significantly convex shape, and were reproduced by a cutoff-PL model with $E_{\rm cut} \sim$ 4 keV, or alternatively by a variable-p disk model with $p \sim 0.6$.

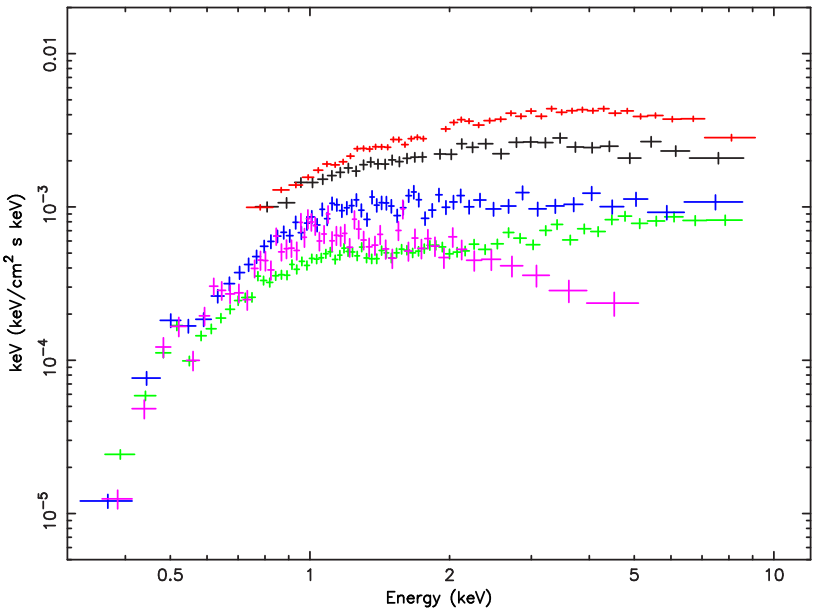

Figure 5.23: Unfolded spectra of NGC1313 Source A. The black and red spectra are from the FI data of the *Suzaku* observation, while the green, blue and cyan spectra are from the PN data of the *XMM–Newton* 2000-10-17, 2004-01-08, and 2004-08-23 observations, respectively.

5.5 Other ULXs

Following the four ULXs analyzed so far, here we describe spectral analysis of the other three targets: Holmberg II X-1, NGC5204 X-1, and IC342 Source 1.

5.5.1 Holmberg II X-1

Similar to the previously analyzed targets, we show in figure 5.24 the CCP and LCP, summarized in table 5.5 the best-fit parameters, and in figure 5.25 unfolded spectra of Holmberg II X-1 acquired in the four observations with *XMM–Newton* (§§4.1.1). This ULX exhibited an luminosity of $\sim 1 \times 10^{40}$ erg s^{-1} on three of the four *XMM–Newton* observations (2002-04-10, 2002-04-16, and 2004-04-15). On these occasions, the spectra were better reproduced by a PL model than by and MCD model, but the PL fit was not generally acceptable yet. As summarized in table 5.5, the fits became acceptable by adding a soft MCD component, and applying an exponential cutoff factor to the PL continuum. These spectral properties agree with those in the PL-type spectra observed in Holmberg IX X-1

and NGC1313 Source A.

On the third occasion (2002-09-18), this source became fainter down to $L_{\rm X} \sim 2 \times 10^{39}$ erg s^{-1}. At that time, it exhibited a very soft spectrum represented by a PL model ($\Gamma \sim 3$), with a soft excess described by an MCD model ($T_{\rm in} \sim 0.2$ keV). These properties resemble those observed in the faintest occasion of NGC1313 Source A. These results are fully consistent with those reported by Dewangan et al. (2004) and Goad et al. (2005) using the same data.

5.5.2 NGC5204 X-1

In the three observations with *XMM–Newton* (§§4.1.1), this ULX, NGC5204 X-1, exhibited a luminosity of $\sim$ 4–6 $\times 10^{40}$ erg s^{-1}. The CCP and LCP, the fitting parameters, and the unfolded spectra are presented in figure 5.26, table 5.6, and figure 5.27, respectively. Like the case of many other ULXs, these spectra were reproduced successfully by a PL model ($\Gamma \sim 1.7$–2.2), when an MCD model of $T_{\rm in} \sim 0.2$–0.3 keV was added to describe soft excess. These results are fully consistent with those reported by Roberts et al. (2004). Like the other PL-type ULXs, we can see in the LCP (figure 5.26) and the unfolded spectra (figure 5.27) that the spectra became slightly softer when the luminosity increases.

5.5.3 IC342 Source 1

This ULX, IC342 Source 1 (§§4.1.2), is a prototypical object, which played an important role in the recognition of "BH-like spectra" of ULXs (Okada et al. 1998; Makishima et al. 2000; Mizuno et al. 2001), as well as their spectral transitions (Kubota et al. 2001). It was observed four times with *XMM–Newton* (§§4.1.1). The CCP and LCP are given in figure 5.28, while the derived fitting parameters and unfolded spectra of this ULX are presented in table 5.7 and figure 5.29, respectively. Because this object has a higher absorbing column ($N_{\rm H} \sim 6 \times 10^{21}$ cm^{-2}) than the other targets, the values of HR1 become larger ($\sim$ 0.8), and cannot be simply compared with those of the other ULXs. In the 1st (2001-02-11) and 3rd (2004-08-17) observations, this ULX was relatively dim ($L_{\rm X} \sim 5 \times 10^{39}$ erg s^{-1}), and the spectra were well described by a PL model with $\Gamma \sim 1.7$. On the other hand, in the 2nd (2004-02-20) and 4th (2005-02-10) observations, it became

more luminous ($L_{\rm X} \sim$ 1.0–1.3 $\times 10^{40}$ erg s^{-1}) and the spectra exhibited a more convex shape that can be better approximated by an MCD model than by a PL model. These high-luminosity spectra are well described by a cutoff-PL model with $E_{\rm cut} \sim$ 6–7 keV, or alternatively, by a variable-p disk model with $T_{\rm in} \sim$ 2.7 keV and $p \sim$ 0.5–0.6.

For reference, the 2nd *ASCA* observation conducted in 2000 found this source in a typical PL-type state, of which the parameters ($\Gamma = 1.77$ and $L_{\rm X} = 6 \times 10^{39}$ erg s^{-1}; Kubota et al. 2001) are very close to those obtained in the 3rd *XMM–Newton* observation. In contrast, the object was in a typical MCD state with $T_{\rm in} = 1.8$ keV during the 1st *ASCA* observation made in 1993 (Okada et al. 1998; Kubota et al. 2001). The observed 0.5–10 keV luminosity (1.9×10^{40} erg s^{-1}) was $\sim 50\%$ higher than that of the 4th *XMM–Newton* observation. Thus, the *ASCA* results are consistent with those obtained in the present work, in the sense that the spectrum become PL-type and MCD-type, at luminosities below and above $\sim$ 5–10 $\times 10^{39}$ erg s^{-1}, respectively. Therefore, this source retains its important position as a prototypical state-transition object.

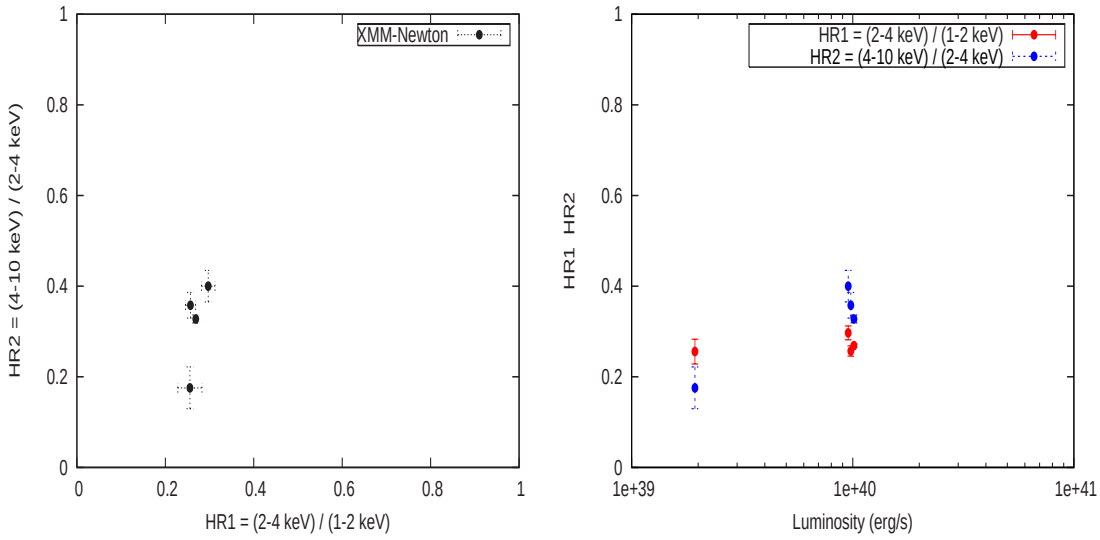

Figure 5.24: The CCP (left) and LCP (right) of Holmberg II X-1, acquired in the *XMM–Newton* observations.

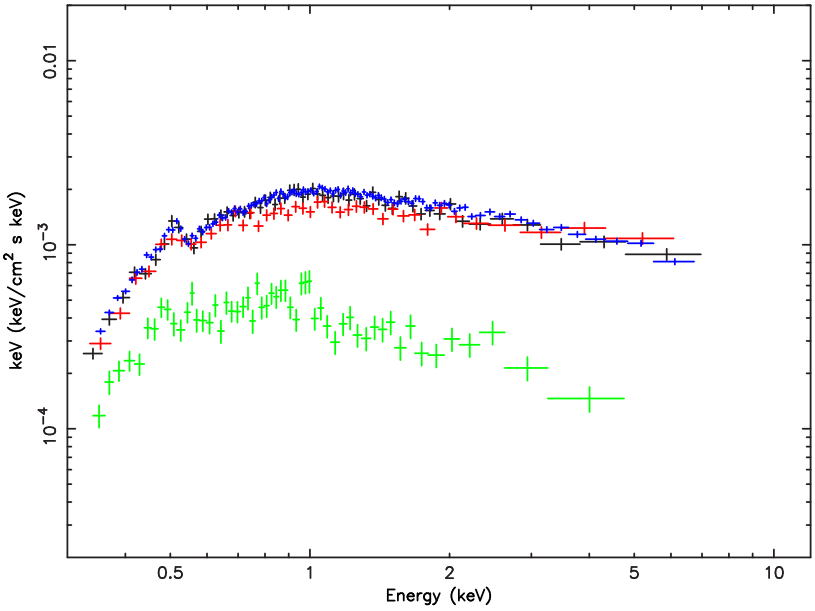

Figure 5.25: The unfolded spectra of Holmberg II X-1. The black, red, green and blue spectra are from the PN data of the *XMM–Newton* 2002-04-10, 2002-04-16, 2002-09-18, and 2004-04-15 observations, respectively.

Table 5.5: Summary of model fits to the *XMM–Newton* spectra of Holmberg II X-1. [a,b]

	Model	$N_{\rm H}$ (10^{22} cm^{-2})	Parameters	$F_{\rm X}$ [c]	$L_{\rm X}$ [c]	χ^2/ν
			XMM–Newton			
2002-04-10	PL	$0.17^{+0.01}_{-0.01}$	$\Gamma = 2.68^{+0.04}_{-0.04}$	6.2	9.9	233.3/180
	MCD [d]		$T_{\rm in} = 0.66$	5.1	8.2	1124.5/180
	MCD	$0.15^{+0.03}_{-0.02}$	$T_{\rm in} = 0.29^{+0.06}_{-0.09}$	0.58	0.93	217.6/178
	+ PL		$\Gamma = 2.49^{+0.12}_{-0.14}$	5.7	9.1	
	MCD	$0.09^{+0.03}_{-0.03}$	$T_{\rm in} = 0.31^{+0.04}_{-0.03}$	1.5	2.4	206.4/177
	+ cutoff-PL		$\Gamma = 1.62^{+0.47}_{-0.65}$ / $E_{\rm cut} = 4.4^{+4.7}_{-1.8}$	4.7	7.5	
2002-04-16	PL	$0.13^{+0.01}_{-0.01}$	$\Gamma = 2.44^{+0.05}_{-0.04}$	5.9	9.4	191.7/132
	MCD [d]		$T_{\rm in} = 0.67$	4.6	7.4	995.0/132
	MCD	$0.12^{+0.02}_{-0.02}$	$T_{\rm in} = 0.24^{+0.03}_{-0.04}$	0.79	1.3	138.5/130
	+ PL		$\Gamma = 2.14^{+0.11}_{-0.10}$	5.4	8.6	
	MCD	$0.09^{+0.03}_{-0.03}$	$T_{\rm in} = 0.26^{+0.05}_{-0.03}$	1.3	2.1	134.3/129
	+ cutoff-PL		$\Gamma = 1.51^{+0.50}_{-1.19}$ / $E_{\rm cut} = 5.4^{+21.2}_{-3.3}$	4.7	7.5	
2002-09-18	PL	$0.14^{+0.02}_{-0.02}$	$\Gamma = 3.03^{+0.11}_{-0.10}$	1.2	1.9	167.1/133
	MCD [d]		$T_{\rm in} = 0.44$	1.0	1.6	344.7/133
	MCD	$0.13^{+0.04}_{-0.03}$	$T_{\rm in} = 0.19^{+0.04}_{-0.06}$	0.18	0.29	156.4/131
	+ PL		$\Gamma = 2.76^{+0.20}_{-0.18}$	1.1	1.8	
2004-04-15	PL [d]	0.17	$\Gamma = 2.68$	6.4	10	691.1/311
	MCD [d]		$T_{\rm in} = 0.64$	5.3	8.5	7207.8/311
	MCD	$0.15^{+0.01}_{-0.01}$	$T_{\rm in} = 0.26^{+0.02}_{-0.02}$	0.69	1.1	484.2/309
	+ PL		$\Gamma = 2.46^{+0.04}_{-0.04}$	5.8	9.3	
	MCD	$0.08^{+0.01}_{-0.01}$	$T_{\rm in} = 0.29^{+0.01}_{-0.01}$	1.7	2.7	387.3/308
	+ cutoff-PL		$\Gamma = 1.36^{+0.24}_{-0.13}$ / $E_{\rm cut} = 3.4^{+0.9}_{-0.6}$	4.6	7.4	

[a] All quoted errors are 90% confidence regions.

[b] The temperatures of parameters are in the units of keV.

[c] The 0.5–10 keV absorption uncorrected flux in 10^{-12} erg s^{-1}cm^{-2} and luminosity in 10^{39} erg s^{-1} .

[d] Since the fit is significantly rejected, there is no confidence error.

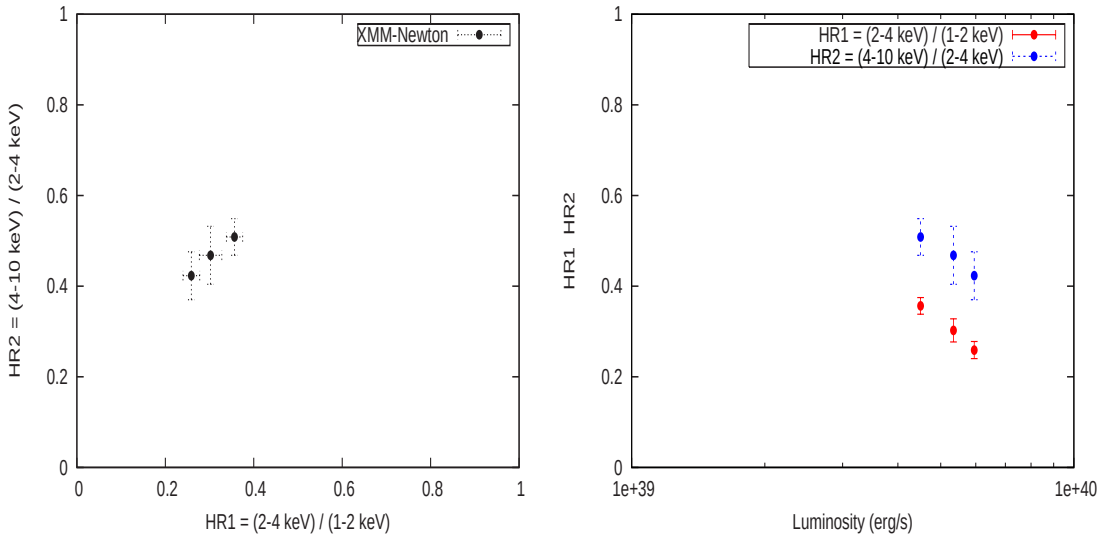

Figure 5.26: The CCP (left) and LCP (right) of NGC5204 X-1, acquired in the *XMM–Newton* observations.

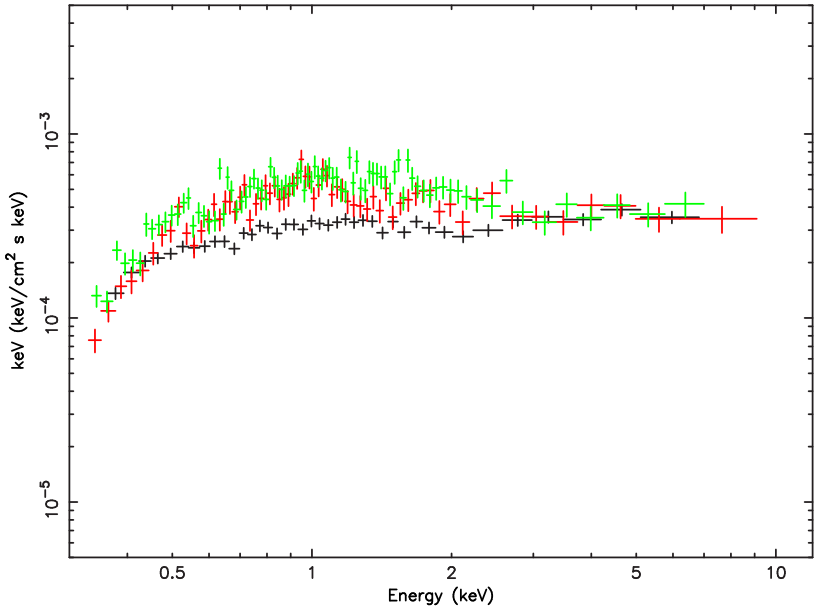

Figure 5.27: The unfolded spectra of NGC5204 X-1. The black, red, and green spectra are from the PN data of the *XMM–Newton* 2003-01-06, 2003-04-25, and 2003-05-01 observations, respectively.

Table 5.6: Summary of model fits to the *XMM–Newton* spectra of NGC5204 X-1. [a,b]

	Model	$N_{\rm H}$ (10^{22} cm^{-2})	Parameters	$F_{\rm X}$ [c]	$L_{\rm X}$ [c]	χ^2/ν
			XMM–Newton			
2003-01-06	PL	$0.05^{+0.01}_{-0.01}$	$\Gamma = 2.03^{+0.05}_{-0.05}$	1.5	4.2	131.1/85
	MCD [d]		$T_{\rm in} = 0.73$	1.1	3.1	972.2/85
	MCD	$0.05^{+0.02}_{-0.02}$	$T_{\rm in} = 0.28^{+0.05}_{-0.05}$	0.19	0.53	93.1/83
	+ PL		$\Gamma = 1.73^{+0.11}_{-0.13}$	1.4	3.9	
2003-04-25	PL	$0.10^{+0.01}_{-0.01}$	$\Gamma = 2.35^{+0.07}_{-0.07}$	1.8	5.0	145.5/128
	MCD [d]		$T_{\rm in} = 0.66$	1.4	3.9	514.6/128
	MCD	$0.12^{+0.02}_{-0.03}$	$T_{\rm in} = 0.21^{+0.05}_{-0.03}$	0.26	0.73	113.5/126
	+ PL		$\Gamma = 2.10^{+0.11}_{-0.13}$	1.7	4.8	
2003-05-01	PL	$0.12^{+0.01}_{-0.01}$	$\Gamma = 2.44^{+0.07}_{-0.06}$	2.1	5.9	178.3/158
	MCD [d]		$T_{\rm in} = 0.65$	1.6	4.5	529.8/158
	MCD	$0.09^{+0.03}_{-0.04}$	$T_{\rm in} = 0.31^{+0.07}_{-0.08}$	0.28	0.78	167.5/156
	+ PL		$\Gamma = 2.15^{+0.17}_{-0.30}$	1.8	5.0	

[a] All quoted errors are 90% confidence regions.

[b] The temperatures of parameters are in the units of keV.

[c] The 0.5–10 keV absorption uncorrected flux in 10^{-12} erg s^{-1}cm^{-2} and luminosity in 10^{39} erg s^{-1} .

[d] Since the fit is significantly rejected, there is no confidence error.

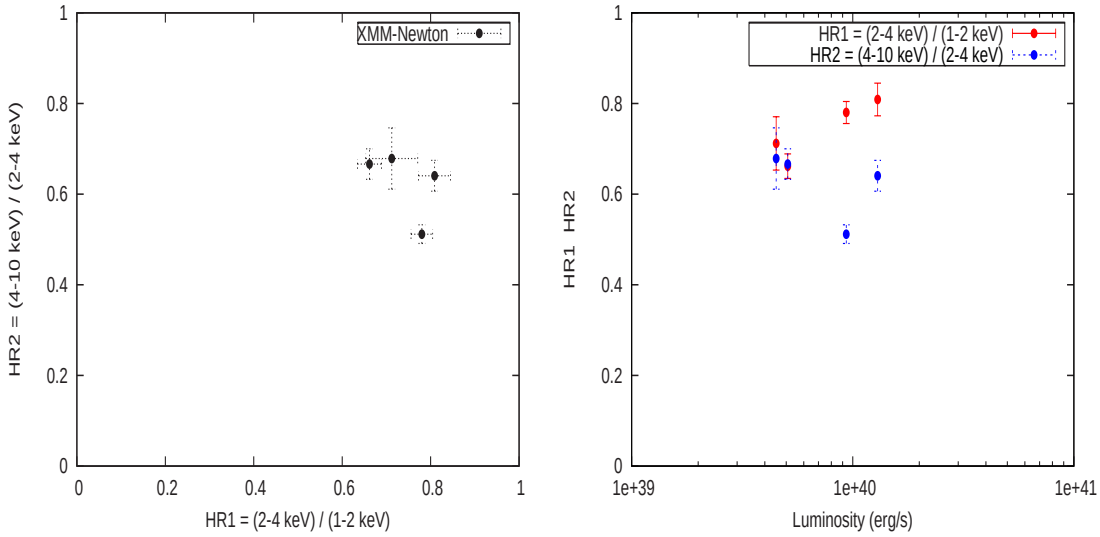

Figure 5.28: The CCP (left) and LCP (right) of IC342 X-1, acquired in the *XMM–Newton* observations.

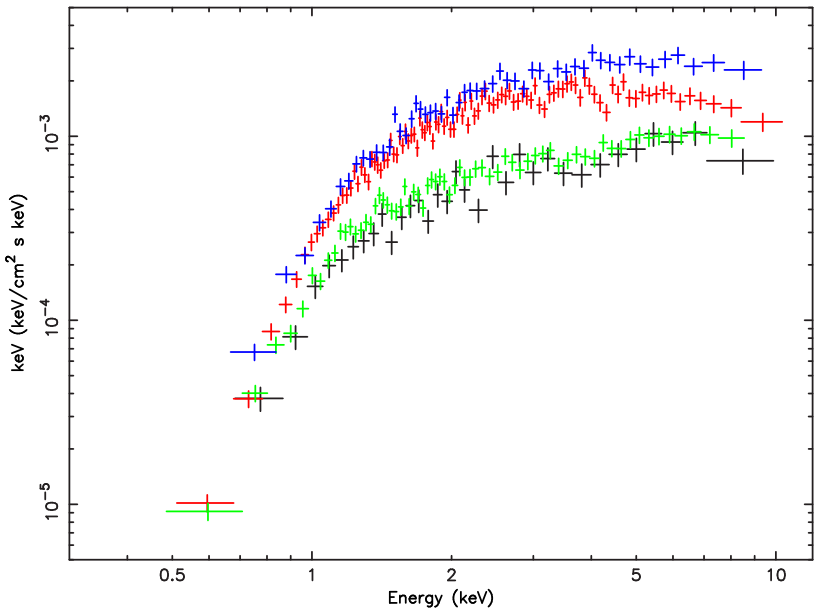

Figure 5.29: The unfolded spectra of IC342 Source 1. The black, red, green and blue spectra are from the PN data of the *XMM–Newton* 2001-02-11, 2004-02-20, 2004-08-17, and 2005-02-10 observations, respectively.

Table 5.7: Summary of model fits to the *XMM–Newton* spectra of IC342 Source 1. [a,b]

	Model	$N_{\rm H}$ (10^{22} cm^{-2})	Parameters	$F_{\rm X}$ [c]	$L_{\rm X}$ [c]	χ^2/ν
			XMM–Newton			
2001-02-11	PL	$0.56^{+0.07}_{-0.06}$	$\Gamma = 1.64^{+0.09}_{-0.08}$	2.4	4.6	69.1/70
	MCD	$0.28^{+0.04}_{-0.04}$	$T_{\rm in} = 2.09^{+0.17}_{-0.14}$	2.2	4.2	99.4/70
2004-02-20	PL	$0.83^{+0.03}_{-0.02}$	$\Gamma = 2.02^{+0.03}_{-0.03}$	5.1	9.7	244.6/232
	MCD	$0.47^{+0.02}_{-0.01}$	$T_{\rm in} = 1.58^{+0.04}_{-0.03}$	4.7	8.9	409.3/232
	variable-p	$0.74^{+0.03}_{-0.02}$	$T_{\rm in} = 2.78^{+0.53}_{-0.22}$ / $p = 0.53^{+0.01}_{-0.01}$	4.9	9.3	203.0/231
	cutoff-PL	$0.71^{+0.04}_{-0.04}$	$\Gamma = 1.47^{+0.14}_{-0.14}$ / $E_{\rm cut} = 6.9^{+2.5}_{-1.5}$	5.0	9.5	203.8/231
2004-08-17	PL	$0.60^{+0.03}_{-0.03}$	$\Gamma = 1.78^{+0.05}_{-0.05}$	2.7	5.1	129.3/116
	MCD [d]	0.34	$T_{\rm in} = 1.76$	2.4	4.6	347.3/116
2005-02-10	PL	$0.83^{+0.04}_{-0.04}$	$\Gamma = 1.83^{+0.05}_{-0.05}$	7.2	14	143.4/127
	MCD	$0.46^{+0.03}_{-0.02}$	$T_{\rm in} = 1.82^{+0.06}_{-0.06}$	6.6	13	164.0/127
	variable-p	$0.68^{+0.07}_{-0.05}$	$T_{\rm in} = 2.66^{+0.62}_{-0.26}$ / $p = 0.58^{+0.02}_{-0.03}$	6.8	13	114.3/126
	cutoff-PL	$0.65^{+0.06}_{-0.06}$	$\Gamma = 1.15^{+0.21}_{-0.22}$ / $E_{\rm cut} = 5.6^{+2.5}_{-1.4}$	6.9	13	114.0/126

[a] All quoted errors are 90% confidence regions.

[b] The temperatures of parameters are in the units of keV.

[c] The 0.5–10 keV absorption uncorrected flux in 10^{-12} erg s^{-1}cm^{-2} and luminosity in 10^{39} erg s^{-1} .

[d] Since the fit is significantly rejected, there is no confidence error.

Chapter 6

SPECTRAL STUDIES OF M82 X-1

In this Chapter, we study the most luminous ULX, M82 X-1, as the final target. As mentioned in §§4.1.1, we utilize the *Chandra* and *Suzaku* observations. This object provides a rare chance to utilize the information above 10 keV obtained with the *Suzaku* HXD.

6.1 *Chandra* Results

As explained in §§4.1.1, this source is surrounded by strong thermal X-ray emission, as well as several luminous compact sources. Accordingly, we first evaluate the archival spectrum taken with *Chandra* , because it is considered to be least contaminant by surrounding X-ray sources thanks to its high spatial resolution.

We analyzed the $\sim$ 60 ks data set obtained on 2005-02-04, with the ACIS-S instrument onboard *Chandra* ; the ACIS is a CCD-based instrument capable of imaging spectroscopy, like the *XMM–Newton* EPIC and the *Suzaku* XIS. This data set was already analyzed by Kaaret et al. (2006). Although this galaxy has been observed with *Chandra* several times, the X-1 spectra obtained in the other observations severely suffered from a pile-up effect (Davis 2001), so that we utilize only the 2005-02-04 data set. We screened the ACIS-S data with a standard manner using CIAO (*Chandra* Interactive Analysis of Observations) software package version 3.4.

On this occasion, the source exhibited a 0.5–10 keV luminosity of $\sim 3 \times 10^{40}$ erg s^{-1} , which is typical of, or relatively lower than, the previous measurements which scatter over $\sim$ 2–10 $\times 10^{40}$ erg s^{-1} (e.g. Griffiths et al. 1979; Watson et al. 1984; Fabbiano 1988; Schaaf et al. 1989; Tsuru 1992; Tsuru et al. 1997; Matsumoto et al. 1999; Ptak et al.

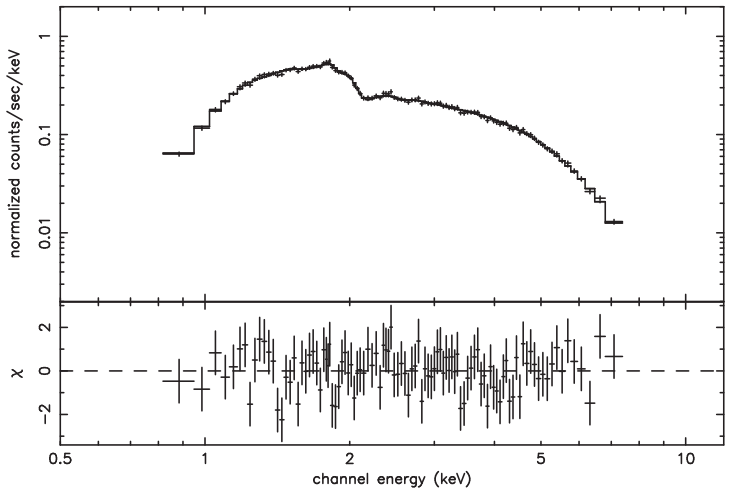

Figure 6.1: A background-subtracted spectrum of M82 X-1 obtained with the *Chandra* ACIS-S CCD, presented together with the best-fit absorbed PL model.

1999; Cappi et al. 1999; Matsumoto et al. 2001; Kaaret et al. 2001; Rephaeli & Gruber 2002; Strohmayer & Mushotzky 2003; Kaaret et al. 2006; Dewangan et al. 2006).

Figure 6.1 shows a background-subtracted ACIS-S spectrum of M82 X-1. Similar to the other ULXs spectra described in the previous Chapter, the spectrum in the 0.8–7 keV energy range is featureless. An absorbed PL model gave an acceptable ($\chi^2/\nu = 84.5/101$ with a probability of 88%) fit, with $\Gamma \sim 1.6$ and $N_{\rm H} \sim 1.1 \times 10^{22}$ cm^{-2}. In contrast, the MCD fit was found to be unacceptable ($\chi^2/\nu = 333.1/101$). The spectral parameters are summarized in table 6.1. This result agrees with that by Kaaret et al. (2006), and indicates that this source was in the PL-type state on this occasion. This is consistent with the results of Chapter 5 that the PL-type spectra are observed in many ULXs in their dimmer state, because M82 X-1 was relatively dim on this occasion as compared to its highest recorded luminosity ($\sim 1 \times 10^{41}$ erg s^{-1}).

Table 6.1: Summary of model fits to the *Chandra* and *Suzaku* spectra of M82 X-1. [a,b]

	Model	$N_{\rm H}$ (10^{22} cm^{-2})	Parameters	$F_{\rm X}$ [c]	$L_{\rm X}$ [c]	χ^2/ν
			Chandra 2005-02-04			
	PL	$1.12^{+0.03}_{-0.03}$	$\Gamma = 1.58^{+0.03}_{-0.03}$	15(17)	24(27)	84.5/101
	MCD [d]	0.80	$T_{\rm in} = 2.1$	13(15)	21(24)	333.1/101
			Suzaku 2005-10-(04,19,27)			
XIS-only	PL ($\leq$ 7 keV)	1.1(fixed)	$\Gamma = 1.53^{+0.04}_{-0.02}$	22	35	150.3/150
	PL	1.1(fixed)	$\Gamma = 1.67^{+0.02}_{-0.02}$	22	35	318.6/174
	cutoff-PL	1.1(fixed)	$\Gamma = 0.76^{+0.13}_{-0.15}$ / $E_{\rm cut} = 5.8^{+1.0}_{-0.8}$	21	34	183.7/173
XIS+PIN	PL	1.1(fixed)	$\Gamma = 1.75^{+0.02}_{-0.02}$	22	35	606.8/182
	cutoff-PL	1.1(fixed)	$\Gamma = 0.77^{+0.08}_{-0.15}$ / $E_{\rm cut} = 5.7^{+0.5}_{-0.7}$	21	34	193.6/181
(NXB +4%)	PL	1.1(fixed)	$\Gamma = 1.77^{+0.02}_{-0.02}$	22	35	809.1/182
	cutoff-PL	1.1(fixed)	$\Gamma = 0.55^{+0.08}_{-0.17}$ / $E_{\rm cut} = 4.7^{+0.4}_{-0.6}$	21	34	228.6/181
(NXB -4%)	PL	1.1(fixed)	$\Gamma = 1.73^{+0.02}_{-0.02}$	22	35	464.9/182
	cutoff-PL	1.1(fixed)	$\Gamma = 0.89^{+0.13}_{-0.10}$ / $E_{\rm cut} = 6.8^{+1.5}_{-0.8}$	21	34	202.1/181
[e]	PL	1.1(fixed)	$\Gamma = 1.64^{+0.03}_{-0.03}$	14	22	538.0/182
	cutoff-PL	1.1(fixed)	$\Gamma = 0.27^{+0.02}_{-0.04}$ / $E_{\rm cut} = 4.2^{+0.1}_{-0.1}$	14	22	193.2/181
[f]	PL	1.1(fixed)	$\Gamma = 1.71^{+0.04}_{-0.04}$	8.5	14	303.9/182
	cutoff-PL	1.1(fixed)	$\Gamma = 0.17^{+0.06}_{-0.04}$ / $E_{\rm cut} = 3.7^{+0.1}_{-0.1}$	8.0	13	193.1/181

[a] All quoted errors are 90% confidence regions.

[b] The temperatures of parameters are in the units of keV.

[c] The 2–10 keV absorption uncorrected flux in 10^{-12} erg s^{-1}cm^{-2} and luminosity in 10^{39} erg s^{-1}, where for the *Chandra* data the 0.5–10 keV flux and luminosity are also shown in parentheses.

[d] Since the fit is significantly rejected, there is no confidence error.

[e] The case when spectra of fainter sources except for X-1 and X-2 were removed.

[f] The case when spectra of both fainter sources and X-2 were removed.

6.2 *Suzaku* Results

6.2.1 XIS spectra

After analyzing the *Chandra* data, we next study the *Suzaku* data of M82 X-1. As shown in table 4.3, M82 was observed with *Suzaku* three times on October 2005. Figure 6.2 shows background-subtracted 3.2–10 keV XIS spectra, which are summed over the three observations because the signal counts are not much different. Here, we did not utilize the energy range below 3.2 keV, because of the contamination from the bright thermal X-ray emission around the galaxy that cannot be excluded in the *Suzaku* spectra because of the poorer angular resolution. In the 3.2–10 keV range, we thus observe a rather hard continuum, together with emission line structures at 6–7 keV; the latter must be iron lines, as reported in previous observations (e.g. Tsuru et al. 1997; Matsumoto et al. 1999; Cappi et al. 1999; Rephaeli & Gruber 2002; Strohmayer & Mushotzky 2003; Agrawal & Misra 2006; Strickland & Heckman 2007). The *Chandra* spectrum of figure 6.1 has such poor quality above $\sim$ 6 keV that the presence of similar Fe lines would not be excluded.

The 2–10 keV source luminosity in the *Suzaku* observations was obtained on average as $\sim 3.5 \times 10^{40}$ erg s^{-1} , which is comparable to that measured by *Chandra* in the previous section. In order to compare the *Suzaku* spectra with that of *Chandra* , we first fitted the XIS spectra with a PL model in the limited 3.2–7 keV range, adding two Gaussians for the Fe-K$_\alpha$ lines in the 6–7 keV band. The hydrogen column density describing photoelectric absorption was fixed at 1.1×10^{22} cm^{-2}, as determined with *Chandra* in the previous section. The fit was acceptable with $\chi^2/\nu = 150.3/150$ and the continuum slope was obtained as $\Gamma \sim 1.5$. As summarized in table 6.1, one Gaussian was obtained at a center energy of 6.67 ± 0.02 keV, with an intrinsic width (in Gaussian sigma) of < 0.11 keV, and an equivalent width (EW) of $\sim$ 60 eV; it improved the fit by $\Delta\chi^2 \sim 120$. The other Gaussian, with its energy fixed at 6.4 keV and assumed to be narrow, improved the fit by $\Delta\chi^2 \sim 20$. Its EW was obtained as $\sim$19 eV. Since the value of Γ agrees with that determined by the *Chandra* data, the *Suzaku* spectra are confirmed to be rather free from the contamination by surrounding diffuse and discrete X-ray sources.

We next re-fitted the XIS spectra with the same PL model, using the energy range up to 10 keV. As shown in figure 6.2 (left), the fit became unacceptable with $\chi^2/\nu = 318.6/174$,

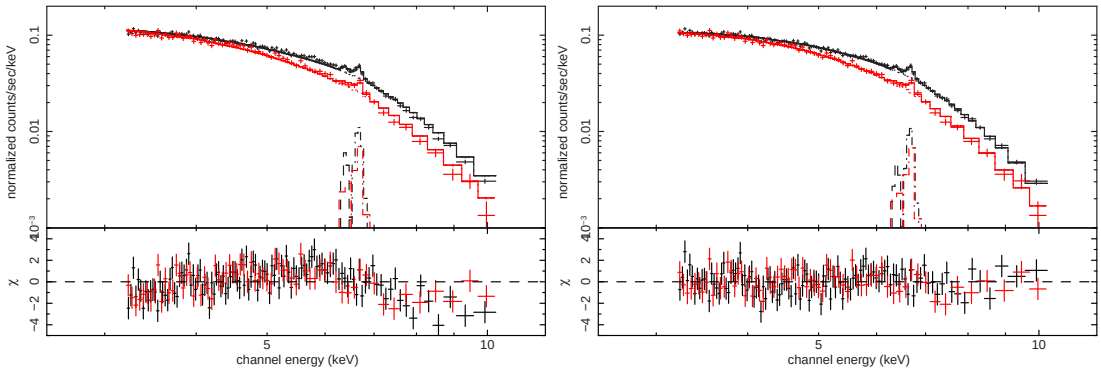

Figure 6.2: Background-subtracted XIS spectra of M82 X-1, presented together with the best-fit absorbed PL (left) and cutoff PL (right) model. In both fits, two gaussians are included. The FI and BI CCD data are shown in black and red, respectively.

contrary to the fitting results in the $\leq$ 7 keV range. This is because the model now overpredicts the data above $\sim$ 7 keV. In other words, the spectra are more convex than a single power-law. Therefore, we fitted them by a cutoff PL model. As described in figure 6.2 (right), the fit then became acceptable with $\chi^2/\nu = 183.7/173$ (with a probability of 27.4%), yielding $\Gamma = 0.76^{+0.13}_{-0.15}$ and a cutoff energy of $5.8^{+1.0}_{-0.8}$ keV, as summarized in table 6.1. Using an F-test, the fit improvement was significant with >99%.

6.2.2 HXD-PIN analysis

Adding to the XIS spectra, we analyze the *Suzaku* HXD-PIN data, in order to investigate the spectrum of M82 X-1 over a wider energy range incorporating the data above 10 keV.

Similar to the XIS data reduction described in §§4.2.2, the HXD-PIN data sets were screened by the revision 1.2 pipeline processing using the standard criteria as follows. We required that the time after passage through the SAA should be longer than 1000 seconds, that the data should be taken in regions where COR is higher than 8 GeV/c, and that the source elevation angle should be higher than 5° above the Earth rim. Futhermore, light curves and spectra were corrected for instrumental dead times. After these screenings, the three observations gave effective exposure of 24 ks, 31 ks, and 22 ks, on 2005 October 4, 19, and 27, respectively.

To perform background subtraction which is crucial for the HXD analysis, we utilized non X-ray background (NXB) models provided by the HXD detector team (Kokubun et

al. 2007). Currently, there are two NXB models available, so-called *bgd_A* and *bgd_B*, which employ both Monte-Carlo techniques but with different algorithms (Mizuno et al. 2006; Watanabe et al. 2007). We produced fake background events using the two NXB models, both under the same observing conditions as the actual data taking, and utilizing the observed auxiliary information such as upper-discriminator hit rates. By processing the fake events through the same screening criteria as for the actual on-source data, we derived two NXB spectra for each observation. Then, *bgd_A* and *bgd_B* respectively gave 12–70 keV count rates of 0.46 and 0.45 cts s^{-1} on October 4, 0.49 and 0.48 cts s^{-1} on October 19, and 0.52 and 0.50 cts s^{-1} on October 27. Thus, the two NXB models are consistent within 4%. Hereafter, we employ *bgd_A* for our spectral analysis.

In order to evaluate the NXB subtraction accuracy, we extracted Earth-occulted data from the three observations, which are thought to consist purely of the NXB events, and examined if the spectra during these epochs can be reprodued by the NXB model. Specifically, we screened the occultation data with the same criteria as for the on-source data, except that the Earth elevation angle was constrained to $< -5^\circ$ instead of $> 5^\circ$. The obtained exposure was 5.3 ks on October 19 and 1.3 ks on October 27, while the October 4 data were free from Earth occultations. Figure 6.3 compares the observed Earth-occultation data, with the synthetic *bgd_A* spectra which emulate the NXB to be observed during these Earth-occultation periods. The observed and modeled NXB count rates in the 12–70 keV energy range are 0.56 ± 0.02 and 0.55 cts s^{-1} respectively on October 19, and 0.54 ± 0.04 and 0.54 cts s^{-1} on October 27 likewise, where the errors refer to statistical 90% confidence level. Statistical errors associated with the NXB model are neglected, because the model is designed to produce 10 times larger number of fake events than those actually expected. Thus, the observed and modeled NXB spectra agree with each other within the statistic errors. Furthermore, the spectral shape is fully consistent between them.

When we limit energy band of the Earth-occultation data to 12–20 keV, where signals are possibly detected as described in the next paragraph, the observed and modeled NXB count rates become 0.31 ± 0.01 and 0.31 cts s^{-1} respectively on October 19, and 0.30 ± 0.03 and 0.30 cts s^{-1} on October 27 likewise. Accordingly, the observed and modeled NXB spectra agree each other within statistic errors of 4% and 10%, on October 19 and 27, respectively. When the two data sets are combined, the NXB model reproduces the

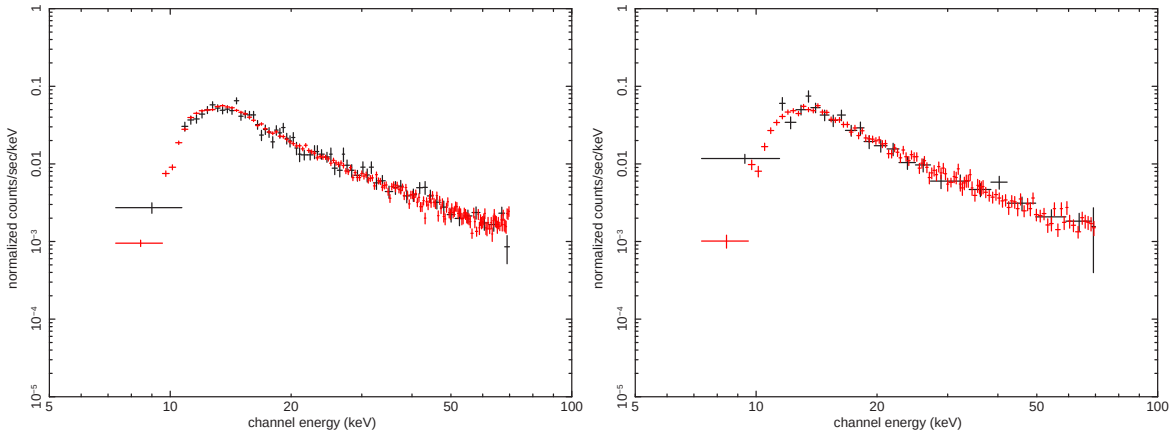

Figure 6.3: Earth-occultation spectra of HXD-PIN (black) obtained on October 19 (left) and 27 (right), compared with the modeled non X-ray background (red).

Earth-occultation data to within ±4%. Therefore, we hereafter consider that the NXB model correctly reproduces the HXD-PIN NXB, within a systematic error of at most 4%. This agrees with the general systematic error of the NXB model, $\sim \pm 5\%$, as reported by Mizuno et al. (2006).

After these preparations, we actually derived the on-source HXD-PIN spectra of M82, and compared them in figure 6.4 with the corresponding NXB (*bgd_A*) models predictions. The figure also shows the NXB-subtracted data, and the predicted cosmic X-ray background (CXB) spectrum based on the *HEAO-1* results by Boldt (1987). Thus, after the NXB subtraction, positive signals remain up to $\sim$ 30 keV in the three observations. Furthermore, the signal count rate exceeds the expected CXB rate at least up to $\sim$ 20 keV. As detailed in table 6.2, the net signal rate, after subtracting both the CXB and NXB, becomes $\sim$ 0.023 cts s^{-1} when averaged over the three observations. This has a statistical significance of 4.7 $\sim$ 8.8 sigmas in individual observations, and $\geq$ 10 sigmas when averaged over the three of them.

While the positive PIN signals (in 12–20 keV) are statistically quite significant, is the detection survive systematic errors in the NXB estimation? As shown in table 6.2, the net signal count rate in 12–20 keV, $\sim$ 0.02 cts s^{-1}, is 6–10% of the NXB count rate in the same band. This exceeds the typical systematic error in the NXB modeling during the present observations, 4%, as estimated above using the Earth-occulated data. As a further confirmation, we compared the on-source count rate with those of the NXB and CXB, using a 30–70 keV range where the NXB is expected to dominate. Then, as given

Table 6.2: Signal and background count rates from HXD-PIN. [a]

	October 4	October 19	October 27	Average
12–20 keV				
on-source	0.295 ± 0.006	0.325 ± 0.005	0.343 ± 0.006	—
NXB [b]	0.260	0.280	0.300	—
CXB [c]	0.018	0.018	0.018	—
net signal‡	0.016 ± 0.006	0.027 ± 0.005	0.025 ± 0.006	0.023 ± 0.003
30–70 keV				
on-source	0.098 ± 0.003	0.104 ± 0.003	0.109 ± 0.003	—
NXB [b]	0.102	0.105	0.109	—
CXB [c]	0.002	0.002	0.002	—
net signal [d]	-0.007 ± 0.003	-0.003 ± 0.003	-0.002 ± 0.003	-0.004 ± 0.002

[a] All quoted errors correspond to 90% confidence level.

[b] Modeled with *bgd_A*.

[c] Predicted from the *HEAO-1* measurements (Boldt 1987).

[d] Net count rate, obtained by subtracting the NXB and CXB from the on-source rate.

in table 6.2, the net signal count rate (after subtracting the NXB and CXB) became -0.0037 cts s^{-1}, or -3.6% of the NXB, when averaged over the three data sets. Therefore, we are likely to be slightly over-subtracting the NXB, although within the uncertainty of the Earth-occulation study. Since this comparison in 30–70 keV tends to enhance the net signal intensity, we conclude that we have detected HXD-PIN signals from the M82 region, which remain significant even considering the systematic NXB uncertainty.

Because the XIS signal from the central region of M82 exhibited rather small variations during the present observations, we expect that the HXD-PIN signals are also rather constant, supposing that they are coming from the same region. If, on the other hand, the positive signals were an artifact of wrong NXB subtraction, we would expect them to vary with time (Kokubun et al. 2007). For this purpose, figure 6.5 shows the 12–20 keV PIN light curves of the three observations. The PIN light curves, with the NXB and CXB both removed, show constantly positive values through the three observations. By fitting

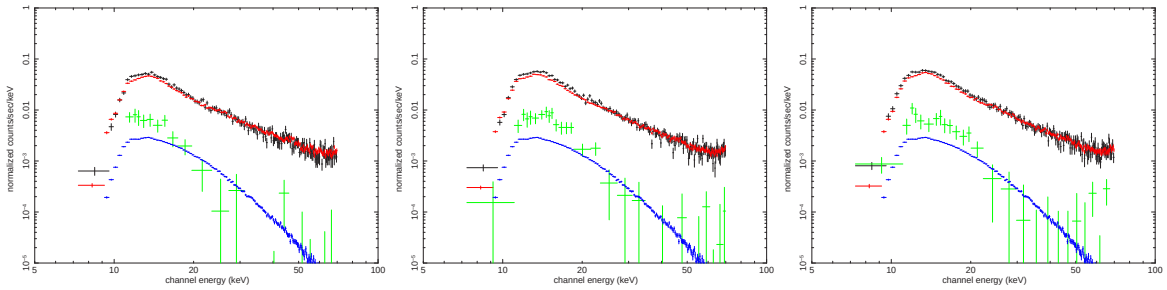

Figure 6.4: Time-averaged HXD-PIN spectra observed on October 4 (left), 19 (middle), and 27 (right). Each panel shows the observed spectrum (black), the modeled NXB spectrum (red), the signals remaining after subtracting the NXB (green), and the expected CXB spectrum (blue).

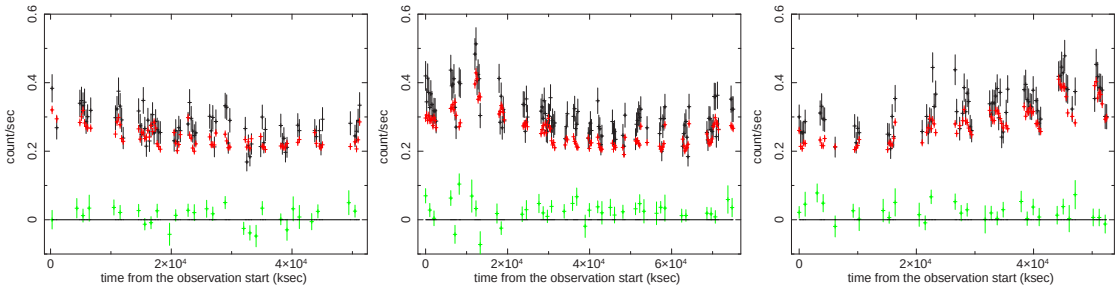

Figure 6.5: The 12–20 keV light curves of M82 observed with HXD-PIN on October 4 (left), 19 (middle), and 27 (right). Each panel shows the observed data (black), the modeled NXB data (red), and the signals remaining after subtracting the NXB and the expected CXB (green).

them with a constant, the source intensity was confirmed to agree with the values in table 6.2 derived from the spectra, and χ^2/d.o.f of the fit was obtained as 41.7/28, 42.8/39, and 31.2/30, in the first, second, and third observations, respectively. These correspond to the probability of the signal counts consistent with being constant of $\sim$ 5%, 35%, and 40%. Therefore, the variable NXB has been mostly subtracted successfully.

We analyzed the 12–20 keV PIN spectra, utilizing a standard response matrix file, and an auxiliary response file. From the observed PIN spectra, we subtracted both the modeled NXB and the expected CXB spectra. When the spectrum averaged over the three observations was fitted by a PL model, the photon index was obtained as $\Gamma = 3.4^{+1.0}_{-0.8}$, and the 12–20 keV flux as 4.4×10^{-12} erg s^{-1}cm^{-2} . If we consider the systematic errors discussed above, the obtained photon index and the 12–20 keV flux become $\Gamma = 3.7^{+3.1}_{-1.2}$

and 1.9×10^{-12} erg s^{-1}cm^{-2} (when the NXB 4% over-subtracted) respectively, while $\Gamma = 3.1^{+0.6}_{-0.6}$ and 6.7×10^{-12} erg s^{-1}cm^{-2} (when the NXB 4% under-subtracted).

6.2.3 Estimation of contribution from M81

As shown in figure 6.6, the M81 galaxy hosting a low-luminosity AGN, located $\sim 37'$ away from M82, was on the edge of the HXD-PIN FOV. Therefore, its contamination (though rather low) must be evaluated. According to a *BeppoSAX* observation, the M81 AGN exhibited a 10–100 keV flux of 7.4×10^{-11} erg s^{-1}cm^{-2} , and a PL spectrum with $\Gamma \sim 1.84$ (Pellegrini et al. 2000). These translate to a flux of 1.5×10^{-11} erg s^{-1} cm^{-2} in the 12–20 keV band. According to La Parola et al. (2004), the 0.5–2.4 keV intensity of the M81 nucleus varied by a factor of 4 through past observations, and at the maximum it was ~ 1.4 times as bright as observed with *BeppoSAX* by Pellegrini et al. (2000). On the other hand, the transmission efficiency of the PIN FOV for M81 was $\sim 3\%$, $\sim$1%, and $\sim 3\%$ in the three observations. Therefore, the maximum possible contamination of M81 to the PIN data, assuming 1.4 times the *BeppoSAX* flux, is estimated on these occasions to be 6×10^{-13}, 2×10^{-13}, and 6×10^{-13} erg s^{-1}cm^{-2} in the 12–20 keV band. These correspond to 20%, 4%, and 10% of the signale flux detected with HXD-PIN. Thus, we can conclude that most of the HXD-PIN signals are from M82, and hence the contamination from the M81 nucleus can be neglected.

6.2.4 Joint fits to the XIS and PIN spectra

So far, the XIS and HXD-PIN data were investigated individually in the previous subsections. Here we evaluate the XIS and PIN spectra simultaneously. As presented in figure 6.7, we utilized the XIS and PIN spectra both averaged over the three observations, because no large difference among them was seen as stated so far. In fitting the spectra, the absorption column was fixed to 1.1×10^{22} cm^{-2}, and the two Gaussian models were included, after the XIS spectral analysis. As before, we utilized the PIN spectra after subtracting the NXB and CXB, and also considered the case of systematically 4% over- and under-subtracted NXB.

Figure 6.7 (left) shows a simultaneous PL fit, with the model normalization constrained to be the same between the XIS and PIN. The fit was not acceptable with $\chi^2/\nu \geq 2$,

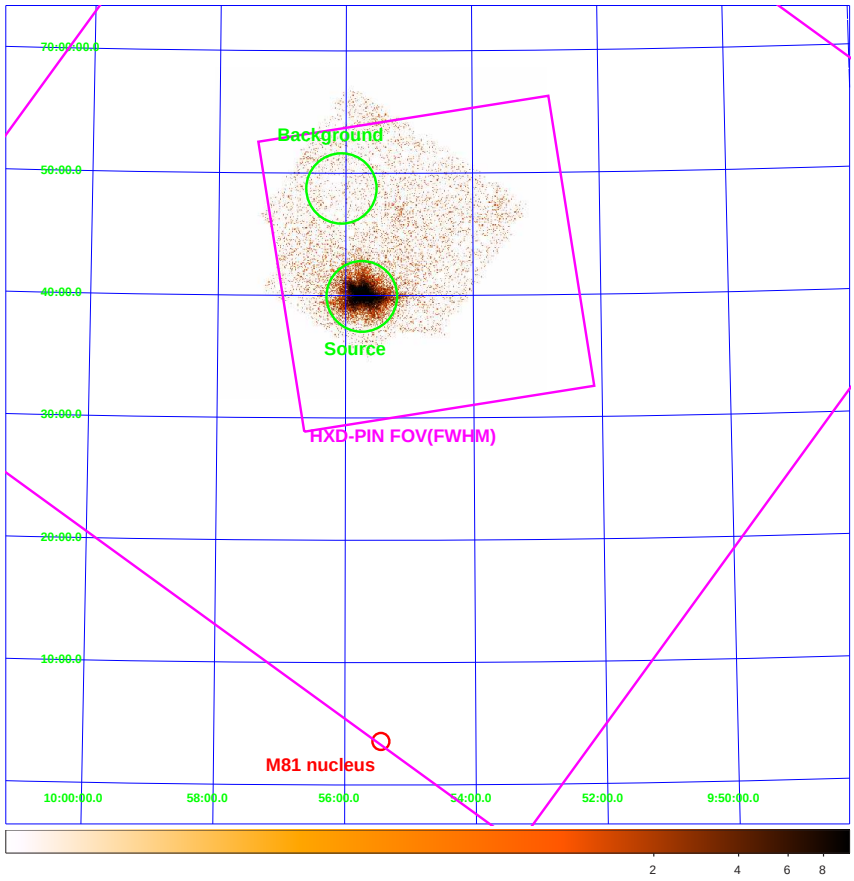

Figure 6.6: FOVs of HXD-PIN, overlaid on a background-inclusive 2–10 keV XIS0 image from the second observation. The smaller and larger squares in magenta show the FWHM and full-width at zero transmission FOVs of HXD-PIN, respectively. Green circles show the source and background regions for the XIS analysis. The location of the M81 nucleus is also shown as a red circle.

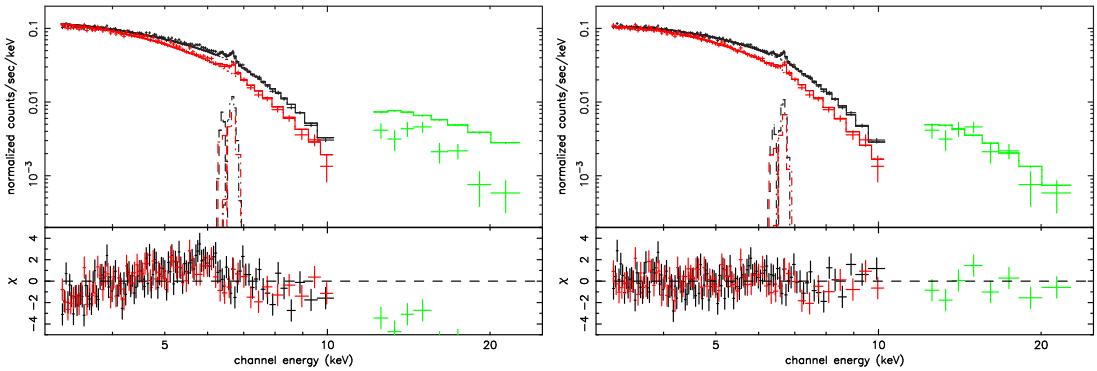

Figure 6.7: The same as figure 6.2, but including the HXD-PIN spectra (green) from which the NXB and CXB are both removed. Best-fit models are PL (left) and cutoff-PL (right).

because the model significantly over-predicted the data in the energy ranges of ≥ 7 keV. This result did not change even if the 4% NXB uncertainty is taken into account. Then, we allowed the model normalization to take separate values between the two instruments. Although the fits were improved to $\chi^2/\nu = 1.9$, the HXD vs. XIS normalization ratio became ≤ 0.7, which is too small even considering calibration uncertainties which is typically $\sim 10\%$ (Kokubun et al. 2007). Thus, the addition of the HXD-PIN data reinforce our inference obtained when using the XIS data only, that the X-1 spectrum is more convex than a PL (figure 6.2). Therefore, we employed a cutoff PL model, which already gave an acceptable fit to the XIS spectra. As shown in figure 6.7 (right) and table 6.1, the fit became again acceptable with $\chi^2/\nu = 1.1$–1.2, yielding a photon index $\Gamma = 0.5$–0.9 and a cutoff energy $E_{\rm cut} = 4$–8 keV. As seen in table 6.1, the best-fit cutoff-PL model thus determined jointly by the XIS and HXD is nearly identical to that determined by the XIS only.

6.2.5 Estimation of contribution from surrounding X-ray sources

Considering the relatively good agreement in the ≤ 7 keV spectra between *Suzaku* and *Chandra* , the *Suzaku* XIS spectra are considered to be dominated by the X-1 signal. However, as clarified with *Chandra* (Griffith et al. 2000; Matsumoto et al. 2001; Kaaret et al. 2006), M82 hosts in its central regions some dozen X-ray point sources with luminosities above $\sim 10^{38}$ erg s^{-1} . Since they are located in a region of $\sim 10''$ around X-1, they con-

tribute not only to our HXD-PIN spectrum, but also to the XIS signal extraction region. Therefore, we need to estimate to what extent these sources other than X-1 contaminates the *Suzaku* spectra, and how they affect our spectroscopic results on X-1.

The largest difficulty in the above estimation is possible time variations in the point X-ray sources (mostly accreting compact objects) around X-1. In order to chase their time variability and in particular to assess their brightest record, we re-visited the *Chandra* archival data. By 2007 August, six ACIS observations with > 10 ks exposure (ObsID:361, 1302, 2933, 6097, 5644, and 6361) were performed on the central region of M82. Using these data, we estimated fluxes and spectra of bright point sources, and of other overall X-ray components, which can potentially contaminate the *Suzaku* spectra.

As a result of analyzing these *Chandra* data, we found an object, located at $\sim 5''$ from X-1 (and hence cannot be resolved with *Suzaku*), that can potentially cause significant contamination. This object was previously noticed by Kaaret et al. (2006) under a designation of X42.3+59, and may be hereafter called "X-2". Through the six *Chandra* observations, X-2 varied largely with its 2–10 keV flux changing from $\lesssim 10^{-13}$ erg s^{-1}cm^{-2} to 6.9×10^{-12} erg s^{-1}cm^{-2} ; the latter amounts to about one third of our XIS detection. As already reported by Kaaret et al. (2006), the 3–8 keV X-2 spectrum at its maximum brightness is described by a rather hard PL with photon index $\Gamma \sim 1.2 - 1.3$, absorbed by $N_{\rm H} \sim 2 - 3 \times 10^{22}$ cm^{-2}. With the luminosity reaching $\sim 10^{40}$ erg s^{-1} , X-2 is also considered as a ULX exhibiting a PL-type spectrum.

Although there are about 10 fainter sources besides X-1 and X-2, their 2–10 keV luminosities on the 6 occasions were confirmed to be $< 3 \times 10^{39}$ erg s^{-1} each, or less than 10% of the *Suzaku* measurement. In addition, their summed 2–10 keV fluxes on these occasions were found to be relatively constant at $7 - 9 \times 10^{-12}$ erg s^{-1}cm^{-2} , and their summed spectrum was reproduced by a PL with $\Gamma = 1.5 - 1.7$. Given these, we decided to separate the contaminating sources into two categories, that is, X-2 as a single source, and the assembly of the other fainter sources. Below, we treat the latter contribution to the *Suzaku* XIS and PIN spectra as a fixed spectral component, while estimate the X-2 contribution under two extreme conditions.

As one of the two extremes, we first consider the case where X-2 is faint enough to be neglected. Then, we need only to consider the assembly of the fainter sources, of which the summed spectrum can be modeled in ≤ 8 keV by a single PL with $\Gamma \sim 1.6$

as described above. If this PL spectrum were assumed to extend to higher energies, HXD-PIN would have detected it up to 30 $\sim$ 40 keV as illustrated in figure 6.8 (top). However, the actual PIN spectrum is rather soft with $\Gamma \geq 2.5$, and detectable only in the 12–20 keV band. Therefore, the summed spectrum of these fainter sources must gradually bend. This inference is physically reasonable, because these sources are considered to be mainly luminous low-mass X-ray binaries, accreting pulsars, supernova remnants, and BH bineries, among which few would actually exhibit straight PL spectra extending to higher energies. Accordingly, we have decided to represent their summed spectrum employing a phenomenological thermal bremsstrahlung model, with its temperature fixed at $T = 10$ keV and its 2–10 keV flux set at 8×10^{-12} erg s^{-1}cm^{-2} . The temperature of 10 keV has been chosen so as to make the spectrum agree with the $\Gamma = 1.6$ PL in energies below 8 keV, and to conform to Makishima et al. (1989) who reported that the spatially integrated X-ray spectrum of M31 (dominated by similar discrete sources) can be approximated by a bremsstrahlung model with $T \sim 8$ keV. Including this additional spectrum as a fixed model component, we jointly re-fitted the *Suzaku* XIS and PIN spectra, in the same way as in the previous subsection. As shown in table 6.1, figure 6.8 (middle left), and figure 6.8 (middle right), the residual signals have been described successfully with a cutoff-PL model, but not by a PL model (with $\chi^2/\nu > 2$). This result agrees with that derived before neglecting the contamination, and yields the X-1 flux and luminosity which are about 2/3 of those derived before. The inferred X-1 spectrum has become somewhat more convex, with a flatter Γ and a lower value of $E_{\rm cut} \sim 4.2$ keV.

As the other extreme, we consider the case where X-2 shines at its highest brightness seen by the past *Chandra* observations. Then, we must also consider the contribution of X-2 to the *Suzaku* spectra. Although the X-2 spectra obtained by *Chandra* are rather hard ($\Gamma \sim$ 1.2–1.3), we cannot assume it to extend into the $>$ 10 keV energy range, for the same reasons as considered above for the fainter sources. Therefore, we assume the X-2 spectrum as an absorbed cutoff-PL model, with $N_{\rm H} = 2.5 \times 10^{22}$ cm^{-2}, $\Gamma = 0.5$, $E_{\rm cut} = 5$ keV, and the 2–7 keV flux of 4.5×10^{-12} erg s^{-1}cm^{-2} . This is a representative spectrum describing a PL-type ULX as derived in the previous Chapter, and its choice is motivated by our recognition that X-2 is a PL-type ULX. The model parameters have been selected so as to reproduce the *Chandra* results in the energy range below 8 keV. Including these two fixed model components, one for X-2 and the other for the fainter

sources, we repeated the analysis of the *Suzaku* spectra. As shown in table 6.1 and figure 6.8 (bottom left and bottom right), the obtained results are almost same as the case of X-2 being negligible, except that the 2–10 keV flux and luminosity reduced to $\sim 40\%$ of the original values without considering the contaminations.

From these results, we conclude that X-1 has a convex spectrum in the $3 \sim 20$ keV energy range, regardless of the behavior of the surrunding contaminant sources. The 2–10 keV luminosity of X-2 is estimated to be $\sim 2.2 \times 10^{40}$ erg s^{-1} if X-2 is dim enough, while $\sim 1.3 \times 10^{40}$ erg s^{-1} if X-2 is at its maximum luminosity ever recorded.

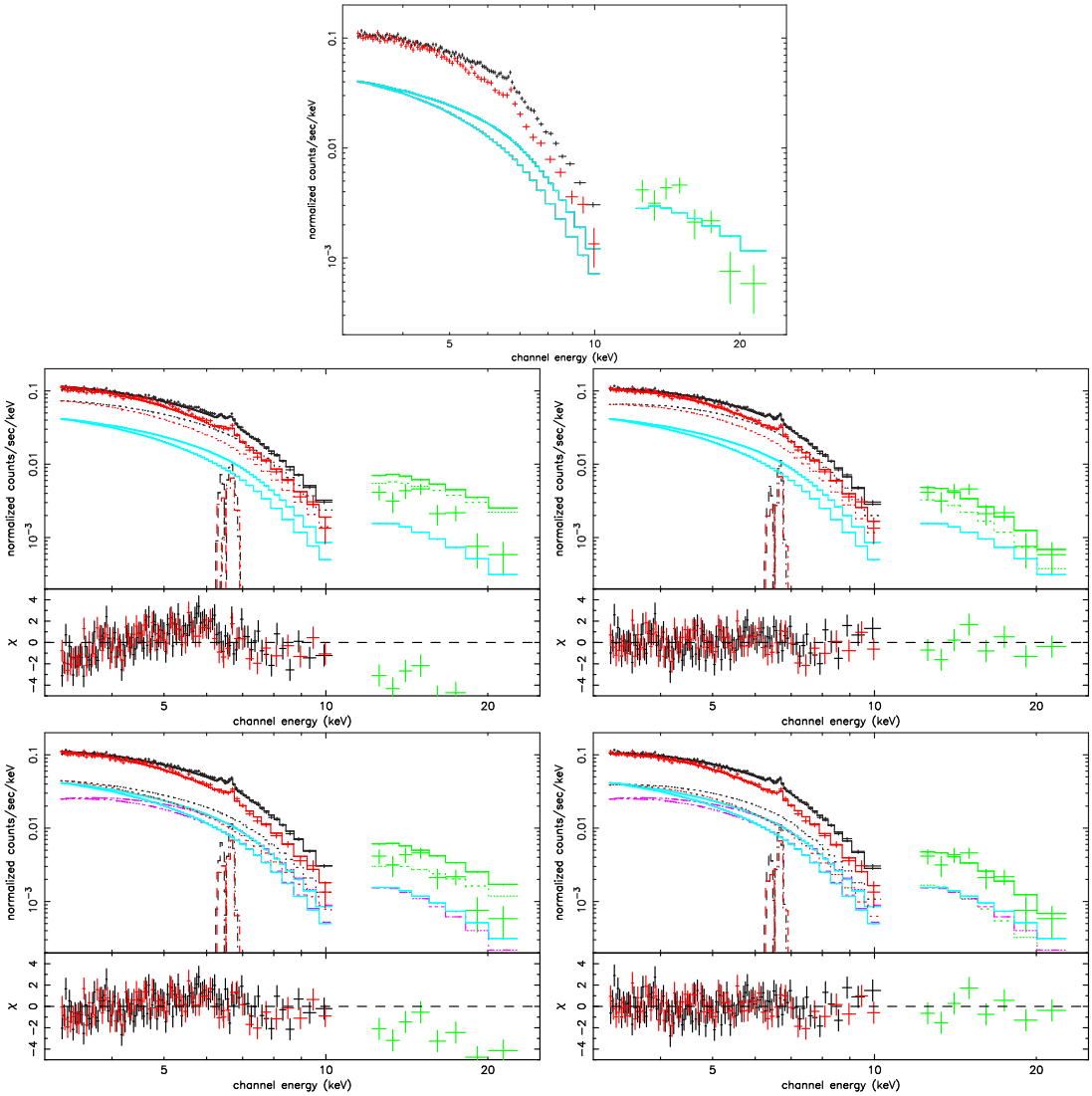

Figure 6.8: The same as figure 6.7, but considering the contribution from surrounding X-ray sources. The top panel shows the case when a PL spectrum of fainter sources (cyan) extends above 10 keV. The middle panels show the spectra fitted by the best-fit PL (left) or the cutoff-PL (right) model, where the modeled spectra of fainter sources (cyan) are included. The bottom panels show the spectra, where the modeled spectra of fainter sources (cyan) and X-2 (magenta) are included.

Chapter 7

DISCUSSION

7.1 Summary of the Results

Utilizing the multiple *Suzaku* and *XMM–Newton* observations, we investigated the spectra of typical 8 ULXs located in nearby (< 5 Mpc) galaxies. Although some of these data sets had already been analyzed by other authors, our unified and careful analyses have allowed us to to obtain significant new results on their luminosity-dependent spectral changes. In this Chapter, these results are combined into a unified picture of these ULXs.

In order to visualize and compare the overall spectral behavior of our sample ULXs, let us return to the CCP derived in Chapter 5. There, the CCPs utilized hardness ratios which are calculated from the observed raw (i.e., response-inclusive) count spectra. Here, to remove the effects of different detector responses and different values of $N_{\rm H}$ among observations, we re-calculated the hardness ratios from photon spectra which are "deconvolved", and also corrected for the photoelectric absorption by $N_{\rm H}$. The "deconvolution" means a process of approximately removing the effects of instrumental responses from the raw count spectra, utilizing the best-fit spectral models. The re-calculated CCPs become approximately independent of the instrument, and of the amount of intervening absorption. Figure 7.1 presents LCPs of all 8 targets, which have been re-calculated as described above. Here, the LCP of M82 X-1 refers to the *Chandra* results (§§6.1), because the *Suzaku* spectra of M82 X-1 (§§6.2) were restricted to the > 3 keV band.

Figure 7.2 is a composite CCP, where the 8 ULXs are plotted on a single panel; it is expected to play a key role in our discussion. We can clearly see in this CCP that the

spectra of all these ULXs change in a unified way as the luminosity changes. In particular, the data points can be roughly divided into two locations, one at (HR1, HR2) = (0.7, 0.6), and the other at (HR1, HR2) = (0.4, 0.4–0.6). The former and latter locations correspond to higher- and lower-luminosity data points of individual objects.

In a closer look, the locations of these data points on the CCP are seen to be divided into 5 representative regions, as specified in figure 7.2. Among them, Region 1 encompasses those data points obtained when an object is more luminous than it is in any other regions. So, let us denote the luminosity of each source in Region 1 as $L_{\rm c}$. Then, as summarized in table 7.1, their luminosities normalized to $L_{\rm c}$ are found to have a good correspondence to the five Regions. Although $L_{\rm c}$ can be directly defined only for 4 sources that evolve into Region 1, we can assume $L_{\rm c}$ of the other 4 sources as given in table 7.1, so that their normalized luminosities in other Regions behave in the same way as the former 4 sources. In other words, the 8 objects exhibit a rather common behavior on the CCP if their luminosity is normalized to the respective $L_{\rm c}$.

In order to relate locations on the CCP to the spectral models, we present in figure 7.3 the same CCP, on which grids of representative spectral parameters are superposed. From figure 7.3, we can see that the data points at (HR1, HR2) = (0.7, 0.6) corresponds to the spectra which can be represented by variable-p disk models with $T_{\rm in} \sim 2$ keV and $p \sim 0.6$, while those at (HR1, HR2) = (0.4, 0.4–0.6) to the spectra represepnted by PL models with $\Gamma \sim$ 2–2.5. These properties re-confirm (Sugiho 2003) that ULXs exhibit MCD-type spectra in their brighter phases and PL-type ones in their fainter phases. We can also see that the PL-type spectra become softer ($\Gamma = 1.5 \rightarrow 2.5$) as the luminosity increases, and that two sources (NGC1313 Source A and Holmberg II X-1) exhibit very soft ($\Gamma \sim 3$) spectra at their lowest luminosity, as already noticed in Chapter 5.

Using $L_{\rm c}$ defined above, and referring to the five Regions on the CCP, we can summarize the luminosity-dependent evolution of the ULX spectra as follows.

Region 1. At the highest luminosity of $\sim L_{\rm c}$, the data points are located on the CCP at (HR1, HR2) $\sim$ (0.7, 0.6). The spectra can be represented by a variable-p disk model with $T_{\rm in} \sim 2.5$ keV and $p \sim 0.6$.

Region 2. When the sources become dimmer ($\sim 0.6 L_{\rm c}$), the data points move down the CCP. The spectra become softer than those in Region 1, and exhibit more convex shapes,

Table 7.1: Luminosities of the 8 ULXs in the 5 Regions on the CCP, normalized to $L_{\rm c}$

Source	$L_{\rm c}$ (erg s^{-1})	Region 1	Region 2	Region 3	Region 4	Region 5
NGC1313 Source A	2×10^{40}	$1L_{\rm c}$ (1)[b]	–	0.4–0.5$L_{\rm c}$ (3)	0.2–0.3$L_{\rm c}$ (3)	0.15$L_{\rm c}$ (1)
NGC1313 Source B	7×10^{39}	0.9–1$L_{\rm c}$ (6)	0.5$L_{\rm c}$ (1)	0.2–0.3$L_{\rm c}$ (5)	–	–
M81 X-6	7×10^{39}	0.7–1$L_{\rm c}$ (3)	0.6$L_{\rm c}$ (2)	–	–	–
Holmberg IX X-1	(4×10^{40}) [a]	–	0.6$L_{\rm c}$ (1)	–	0.2–0.3$L_{\rm c}$ (3)	–
Holmberg II X-1	(4×10^{40}) [a]	–	–	0.4$L_{\rm c}$ (3)	–	0.05$L_{\rm c}$ (1)
NGC5204 X-1	(2×10^{40}) [a]	–	–	0.25–0.3$L_{\rm c}$ (2)	0.2$L_{\rm c}$ (1)	–
IC342 Source 1	1.3×10^{40}	$1L_{\rm c}$ (1)	–	–	0.4$L_{\rm c}$ (2)	–
M82 X-1	(1×10^{41}) [a]	–	–	–	0.3$L_{\rm c}$ (1)	–
average	–	$L_{\rm c}$	0.6$L_{\rm c}$	0.4$L_{\rm c}$	0.2 $L_{\rm c}$	0.1$L_{\rm c}$

[a] $L_{\rm c}$ is not directly measured, appropriately assumed.

[b] The number of observations is described in parenthesis.

so that a simple MCD model becomes a rather good approximation. In Region 1 and 2, the luminosity scales approximately as $\propto T_{\rm in}^2$ (figure 5.4 and figure 5.10).

Region 3. As the luminosity decrease to $\sim 0.4L_{\rm c}$, the data points make a jump, or "transition" to the left of the CCP. The spectra are no longer approximated by the MCD model, and instead, require a PL modeling with $\Gamma \sim 2.5$.

Region 4. When the luminosity further decreases to $\sim 0.2L_{\rm c}$, the spectra become gradually harder down to $\Gamma \sim 1.5$. The data points move to the top region of the CCP. In Regions 3 and 4, the spectra are often accompanied by a soft excess ($\simeq$ or MCD with $T_{\rm in} \sim 0.3$ keV) and a high-energy turn over.

Region 5. At the lowest luminosity of $\sim 0.1L_{\rm c}$, the spectra suddenly become softer, making another "transition" to the bottom left corner of the CCP. The spectra are approximated by a steep ($\Gamma \sim 3$) PL, with evidence for a cool MCD compontent.

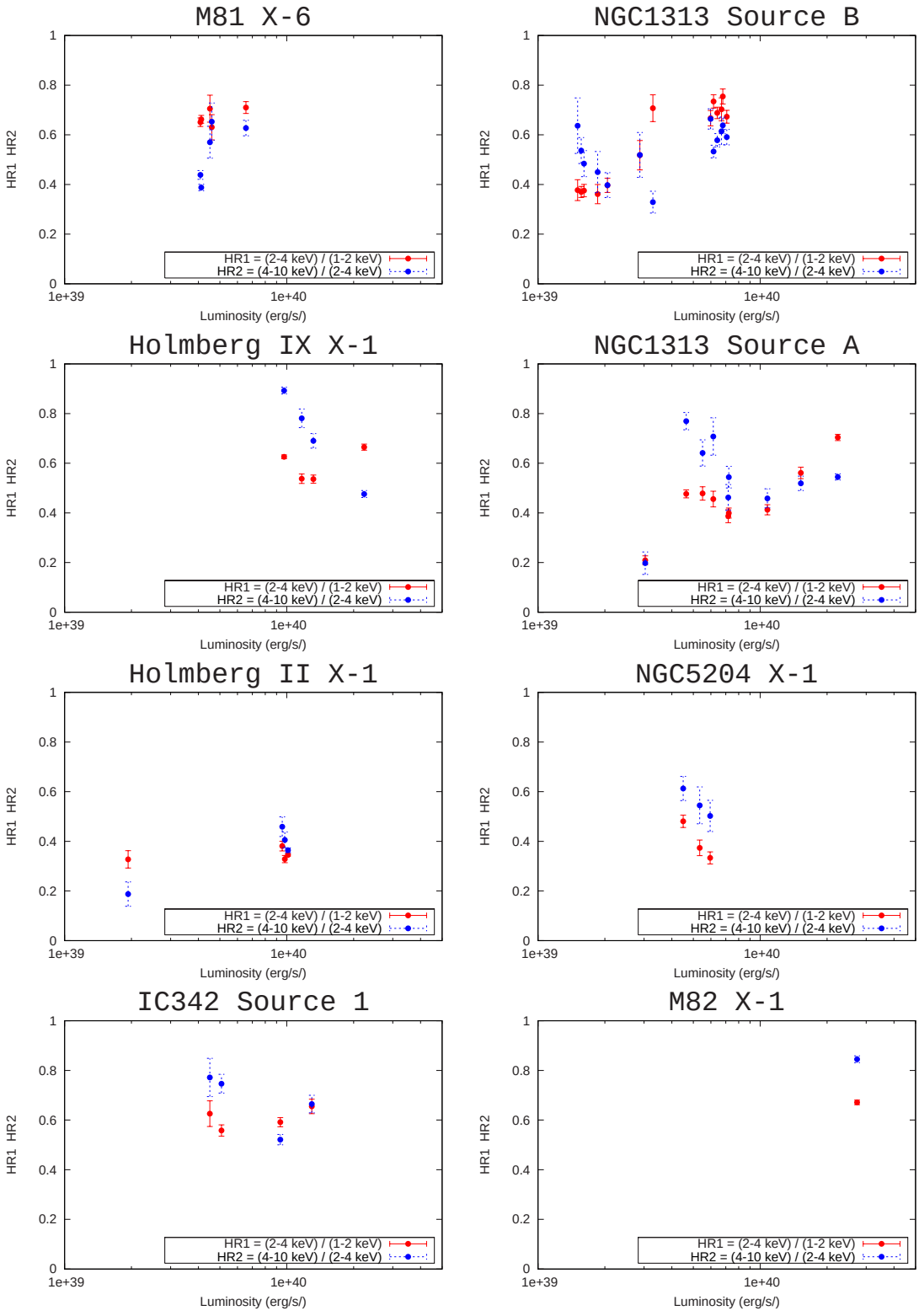

Figure 7.1: The LCPs of the indivicual ULXs, re-calculated using the de-convolved and absorption-corrected spectra.

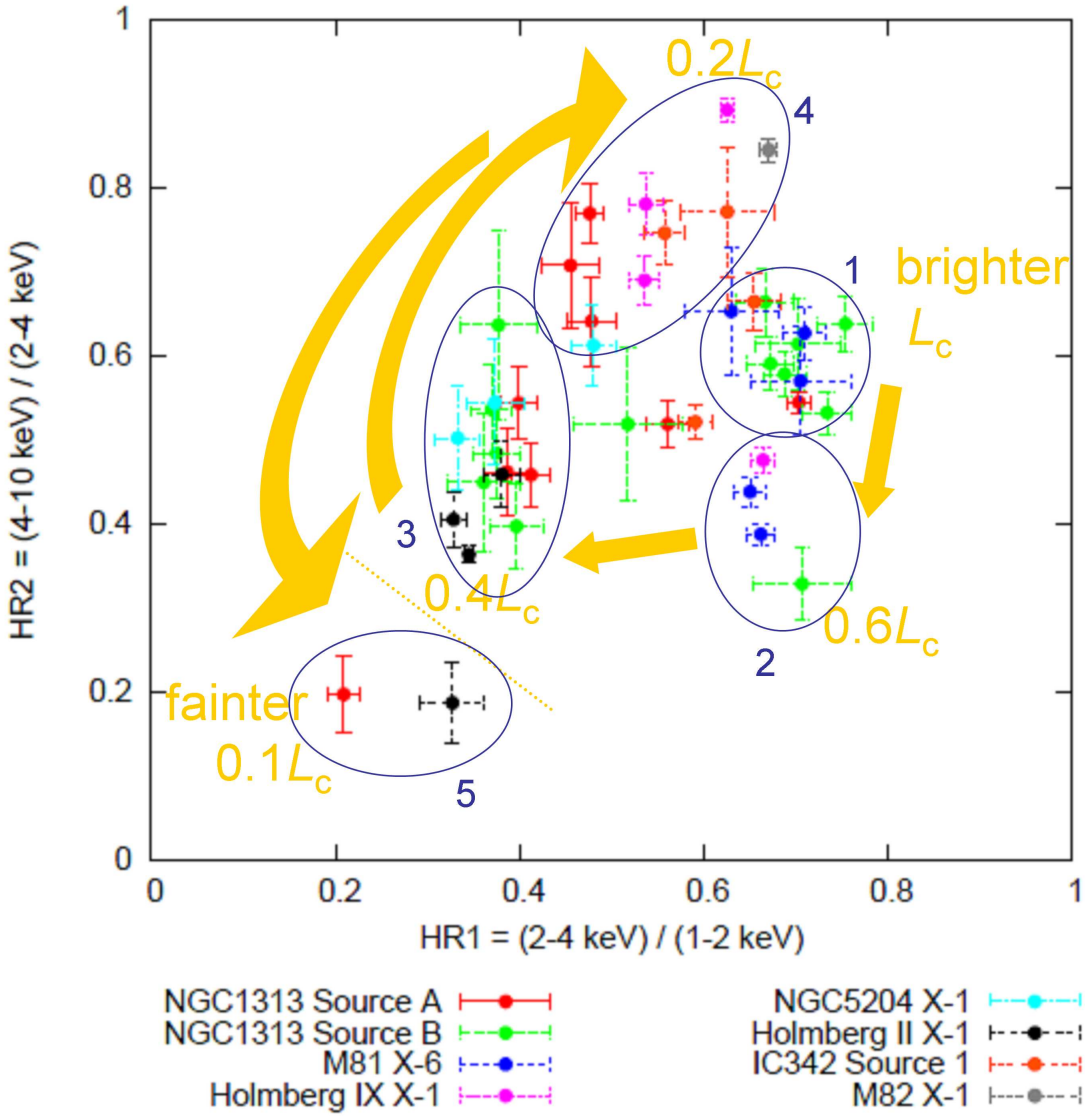

Figure 7.2: The composite CCP combining all the 8 targets, re-calculated using the deconvolved and absorption-removed photon spectra. Indicated in yellow are the luminosities normalized to L_c (see text), and the locus of luminosity-dependent spectral evolution. Five representative regions are indicated in blue.

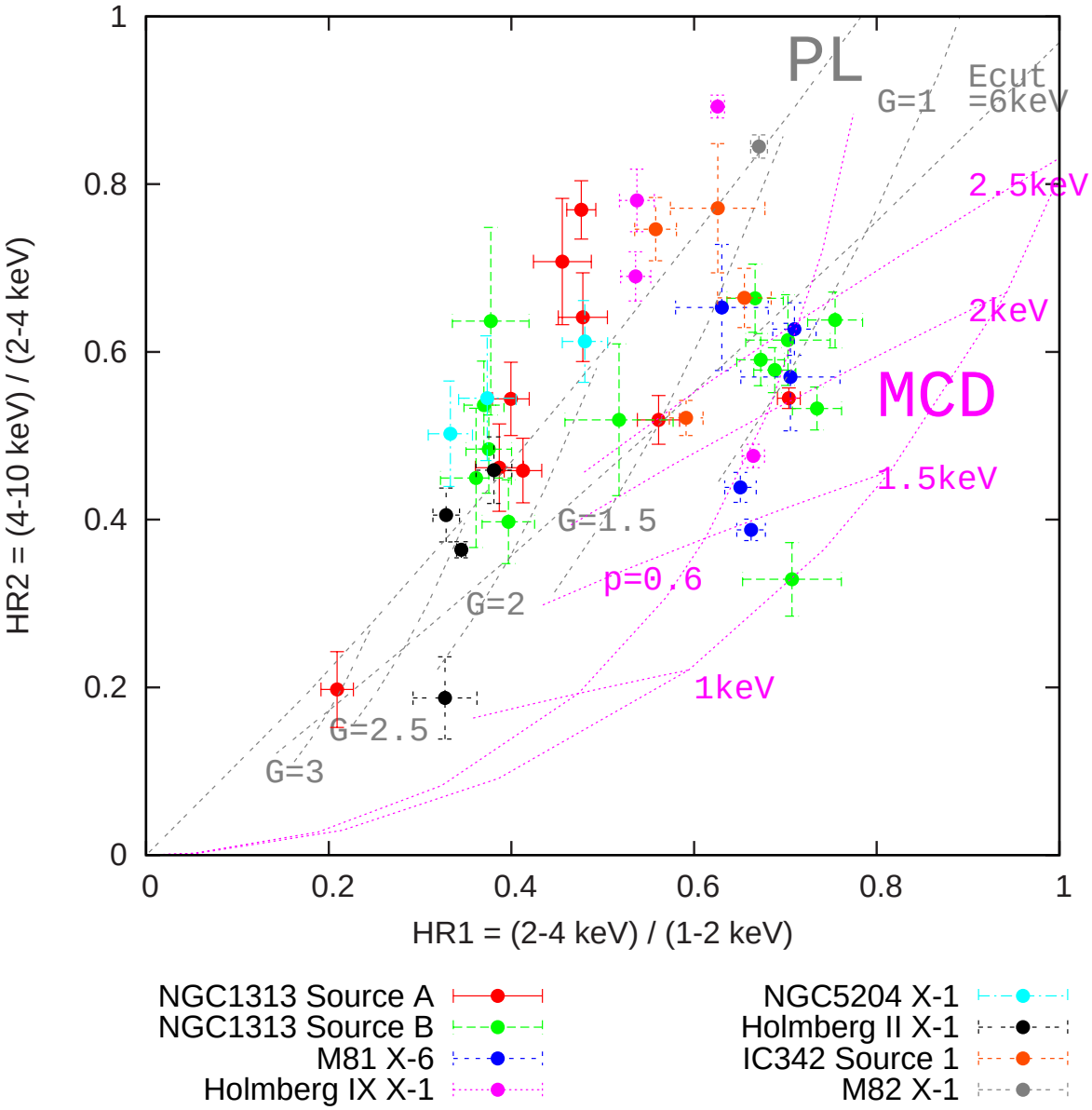

Figure 7.3: The same as figure 7.2, on which grids representing a family of cutoff-PL spectra (gray) and a family of variable-p (including MCD) spectra (magenta) are superposed.

7.2 MCD-type ULXs

Since the overall spectral behavior of our sample ULXs has been clarified in the previous section, here we discuss in further details the sources exhibiting the MCD-type spectra (Regions 1 and 2). Such convex spectra of ULXs were first pointed out by Colbert & Mushotzky (1999), and Makishima et al. (2000).

In order to compare the MCD-type spectra of the sample ULXs with those of Galactic BHBs, we present in figure 7.4 an "H-R diagram" of BHs. This plot is basically the same as figure 5.4 employed in the analysis of M81 X-6 (§§5.1), and figure 5.10 of NGC1313 Source B (§§5.2), but the axis of the band-limited X-ray luminosity has been changed to the bolometric luminosity ($L_{\rm bol}$), obtained from the MCD fits. This plot gives us useful information on the spectral evolution of BHBs and ULXs, and has been extensively utilized by Makishima et al. (2000), Mizuno (2000), Kubota (2001), and Sugiho (2003). When the accretion rate changes, a BH of a given mass moves on this diagram along the constant mass lines described by $L \propto T_{\rm in}^4$, as long as the standard accretion disk is realized. Actually, the typical BHB, LMC X-3, evolves along the constant mass ($\sim 6\ M_\odot$) line, and XTE J1550-564 also obeys the relation in its high/soft state.

In figure 7.4, the data points of XTE J1550-564 start deviating from the constant-mass ralation, as the source gets more luminous, past through the VHS, and then enters the slim-disk state. In this particular source, this "transition" is seen to occur at a luminosity near the Eddington limit with $\eta \sim 0.5$, where η is the bolometric luminosity normalized to the Eddington limit. As described in §§2.2.4, the source behaves as $L \propto T_{\rm in}^2$ beyond this point, in contrast to the canonical $L \propto T_{\rm in}^4$ behavior.

Like XTE J1550-564 in the slim-disk state, four ULXs varied in figure 7.4 approximately along the relation of $L \propto T_{\rm in}^2$; these are M81 X-6, NGC1313 Source B, Holmberg IX X-1, and IC342 Source 1; they exhibited time variability through the *Suzaku* , *XMM–Newton* , and *ASCA* observations, while they were in the MCD-type state. This behavior was already presented in figure 5.4 and figure 5.10. Since this $L \propto T_{\rm in}^2$ scaling is theoretically expected for slim disks (§§2.2.4), these results strengthen the interpretation (Tsunoda et al. 2006) that MCD-type ULXs correspond to BHBs in the slim-disk state. This inference is further reinforced by the results obtained in §§5.1, §§5.2, §§5.3, and §§5.5.3, that the MCD-type spectra in Region 5 and Region 4 (figure 7.2) are generally better described by the variable-p spectra with $p \sim 0.6$, than by a simple MCD model.

From these considerations, we conclude that the ULXs in Region 5 and Region 4 of figure 7.2 harbor slim disks, and are in the same condition as the BHBs in the slim-disk states. As discussed by Kubota et al. (2001) and Tsunoda et al. (2006), this state identification solves the original problem with the MCD-type ULXs, that their disk temperature is too high to be reconciled with their large BH mass required by their high luminosity (Makishima et al. 2000).

Although the above analogy appears to work, these ULXs and the slim-disk BHBs clearly occupy different regions on the H-R disgram, with 1–2 orders of magnitude differences in luminosity. This difference should be ascribed to systematic mass differences between ULXs and BHBs. Further discussion on this point continues in §§7.4.

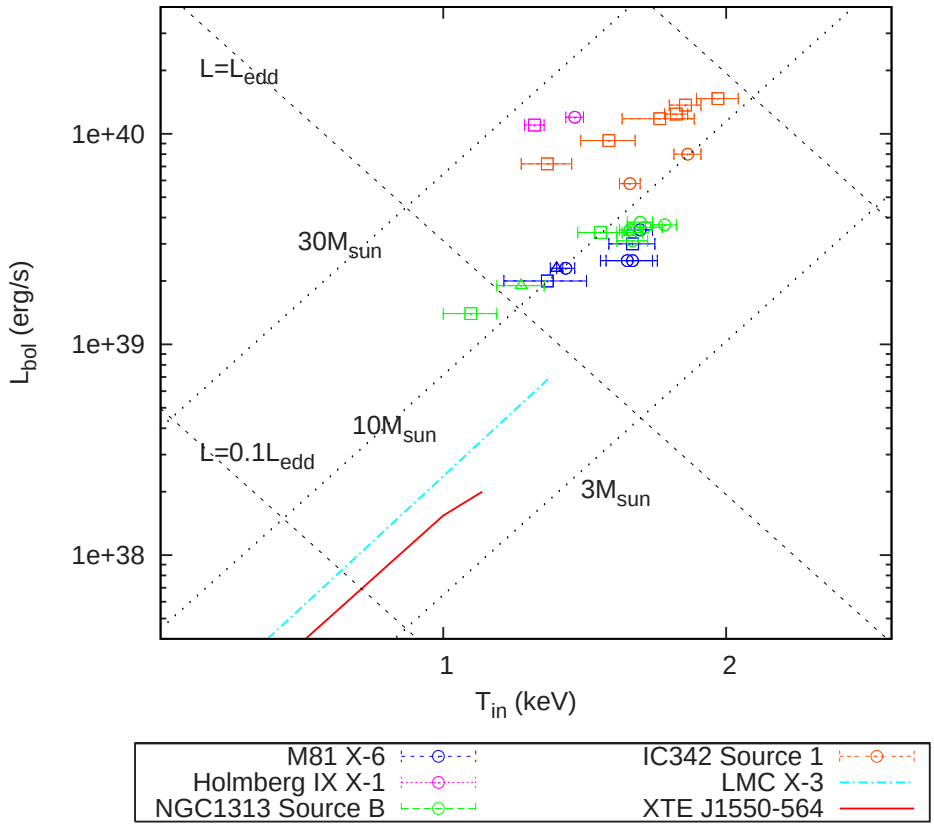

Figure 7.4: A scatter plot between the bolometric luminosity ($L_{\rm bol}$) and the inner-disk temperature ($T_{\rm in}$) of the sample ULXs exhibiting MCD-type spectra, derived through the MCD model fits. The *Suzaku* , *XMM–Newton* , and *ASCA* data are shown in triangles, circles, and squares, respectively. The data of two Galactic/Magellanic BHBs (LMC X-3 and XTE J1550-564) are also drawn with solid lines (from Kubota 2001). The dot-dashed lines indicate constant BH mass grid, calculated from equation 2.10. The dashed lines indicate equation 2.11. The system inclination angle is assumed to be 0°.

7.3 PL-type ULXs

As described in §§7.1, sources in Region 2 and Region 3 on the CCP (figure 7.2) exhibit PL-dominant spectra with $\Gamma = 1.5$–2.5. Such PL-like spectra, first detected with *ASCA* from a few ULXs (Makishima et al. 2000; Kobuta et al. 2001), were later found in a much larger number of ULXs through *Chandra* and *XMM–Newton* observations (e.g., Miller et al. 2003; Roberts et al. 2004). At first, these ULXs had been thought to be in the low/hard state typically observed in Galactic/Magellanic BHBs (§§2.5.2; Kubota et al. 2001). However, based on the detailed spectral analysis of IC342 Source 1 with *ASCA* , and a consideration of the transition luminosity, it has been argued that PL-type ULXs are more reasonably interpreted as corresponding to stellar BHBs in the VHS, where their spectra are dominated by a PL component from an unsaturated thermal Comptonization process of some soft seed photons (§§2.5.4; Kubota et al. 2002). Our working hypothesis, summarized in Chapter 1 also invokes this interpretation.

7.3.1 Similarity with BHBs in the VHS

To examine whether our results support the hypothesis that PL-type ULXs correspond to BHBs in the VHS, let us summarize below the present results on our PL-type sources.

1. As seen in the CCP (figure 7.2), the PL-type sources in our sample have their luminosities in the range 0.2–0.4 $L_{\rm c}$. In other words, their luminosities are 0.2–0.4 times those which they would exhibit in the MCD-type state. This compares favorably with the fact that the VHS of stellar BHBs appears at lower (by typically several tens percent) luminosity than their slim-disk state.

2. The photon index of many PL-type sources are found at $\Gamma = 2$–2.5 (Region 3 in the CCP), which are very close to those of stellar BHBs in the VHS ($\Gamma \sim 2.5$; Kubota 2001), although some PL-type ULXs exhibit harder spectra with $\Gamma \sim 1.5$ (Region 2 in the CCP).

3. The presence of a soft-excess component in many PL-type ULXs, expressed by an MCD model with $T_{\rm in} \sim 0.3$ keV, is consistent with the weak MCD component which is generally present in the VHS of BHBs, veiled by the dominant PL component.

4. When the luminosity increases from Region 4 to Region 3, the ULX spectra become softer as $\Gamma = 1.5 \rightarrow 2.5$. This property can be explained naturally by a Compton cooling process that is invoked to explain the VHS of BHBs: an increased soft photon flux enhances electron cooling of the Comptonizing plasma.

5. The QPO detections from typical PL-type ULXs (M82 X-1 and Holmberg IX X-1) by several authors (§§2.6.2) agrees with the fact that QPOs of stellar BHBs have often been observed most strongly in their VHS.

These results altogether support and strengthen the interpretaion that PL-type ULXs are in the same physical state as Galactic BHBs in the VHS.

7.3.2 Spectral turn-over

Although many properties observed in the PL-type ULXs correspond to those of Galactic BHBs in their VHS, there are some differences between them. In particular, as already described in Chapter 5 and Chapter 6, some PL-type spectra exhibit high-energy spectral declines at ~ 6 keV as expressed by a cutoff-PL model. Although this effect itself was already observed from BHBs in their VHS (Kobayashi et al. 2003), the turn-over energies observed from PL-like ULXs are significantly lower than those observed in the VHS of Galactic BHBs. To visualize this relation, we plot in figure 7.5 the cutoff energies against the luminosity of four ULXs, NGC1313 Source A (§§5.4), Holmberg IX X-1 (§§5.3), Holmberg II X-1 (§§5.5.1), and M82 X-1 (§§6.2); the data points refer to those spectra which exhibit significant spectral cutoff under relatively high photon statistics. We also present in figure 7.5 data of the Glactic transient BHB, GRO J1550-564 in the VHS (Kobayashi et al. 2003). We can see that the cutoff energies (5–10 keV) of ULXs are more than an order of magnitude lower than that (200–300 keV) of the BHBs.

Such lower cutoff energies of ULXs suggest that their putative Comptonizing plasmas have lower electron temperatures ($T \sim 2$ keV) and higher optical depths ($\tau \sim 10$) than those in the VHS of BHBs. These properties of ULXs have already been reported by several authors (e.g., Stobbert et al. 2006; Dewangan et al. 2006), although the reality and physical details of Compton scattering with such low electron temperatures and large optical depths are a subject of future study.

As another BH object, we also plot in figure 7.5 a data point obtained from an AGN,

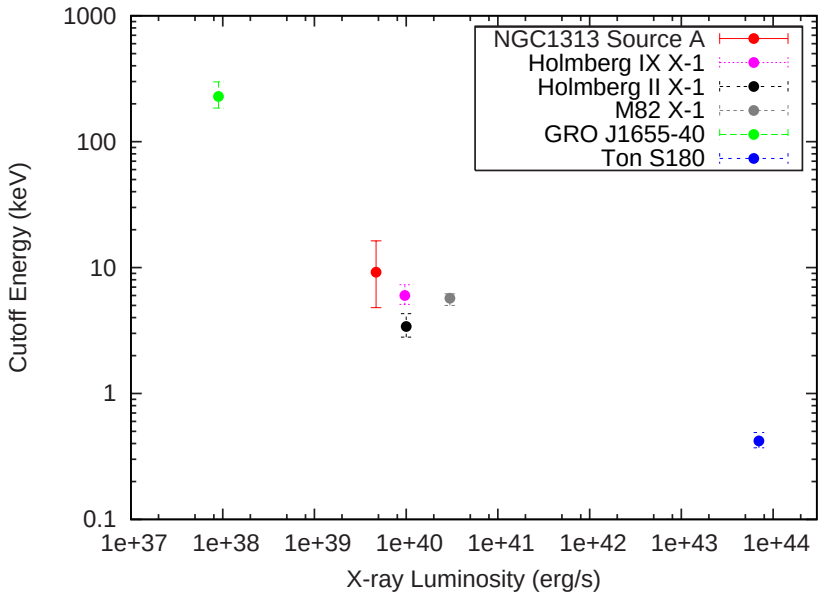

Figure 7.5: A scatter plot between the luminosity and cutoff energy, obtained from four PL-type ULXs exhibiting significant high-energy spectral turn over. For comparison, data of the BHB, GRO J1655-40 (Kobayashi et al. 2003) in the VHS, and a narrow-line Seyfert 1 galaxy, Ton S180 (Murashima et al. 2006), are also presented.

the narrow line Seyfert 1 galaxy Ton S180 (Murashima et al. 2006). These authors successfully explained the soft excess of this narrow-line Seyfert 1 galaxy in terms of a cutoff PL model with $E_{\rm cut} \sim 0.4$ keV, so that it may be interpreted as analogous to the VHS. Including this data point, we can see in figure 7.5 a clear negative correlation between the cutoff energy and the luminosity, through the Galactic BHB, ULXs, and the AGN. In other words, objects with higher luminosity ($\simeq$ higher mass) are suggested to show lower cutoff energies. This result suggests that ULXs indeed harbor BHs which have intermediate masses between stellar BHBs and AGNs. The negative correlation seen in figure 7.5 may be explained, at least qualitatively, that a more massive object has a lower Compton-cloud temperature because it has a lower cool-disk temperature ($\propto M_{\rm BH}^{-\frac{1}{4}}$), and hence a more enhanced cooling of the Compton cloud.

7.4 Mass Estimation

Using the information obtained so far, how can we estimate the BH mass of ULXs? For this purpose that is essential to the ULX study, let us define a parameter $\eta_{\rm c}$, which relates the normalizing luminosity $L_{\rm c}$ to the Eddington luminosity $L_{\rm E}$ as

$$L_{\rm c} = \eta_{\rm c} L_{\rm E}. \tag{7.1}$$

If we can obtain the value of $\eta_{\rm c}$ for individual sources, eq. 2.1 would allow us to estimate the BH mass as

$$M = \frac{1}{\eta_{\rm c}} \times (\frac{L_{\rm c}}{1.5 \times 10^{38} {\rm erg\ s^{-1}}}) \times M_{\odot}. \tag{7.2}$$

In this section, we try to estimate the values of $\eta_{\rm c}$ through semi-quantitative comparison of ULXs with BHBs.

7.4.1 Comparison with BHBs

In order to directly compare $L_{\rm c}$ of ULXs with the luminosity-dependent state changes of BHBs, we plot in figure 7.6 data points of two transient BHBs in our Galaxy, XTE J1550-564 and 4U 1630-47, on the same CCP as figure 7.2. These data were calculated using the best-fit MCD + PL model from Kubota & Makishima (2004) for XTE J1550-564, and Abe et al. (2005) for 4U 1630-47. These two BHB exhibited three spectral states; the high/soft state, the VHS, and the slim-disk state. We can see in figure 7.6 that the three spectral states of these BHBs are roughly separated into three regions on the CCP.

1. Data points in the slim-disk state of the two Galactic BHBs are located at (HR1, HR2) = (0.5–0.7, 0.3–0.5). This location is nearly the same as Region 2 in figure 7.2 for the ULXs. This supports the interpretation that ULXs with MCD-type spectra are analogous to Galactic BHBs in the slim-disk state.

2. When the BHBs are in the VHS, their data points appear at (HR1, HR2) = (0.4–0.5, 0.4–0.5). This region roughly coincides with Region 3 of ULXs, again supporting that the PL-type ULXs correspond to BHBs in the VHS.

3. Data of the BHBs in the high/soft state are located at the lower-left region on the CCP at (HR1, HR2) = (0.4–0.5, 0.1–0.3), which is close to the location of Region

Table 7.2: Parameters of typical four BHBs.

	$M_{\rm BH}$	i	$L_{\rm E}$ (10^{39} erg s^{-1})	Slim-disk*	VHS*	High/Soft*	ref.
XTE J1550-564	8.4–11.2	67°–75°	~ 1.5	0.5–0.3	0.3–0.2	0.2–	a
4U 1630-47	3.4–5.1	–	~ 0.6	~ 0.4	~ 0.4	0.4–	b
GRO 1655-40	5.8–7.9	64°–71°	~ 1.1	–	0.17–0.1	0.1–	c
LMC X-3	5–7.2	65°–69°	~ 0.9	–	–	0.9–	d

*: Spectral states, and the range of $L/L_{\rm E}$.

a: Kubota & Makishima (2004) b: Abe et al. (2005) c: Kubota et al. (2001) d: Kubota (2001)

5 of ULXs. This supports our inference made in §7.1 that the two ULXs on these occasions host standard (Shakura-Sunyaev type) accretion disks.

Figure 7.7 illustrates the luminosity ranges, in terms of η, of the four accretion states actually observed from three BHBs, LXC X-3, GRO J1655-40 (Kubota et al. 2001), and XTE J1550-564 (Kubota & Makishima 2004); their specific parameters refer to table 7.2. Figure 7.7 does not show 4U 1630-47, since its distance, hence $L_{\rm E}$, is only poorly known. The systematic differences seen among these BHBs is considered to reflect uncertainties in their distances, masses, and inclinations, as well as their BH spin parameters (Kubota et al. 2001) which is almost unconstrained. Those of our sample ULXs are also presented as a function of $L/L_{\rm c}$. This diagram allows us to define a correspondence between η of BHBs and $L/L_{\rm c}$ of ULXs, mainly referring to their transition luminosities, and hence to estimate the value of $\eta_{\rm c}$ of our sample ULXs. Among these BHBs, LMC X-3 is known to stay in its high/soft state up to $\eta \sim 0.9$. Since the transition point from high/soft (Region 5) to very-high (Region 4) states in our ULXs is at about $0.2L_{\rm c}$ (table 7.1), we obtain $\eta_{\rm c} \sim 4$ if referring to LMC X-3. Alternatively, GRO J1655-40 is known to make transitions from its high/soft state to its VHS at $\eta \sim 0.1$. If using this value, we obtain $\eta_{\rm c} \sim 1$. Finally, XTE J1550-564 becomes as luminous as $\eta \sim 0.5$ when it is in the slim-disk state. If considering this case, a value of $\eta_{\rm c} \sim 0.5$ is derived.

In table 7.3, we summarize the masses of individual sample ULXs estimated in this way, employing the three estimates of $\eta_{\rm c}$; 0.5, 1, and 4. Thus, the estimated masses of ULXs range from several tens $M_\odot$to several hundreds $M_\odot$.

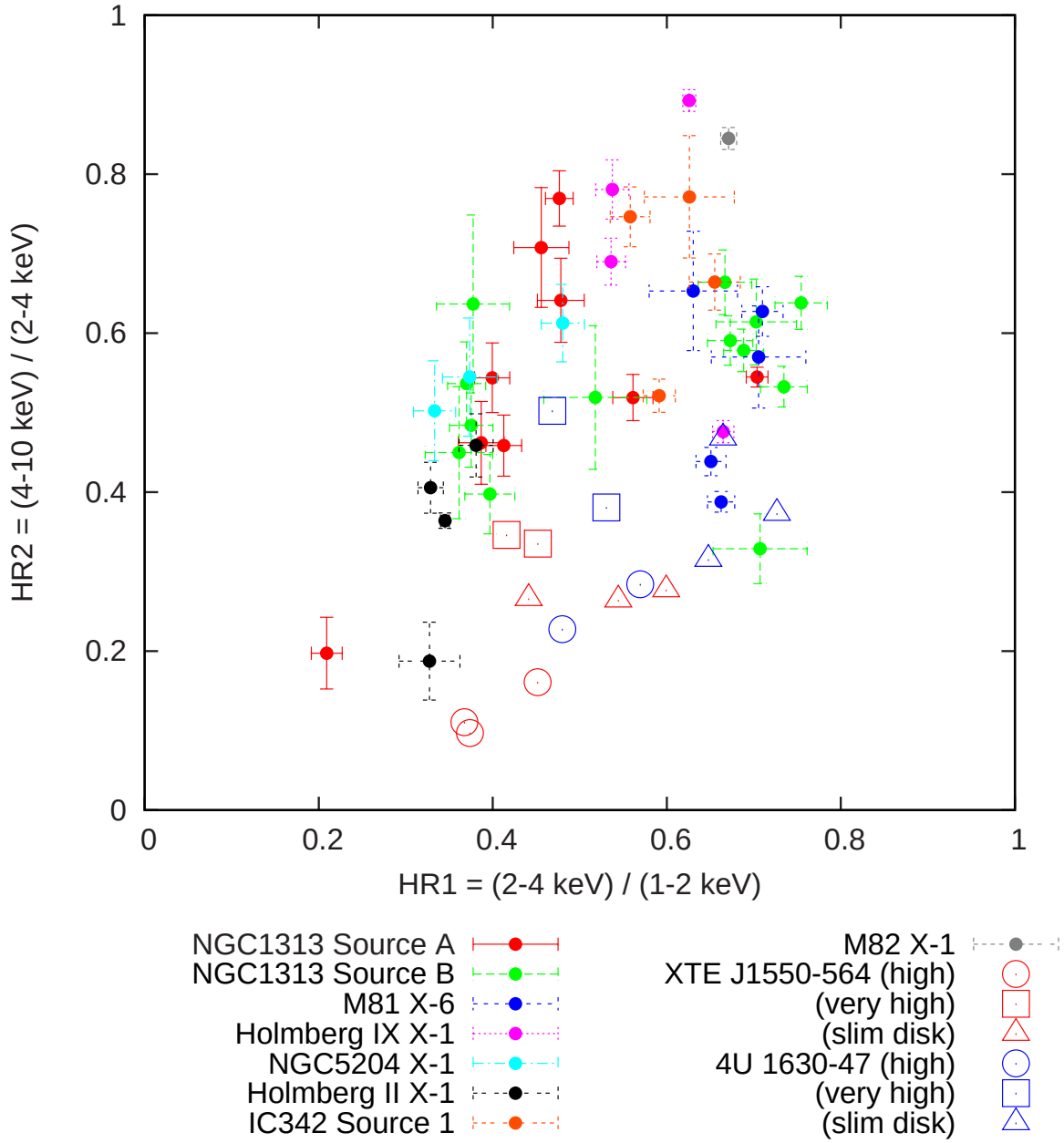

Figure 7.6: The same as figure 7.2, but combined with data points obtained from two Galactic BHBs, XTE J1550-564 (Kubota & Makishima 2004) and 4U 1630-47 (Abe et al. 2005).

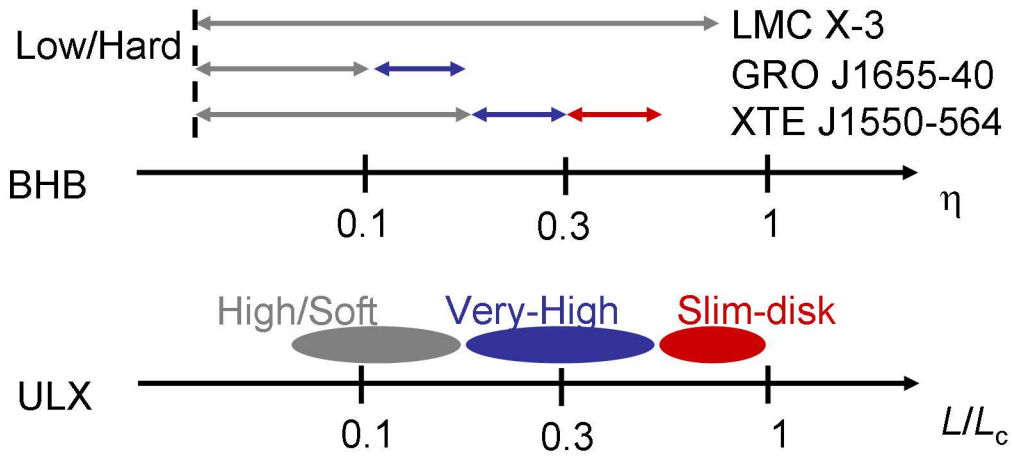

Figure 7.7: A schematic comparison of luminosity-dependent spectral states, expressed by η for three Galactic/Magellanic BHBs (LXC X-3, GRO J1655-40, and XTE J1550-564) and by $L/L_{\rm c}$ for our sample ULXs.

Table 7.3: A summary of the estimated ULX masses.

Source	$L_{\rm c}$	$\eta_{\rm c}=4$	$\eta_{\rm c}=1$	$\eta_{\rm c}=0.5$	$R_{\rm in}$ (Region 3 or 4)	$R_{\rm in}$ (Region 5)
NGC1313 Source A	2×10^{40}	$30M_\odot$	$130M_\odot$	$270M_\odot$	$180^{+20}_{-60}\ M_\odot$	$660^{+520}_{-310}\ M_\odot$
NGC1313 Source B	7×10^{39}	$10M_\odot$	$50M_\odot$	$90M_\odot$	–	–
M81 X-6	7×10^{39}	$10M_\odot$	$50M_\odot$	$90M_\odot$	–	–
Holmberg IX X-1	(4×10^{40})	$70M_\odot$	$270M_\odot$	$530M_\odot$	$140^{+20}_{-10}\ M_\odot$	–
Holmberg II X-1	(4×10^{40})	$70M_\odot$	$270M_\odot$	$530M_\odot$	$220^{+10}_{-20}\ M_\odot$	$260^{+300}_{-120}\ M_\odot$
NGC5204 X-1	(2×10^{40})	$30M_\odot$	$130M_\odot$	$270M_\odot$	$100^{+60}_{-30}\ M_\odot$	–
IC342 Source 1	1.3×10^{40}	$20M_\odot$	$90M_\odot$	$170M_\odot$	–	–
M82 X-1	(1×10^{41})	$160M_\odot$	$670M_\odot$	$1300M_\odot$	–	–

7.4.2 Mass estimation from the soft-excess modeling

As an independent method of ULX mass estimation, we may utilize the soft-excess components observed in 4 objects, Holmberg IX X-1 (§5.3), NGC1313 Source A (§5.4), Holmberg II X-1 (§§5.5.1), and NGC5204 X-1 (§§5.5.2). If the emission originates in a standard accretion disk, we can obtain a value of its inner-disk radius $R_{\rm in}$ from the MCD model fit. As described in §§2.2.2, we can then estimate the mass of the central BH from $R_{\rm in}$ using eq. 2.8. Here, we may assume for simplicty that $R_{\rm in}$ corresponds to the radius of the last stable orbit and the central object is a Schwarzshild BH ($\alpha = 1$), although this assumption may not be necessarily justified.

The column before the last in table 7.3 gives the ULX masses estimated in this way, using the spectra in Region 3 or 4. In calculating these results, we utilized the best constrained value of $R_{\rm in}$ from the multiple observations of each object. The estimated masses result in 100–200 $M_\odot$, which are generally consistent with those derived in the previous subsection. More specifically, the BH mass of each object derived here falls on a relatively lower range of those estimated from the transition luminosities, corresponding to $\eta_{\rm c} = 1$–2 typically. However, as revealed by Kubota et al. (2001) and Kubota & Makishima (2004) concerning BHB in the VHS, the cool (and presumably standard) disk emission is partially "taken up" by the Comptonizing corona, and transformed into the PL-like harder continua. Since this effect is known to make $R_{\rm in}$ systematically smaller, the values in this column (before the last) are likely to be rather under-estimated.

The last column of table 7.3 provides the mass estimates for the two ULXs which entered Region 5, or the standard high/soft state according to our state assignments. Although these estimates are subject to rather large uncertainties, they are again consistent with the other estimate, and tend to give higher masses than the data from Regions 3 and 4. This is possibly because the cool disk in this state is no longer affected by strong Comptonization, which caused the potential problems in Regions 3 and 4.

From these multiple and independent considerations, we conclude that many of the sample ULXs have their BH mass in the range which is significantly higher than that for the ordinary stellar BHs. Although some of them could have 10–20 $M_\odot$under the extreme assumption of $\eta_{\rm c} \sim 4$, the others do require the higher masses.

7.5 Some Implications

To complete our discussion, let us briefly consider implications of the present results from somewhat wider aspects.

7.5.1 Possibility of highly super-Eddington emission

As explained in Chapter 1, the competing scenario interprets ULXs as ordinary-mass stellar BHs under highly super-Eddington ($\eta > 5$) emission. This view is based on the fact that some ULX spectra can be reproduced by a variable-p model with $p \simeq 0.6$ and a rather high disk temperature ($T_{\rm in} \gtrsim 2.5$ keV), and that such a spectrum is *theoretically* expected to emerge from slim disks that are under extremely high accretion rates. The representative case is an *XMM–Newton* spectrum of M82 X-1. This spectrum was shown by Okajima et al. (2006) to be reproduced by a variable-p model with $p \sim 0.61$ and $T_{\rm in} \sim 3.7$ keV, which could be interpreted as an ordinary-mass ($\sim$ 20–30 $M_\odot$) BH with a super-Eddington ($\eta \sim 5$) luminosity. Although the data set utilized by Okajima et al. (2006) differs from those we analyzed utilizing the *Chandra* and *Suzaku* observations in Chapter 6, M82 X-1 at that time exhibited a flux of $\sim 3 \times 10^{-11}$ erg s^{-1}cm^{-2} which is close to those measured in the *Chandra* and *Suzaku* analysis.

To evaluate the above issue, we re-considered the results obtained with our *Chandra* and *Suzaku* analysis. From the *Chandra* analysis, as described in section 6.1 and section 7.1, the M82 X-1 spectrum, successfully represented by a PL model of $\Gamma \sim 1.6$, was located close at the VHS region (Region 4) on our CCP (figure 7.2). Because the *Chandra* spectrum was limited in the lower energy range ($\lesssim 7$ keV), the spectral convex shape, characteristic of the variable-p or cutoff-PL model, cannot be measured. Therefore, we re-analyzed the *Suzaku* XIS + HXD data (3–20 keV) in the same manner as Okajima et al. (2006), neglecting for simplicity any contamination from the surrounding sources or from M81. As a result, we found that the *Suzaku* spectra of M82 X-1 can be reproduced by a variable-p model with $p = 0.63 \pm 0.02$ and $T_{\rm in} = 3.6^{+0.3}_{-0.2}$, which are very close to those obtained by Okajima et al. (2006). The obtained fit goodness, $\chi^2/\nu = 191.9/181$, is comparable to (or even slightly better than) that with our cutoff-PL fit ($\chi^2/\nu = 193.6/181$; table 6.1). In other words, our cutoff-PL modeling (leading to the VHS interpretation) and that with the variable-p model (leading to the slim-disk interpretation) degenerates,

and cannot be distinguished even employing the HXD-PIN data. This is not surprising, since the upper ends of Region 1 (the slim-disk state) and Region 4 (our VHS interpretation) come close together on the CCP (figure 7.2), and M82 X-1 just falls onto this nearly overlapping region.

Even though the two interpretations of M82 X-1 cannot be distinguished from the data alone, we can examine the two alternative scenarios for their overall consistency. During the present *Suzaku* observation (as well as in the *XMM–Newton* observation utilized by Okajima et al. 2006, and the *Chandra* observation in section 6.1), M82 X-1 was some 3 times dimmer than its highest-luminosity record known to date. Here, in order to analyze a M82 X-1 spectrum with the highest luminosity, we revisited archival data acquired with the *RXTE* satellite. We utilized an observation on 1997-11-02 (ID:20303-02-07-00), because on that occation Rephaeli & Gruber (2002) reported that M82 X-1 showed the highest luminosity at $\sim 1 \times 10^{41}$ erg s^{-1}. As a result of our re-analysis, the 3–20 keV *RXTE* spectrum was successfully reproduced by either a cutoff-PL model with $\Gamma = 0.75 \pm 0.20$, $E_{\rm cut} = 4.5^{+0.7}_{-0.5}$ keV, ($\chi^2/\nu = 44.6/42$), or a variable-p disk model with $T_{\rm in} = 3.0 \pm 0.2$ keV, $p = 0.60 \pm 0.03$, ($\chi^2/\nu = 46.8/42$).

Considering all these results from *Suzaku* , *XMM–Newton* , and *RXTE* , if we assume that M82 X-1 was in the slim-disk state through the three observations, we confront with the following difficulties.

1. In our CCP, the slim-disk state (Region 1 and Region 2) is observed at the highest luminosity of individual objects, and any ULX did not vary in luminosity by more than a factor of two or so within this state. Similarly, the luminosity of XTE J1550-564 (the transient BHB) has been observed to saturate strongly, as it enters the slim-disk state (Kubota & Makishima 2004). It would be unreasonable to assume that only M82 X-1 can vary by a factor of ≥ 3 in luminosity while it is in the slim-disk state.

2. The values of $T_{\rm in} \sim 3$–4 keV obtained with the variable-p model from these spectra of M82 X-1, particularly those in the dimmer state, are higher than those (1.5–2.5 keV) observed from the other targets in our sample that are interpreted in the slim-disk state. There would be no reasonable explanation for this high value of $T_{\rm in}$, given that M82 X-1 is considered to be the most massive object in our sample, and hence is expected to show generally lower disk temperatures than the others.

3. The value of $T_{\rm in} = 3.0 \pm 0.2$ keV in the highest luminosity state obtained with *RXTE* is lower than those (~ 3.5 keV) in the dimmer state measured with *Suzaku* and *XMM–Newton* . This is inconsistent with the relation that $T_{\rm in}$ varies with the luminosity approximately as $L \propto T_{\rm in}^2$ (our figure 7.4 and Watarai et al. 2001).

4. The obtained values of $p \sim 0.6$ are constant within errors of ± 0.03 between the dimmer and highest luminosity states. This disagrees with the theoretically predicted (Watarai et al. 2001) and observationally confirmed (figure 5.11) slim-disk behavior, that p decrease down to 0.5 as the luminosity increase (§§2.2.4).

From these considerations, we consider it difficult to regard M82 X-1 as residing in the slim-disk state at least during the two dimmer occasions observed by *Suzaku* and *XMM–Newton* , and it is natural to interpret that these two are in the VHS. This is contrary to the interpretation by Okajima et al. (2006) that it was in the slim-disk state in the *XMM–Newton* occasion.

On the other hand, how about the highest luminosity state observed by *RXTE* ? One possibility is that M82 X-1 was in the VHS in the highest luminosity phase as well. This interpretation is feasible, from the following two aspects.

1. The cutoff energies of $E_{\rm cut} \sim 4$–7 keV on the three occasions are almost the same as those observed from the other ULXs in our sample that are interpreted to be in the VHS.

2. The cutoff energy ($4.5^{+0.7}_{-0.5}$ keV) at the highest luminosity phase is nearly the same as, or lower than, those (5–7 keV) at the dimmer phase. If the cooling of the cutoff energy is real, this is possibly due to an effect of Compton cooling.

Alternatively, we may interpret that M82 X-1 was in the slim-disk state when observed with *RXTE* . This view is also consistent with our overall picture, based on the following considerations.

1. The luminosity relation between the dimmer state and the highest luminosity is consistent with that between the VHS and the slim-disk state observed in our sample ULXs.

2. Although the value of $T_{\rm in} \sim 3.5$ keV derived in the dimmer state is too high, that in the highest-luminosity state, 3.0 ± 0.2 keV, is comparable with the highest temperature in our slim-disk sample (~ 2.8 keV from NGC1313 Source B on 2003-12-21 in table 5.2).

3. The value of $p \sim 0.6$ is consistent with those from the other ULXs in the slim-disk state in our sample.

Thus, the state classification of M82 X-1 in the most luminous state is ambiguous; it can either be in the VHS, or in the slim-disk state.

The mass constraint for M82 X-1, derived in table 7.3 assuming $L_{\rm c} \sim 1 \times 10^{41}$ erg s^{-1}, is considered to remain valid, in the case that the most luminous state corresponds to the slim-disk state. On the other hand, when the luminous state is the VHS, we need a larger value of $L_{\rm c}$ than 1×10^{41} erg s^{-1}, which introduces a larger mass for M82 X-1. In both cases, the value of mass ($\gtrsim 160\ M_\odot$ even if $\eta \sim 4$) becomes significantly larger than an ordinary ($\lesssim 30\ M_\odot$) one, as far as the value of η is $\lesssim 5$.

In conclusion, the results derived in the present thesis argue against the slim-disk interpretation of the M82 X-1 spectra taken at rather dimmer state, even though the variable-p model gives an acceptable fit. This in turn weakens the grounds for the ordinary-mass interpretation of ULXs, and instead, strengthen our working hypothesis proposed, e.g., by Sugiho (2003).

7.5.2 Other ULXs

Although we have thus constructed a unified scenario using the 8 ULXs, it is not clear whether the scenario can be applied to other ULXs in general, since our sample is neither complete nor objectively well defined. Indeed, ULXs could be an inhomogeneous mixture of more than one populations. Some of them could actually be ordinary-mass stellar BHs under super-Eddington emission, or could even be highly beamed X-ray emitters.

In spite of the above ambiguity, we believe that the present results have a high significance, because we have successfully shown that at least a considerable fraction of ULXs, including in particular the most prototypical ones, form a population that is distinct from ordinary stellar-mass BHs. The apparent absence of this population in the Local Group galaxies could be related their formation, although the discussion on this point is beyond

the scope of the present thesis. We mention an interesting effect found by Sugiho (2003), that PL-type ULXs are found preferentially in early-type spirals, whereas MCD-type ones in late-type spirals.

Chapter 8

CONCLUSION

In the present thesis, we have analyzed the spectra of typical 8 ULXs (NGC1313 Source A, NGC1313 Source B, M81 X-6, Holmberg IX X-1, Holmberg II X-1, IC342 Source 1, NGC5204 X-1, and M82 X-1) in nearby (< 5 Mpc) galaxies, whose luminosity reaches 5×10^{39} erg s^{-1}. Through investigations of their spectral changes using the multiple *Suzaku* and *XMM–Newton* observations, we have found the 8 sample ULXs to exhibit a common luminosity-dependent spectral evolution. Based on this unified behavior of the 8 ULXs, and invoking an analogy to the behavior of Galactic BHBs, we can draw the following conclusions.

1. When more luminous than on other occasions, the sample ULXs exhibit a rather convex spectral shape, which prefer an MCD model fit to a PL model fit. The fit is further improved by employing a variable-p disk model with $p \sim 0.6$ instead of the simple MCD model. Furthermore, their luminosity changes approximately as $L \propto T_{\rm in}^2$. These properties strengthen the interpretation that these MCD-type ULXs are in a state analogous to the slim-disk state observed in Galactic BHBs at their highest luminosities.

2. When the luminosity decreases to 0.2–0.4 times that in the MCD-type state, the ULX makes a clear transition to a state where the spectrum is approximately expressed by a PL model with $\Gamma = 1.5$–2.5. During the PL-type state, the PL-type spectrum softens as the luminosity increases. We can hence interpret these PL-type ULXs as residing in a state which is analogous to the VHS of Galactic BHBs.

3. Some PL-type spectra are accompanied by a soft-excess component described by an MCD model with $T_{\rm in} \sim 0.3$ keV, together with a high-energy spectral turn over expressed by a cutoff-PL model with $E_{\rm cut} \sim 6$ keV. In particular, such a spectral curvature at ~ 6 keV was clearly observed from M82 X-1, utilizing the broad energy band up to ~ 20 keV provided by the *Suzaku* HXD. These properties can be consistently explained by the scenario for the VHS of Galactic BHBs, that soft photons from a cool accretion disk are Comptonized by a hot corona surrounding the disk. The cutoff energies observed from PL-type ULXs are significantly lower than those observed in the Galactic BHB, GRO J1655-40, in its VHS.

4. At the lowest luminosity, two ULXs, NGC1313 Source A and Holmberg II X-1, exhibited very soft spectra approximately expressed by a PL model with $\Gamma \sim 3$. Since the spectrum is better explained by adding a cool disk contribution at the softest spectral region, this state is considered analogous to the well established high/soft state of BHBs. This further suggests that the two ULXs harbored, on these occasion, a standard Shakura-Sunyaev accretion disk that is truncated at the last stable orbit around the central BH.

5. Combining these results altogether, we infer the sample ULXs as radiating at luminosities that not largely exceed their Eddington limits. This requires them to have rather high Eddington limits. As a result, the mass of our sample ULXs can be estimated as several tens to several hundreds $M_{\odot}$, which is significantly massive than those of stellar BHBs observed in our Galaxy and the Magellanic clouds.

List of Figures

List of Tables

Bibliography

[1] Abe, Y., Fukazawa, Y., Kubota, A., et al. 2005, PASJ, 57, 629

[2] Abramowicz, M.A., Czerny, B., Lasota, J.P. et al. 1988, ApJ, 332, 646

[3] Agrawal, V.K. & Misra, R. 2006, ApJ, 638, L83

[4] Angelini, L., Loewenstein, M., Mushotzky, R.F. 2001, ApJ, 557, L35

[5] Begelman, M.C. 1978, MNRAS, 184, 53

[6] Begelman, M.C. 2002, ApJ, 568, 97

[7] Bethe, H.A. & Brown, G. E. 1995, ApJ, 445, L129

[8] Boldt, E. 1987, Phys.Rep., 146, 215

[9] Bolton, C.T. 1972, Nature, 235, 271

[10] Cappi, M., Persic, M., Bassani, L., et al. 1999, A&A, 350, 777

[11] Colbert, E.J.M. & Mushotzky, R.F. 1999, ApJ, 519, 89

[12] Colbert, E.J.M. & Ptak, A. 2002, ApJS, 143, 25

[13] Collura, A., Reale, F., Schulman, E., et al. 1994, ApJ, 420, L63

[14] Cropper, M., Soria, R., Mushotzky, R.F. et al. 2004, MNRAS, 349, 39

[15] Davis, J.E. 2001, ApJ, 562, 575

[16] Dewangan, G.C., Miyaji, T., Griffiths, R.E., et al. 2004, ApJ, 608, L57

[17] Dewangan, G.C., Titarchuk, L., Griffiths, R.E. 2006, ApJ, 637, L21

[18] Dewangan, G.C., Griffiths, R.E., Rao, A.R. 2006, ApJ, 641, L125

[19] di Matteo, T. & Psaltis, D. 1999, ApJ, 526, L101

[20] Dotani, T., Inoue, H., Mitsuda, K., et al. 1997, ApJ, 485, 87

[21] Dubus, G., Charles, P.A., Long, K.S., et al. 1997, ApJ, 490, L47

[22] Ebisawa, K. 1991, Ph.D thesis, Univ. of Tokyo

[23] Ebisawa, K., Makino, F., Mitsuda, K., et al. 1993, ApJ, 403, 684

[24] Ebisawa, K., Ueda, Y., Inoue, H., et al. 1996, ApJ, 467, 419

[25] Ebisawa, K., Zycki, P., Kubota, A., et al. 2003, ApJ, 597, 780

[26] Ebisuzaki, T., Makino, J., Tsuru, T.G., et al. 2001, ApJ, 562, L19

[27] Ezoe, Y., Iyomoto, N., Makishima, K. 2001, PASJ, 53, 69

[28] Fabbiano, G., & Trinchieri, G. 1987, ApJ, 315, 46

[29] Fabbiano, G. 1988, ApJ, 330, 672

[30] Fabbiano, G., Gioia, I., Trinchieri, G. 1989, ARA&A, 27, 87

[31] Fabbiano, G., Kim, D.W., Trinchieri, G. 1992, ApJS, 80, 531

[32] Fabbiano, G., Zezas, A., Murray, S.S. 2001, ApJ, 554, 1035

[33] Feng, H. & Kaaret, P. 2005, ApJ, 633, 1052

[34] Fiorito, R. & Titarchuk, L. 2004, ApJ, 614, L113

[35] Freedman, W.L., Hughes, S.M., Madore, B.F., et al. 1994, ApJ, 427, 628

[36] Fryer, C.L. & Kalogera, V. 2001, ApJ, 554, 548

[37] Giacconi, R., Gursky, H., Paolini, F.R., et al. 1962, Physical Review Letters, 9, 439

[38] Giacconi, R., Bechtold, J., Branduardi, G., et al. 1979, ApJ, 234, 1

[39] Goad, M.R., Roberts, T.P., Knigge, C., et al. 2002, MNRAS, 335, L67

[40] Goad, M.R., Roberts, T.P., Reeves, J.N., et al. 2006, MNRAS, 365, 191

[41] Griffiths, R.E., Schwartz, D.A., Schwarz, J., et al. 1979, ApJ, 230, 21

[42] Griffiths, R.E., Ptak, A., Feigelson, E.D., et al. 2000, Science, 290, 1325

[43] Grimm, H.J., Gilfanov, M., Sunyaev, R. 2003, MNRAS, 339, 793

[44] Gruber, D.E., Matteson, J.L., Peterson, L.E., et al. 1999, ApJ, 520, 124

[45] Heinzeller, D. & Duschl, W.J. 2007, MNRAS, 374, 1146

[46] Hirano, A., Kitamoto, S., Yamada, T.T., et al. 1995, ApJ, 446, 350

[47] Humphrey, P.J., Fabbiano, G., Elvis, M. et al. 2003, MNRAS, 344, 134

[48] Ichimaru, S. 1977, ApJ, 214, 840

[49] Inoue, H., Koyama, K., Makishima, K., et al. 1981, ApJ, 250, L71

[50] Ishisaki, Y., Makishima, K., Iyomoto, N., et al. 1996, PASJ, 48, 237

[51] Ishisaki, Y., Maeda, Y., Fujimoto, R., et al. 2007, PASJ, 59, S113

[52] Isobe, N., Kubota, A., Makishima, K., et al. 2007, astroph:07081804

[53] Kaaret, P. Prestwich, A.H., Zezas, A., et al. 2001, MNRAS, 321, L29

[54] Kaaret, P., Corbel, S., Prestwich, A.H. 2003, Science, 299, 365

[55] Kaaret, P., Ward, M.J., Zezas, A. 2004, MNRAS, 351, 83

[56] Kaaret, P., Simet, M.G., Lang, C.C. 2006, ApJ, 646, 174

[57] Karachentsev, I.D., Sharina, M.E., Dolphin, A.E., et al. 2002, A&A, 385, 21

[58] Katayama, H., Takahashi, I., Ikebe, Y., et al. 2004, A&A, 414, 767

[59] Kelley, R.L., Mitsuda, K., Allen, C.A., et al. 2007, PASJ, 59, S77

[60] King, A.R., Davies, M.B., Ward, M.J., et al. 2001, ApJ, 552, L109

[61] King, A.R. 2002, MNRAS, 335, L13

[62] Kobayashi, Y., Kubota, A., Nakazawa, K., et al. 2003, PASJ, 55, 273

[63] Kokubun, M., Makishima, K., Takahashi, T., et al. 2007, PASJ, 59, S53

[64] Kording, E., Falcke, H., Markoff, S. 2002, A&A, 382, 13

[65] Kording, E., Colbert, E., Falcke, H. 2005, A&A, 436, 427

[66] Koyama, K., Tsunemi, H., Dotani, T., et al. 2007, PASJ, 59, S23

[67] Kubota, A., Tanaka, Y., Makishima, K., et al. 1998, PASJ, 50, 667

[68] Kubota, A. 2001, Ph.D thesis, Univ. of Tokyo

[69] Kubota, A., Mizuno, T., Makishima, K., et al. 2001, ApJ, 547, L119

[70] Kubota, A., Done, C., Makishima, K., et al. 2002, MNRAS, 337, L11

[71] Kubota, A. & Makishima, K. 2004, ApJ, 601, 428

[72] Kuntz, K.D., Gruendl, R.A., Chu, Y.H., et al. ApJ, 620, L31

[73] Kuranov, A.G., Popov, S.B., Postnov, K.A., et al. 2007, MNRAS,

[74] La Parola, V., Peres, G., Fabbiano, G., et al. 2001, ApJ, 556, 47

[75] La Parola, V., Fabbiano, G., Elvis, M., et al. 2004, ApJ, 601, L831

[76] Lehmann, I., Becker, T., Fabrika, S., et al. 2005, A&A, 431, 847

[77] Liu, J.F., Bregman, J.N., Seitzer, P. 2002, ApJ, 580, L31

[78] Liu, J.F., Bregman, J.N., Irwin, J., et al. 2002, ApJ, 581, L93

[79] Liu, J.F., Bregman, J.N., Seitzer, P. 2004, ApJ, 602, 249

[80] Liu, J.F. & Bregman, J.N. 2005, ApJS, 157, 59

[81] Liu, J.F., Bregman, J.N., Irwin, J. 2006, ApJ, 642, 171

[82] Maccarone, T.J., Kundu, A., Zepf, S.E. 2003, ApJ, 586, 814

[83] McClintock, J.E., Remillard, R.A. 2006, Cambridge University Press

[84] Magdziarz, P., Blaes, O.M., Zdziarski, A.A., et al. 1998, MNRAS, 301, 179

[85] Makishima, K., Maejima, Y., Mitsuda, K., et al. 1986, ApJ, 308, 635

[86] Makishima, K., Kubota, A., Mizuno, T., et al. 2000, ApJ, 535, 632

[87] Malizia, A., Bassani, L., Zhang, S.N., et al. 1999, ApJ, 519, 637

[88] Matsumoto, H. & Tsuru, T.G. 1999, PASJ, 51, 321

[89] Matsumoto, H., Tsuru, T.G., Koyama, K., et al. 2001, ApJ, 547, L25

[90] Matsumoto, H., Tatsuya, I., Tsuru, T.G., et al. 2004, PTPS, No. 155, 379

[91] Miller, J.M., Fabian, A.C., Wijnands, R., et al. 2002, ApJ, 578, 348

[92] Miller, J.M., Fabbiano, G., Miller, M.C., et al. 2003, ApJ, 585, L37

[93] Miller, J.M., Fabian, A.C., Miller, M.C. 2004, ApJ, 607, 931

[94] Miller, J.M., Zezas, A., Fabbiano, G., et al. 2004, ApJ, 609, 728

[95] Miller, N.A., Mushotzky, R.F., Neff, S.G. 2005, ApJ, 623, L109

[96] Mineshige, S., Hirano, A., Kitamoto, S., et al. 1994, ApJ, 426, 308

[97] Mineshige, S., Kawaguchi, T., Takeuchi, M., et al. 2000, PASJ, 52, 499

[98] Mitsuda, K., Inoue, H., Koyama, K., et al. 1984, PASJ, 36, 741

[99] Mitsuda, K., Bautz, M., Inoue, H., et al. 2007, PASJ, 59, S1

[100] Miyaji, T., Lehmann, I., Hasinger, G. 2001, ApJ, 121, 3041

[101] Miyamoto, S., Kimura, K., Kitamoto, S., et al. 1991, ApJ, 383, 784

[102] Miyawaki, R., Sugiho, M., Kokubun, M., et al. 2004, PASJ, 56, 591

[103] Mizuno, T., Ohnishi, T., Kubota, A., et al. 1999, PASJ, 51, 663

[104] Mizuno, T. 2000, Ph.D thesis, Univ. of Tokyo

[105] Mizuno, T., Kubota, A., Makishima, K. 2001, ApJ, 554, 1282

[106] Mizuno, T., Takahashi, H., Ushio, M., et al. 2006, SUZAKU-MEMO-2006-42

[107] Mizuno, T., Miyawaki, R., Ebisawa, K., et al. 2007, PASJ, 59, S257

[108] Moran, E.C., & Lehnert, M.D. 1997, ApJ, 478, 172

[109] Mucciarelli, P., Casella, P., Belloni, T., et al. 2006, MNRAS, 365, 1123

[110] Murashima, M., Kubota, A., Makishima, K., et al. 2005, PASJ, 57, 279

[111] Mushotzky, R.F. 2004, Progress of Theoretical Physics Supplement, 155, 27

[112] Mushotzky, R.F. 2006, Advances in Space Research, 38, 2793

[113] Nakamura, N., Dotani, T., Inoue, H., et al. 1989, PASJ, 41, 617

[114] Narayan, R. & Yi, I. 1994, 428, L13

[115] Neff, S.G., Ulvestad, J.S., Campion, S.D. 2003, ApJ, 599, 1043

[116] Okada, K., Dotani, T., Makishima, K., et al. 1998, PASJ, 50, 250

[117] Okajima, T., Ebisawa, K., Kawaguchi, T. 2006, ApJ, 652, L1050

[118] Ogawa. 1992 MSc. thesis, Rikkyo Univ.

[119] Paczynski, B. 1974, A&A, 34, 161

[120] Pakull, M.W. & Mirioni, L. 2002, astro-ph/0202488

[121] Pakull, M.W. & Mirioni, L. 2003, Revista Mexicana de Astronomia y Astrofisica, 15, 197

[122] Pellegrini, S., Cappi, M., Bassani, L., et al. 2000, A&A, 353, 447

[123] Petre, R., Okada, K., Mihara, T., et al. 1994, PASJ, 46, L115

[124] Ptak, A. & Griffiths, R. 1999, ApJ, 517, L85

[125] Ptak, A. & Colbert, E. 2004, ApJ, 606, 291

[126] Ptak, A., Colbert, E., van der Marel, R.P., et al. 2006, ApJS, 166, 154

[127] Ranalli, P., Origlia, L., Comastri, A., et al. 2006, astro-ph/0607322

[128] Rephaeli, Y., & Gruber, D. 2002, A&A, 389, 752

[129] Roberts, T.P., & Warwick, R.S. 2000, MNRAS, 315, 98

[130] Roberts, T.P., Goad, M.R., Ward, M.J., et al. 2000, MNRAS, 325, L7

[131] Roberts, T.P. & Warwick, R.S. 2002, MNRAS, 315, 98

[132] Roberts, T.P., Warwick, R.S., Ward, M.J., et al. 2004, MNRAS, 349, 1193

[133] Roberts, T.P., Warwick, R.S., Ward, M.J., et al. 2005, MNRAS, 357, 1363

[134] Roberts, T.P., Kilgard, R.E., Warwick R.S., et al. 2006, MNRAS, 371, 1877

[135] Roberts, T.P. 2007, astro-ph/0706.2562

[136] Sanchez-Sutil, J.R., Munoz-Arjonilla, A.J., Marti, J. et al. 2006, A&A, 452, 739

[137] Schaaf, R., Pietsch, W., Biermann, P.L., et al. 1989, ApJ, 336, 722

[138] Serlemitsos, P.J., Soong, Y., Chan, K., et al. PASJ, 59, S9

[139] Shakura, N.I. & Syunyaev, R.A. 1973, A&A, 24, 337

[140] Shimura, T. & Takahara, F. 1995, ApJ, 445, 780

[141] Soifer, B.T., Neugebauer, G., Houck, J.R. 1987, ARA&A, 25, 187

[142] Soria, R., & Wu, K. 2002, A&A, 384, 99

[143] Soria, R., Monch, C., Read, A.M., et al. 2004, A&A, 423, 955

[144] Soria, R., Fender, R.P., Hannikainen, D.C. et al. 2006, MNRAS, 368, 1527

[145] Stevens, I.R., Read, A.M., Bravo-Guerrero, J. 2003, MNRAS, 343, L47

[146] Stobbart, A.M., Roberts, T.P., Wilms, J. 2006, MNRAS, 368, 397

[147] Strickland, D.K. & Heckman, T.M. 2007, ApJ, 658, S258

[148] Strohmayer, T.E. & Mushotzky, R.F. 2003, ApJ, 586, L61

[149] Strohmayer, T.E., Mushotzky, R.F., Winter, L. et al. 2007, ApJ, 660, 580

[150] Sugiho, M., Kotoku, J., Makishima, K., et al. 2001, ApJ, 561, 73

[151] Sugiho, M 2003, Ph.D thesis, Univ. of Tokyo

[152] Swartz, D.A., Ghosh, K.K., Tennant, A.F., et al. 2004, ApJS, 154, 519

[153] Takahashi, T., Abe, K., Endo, M., et al. 2007, PASJ, 59, S35

[154] Takizawa, M. 1991 MSc. thesis, Univ. of Tokyo

[155] Tanaka, Y., Nandra, K., Fabian, A.C., et al. 1995, Nature, 375, 659

[156] Terashima, Y. & Wilson, A.S. 2003, ApJ, 583, 145

[157] Tsunoda, N., Kubota, A., Namiki, M., et al. 2006, PASJ, 58, 1081

[158] Tsuru, T. 1992, Ph.D thesis, Univ. of Tokyo

[159] Tsuru, T.G., Awaki, H., Koyama, K., et al. 1997, PASJ, 49, 619

[160] Tsuru, T.G., Matsumoto, H., Inui, T., et al. 2004, PTPS, No. 155, 59

[161] Tsuru, T.G., Ozawa, M., Hyodo, Y., et al. 2007, PASJ, 59, S269

[162] Tully, R.B. 1988, Nearby Galaxies Catalog, Cambridge University Press

[163] Turolla, R., Mucciarelli, P., Zampieri, L., et al. 2006, Advances in Space Research, 38, 7, 1374

[164] Uno, S., Mitsuda, K., Inoue, H., et al. 2002, ApJ, 565, 419

[165] van der Klis, M. 1995, Proceedings of the IAU Colloquium

[166] Vazquez, G.A., Hornschemeier, A.E., Colbert, E., et al. 2007, ApJ, 658, L21

[167] Vierdayanti, K., Mineshige, S., Ebisawa, K., et al. 2006, PASJ, 58, 915

[168] Wang, Q.D. 2002, MNRAS, 332, 764

[169] Wang, Q.D., Yao, Y., Fukui, W., et al. 2004, ApJ, 609, 113

[170] Watanabe, S., Ushio, M., Tanaka, T., et al. 2007, SUZAKU-MEMO-2007-01

[171] Watarai, K., Fukue, J., Takeuchi, M., et al. 2000, PASJ, 52, 133

[172] Watarai, K., Mizuno, T., Mineshige, S. 2001, ApJ, 549, L77

[173] Watson, M.G., Stanger, V., Griffiths, R.E. 1984, ApJ, 286, 144

[174] Weisskopf, M.C., Wu, K., Tennant, A.F., et al. 2004, ApJ, 605, 360

[175] Winter, M.L., Mushotzky, R.F., Reynolds, C.S. 2006, ApJ, 649, 730

[176] Wu, H., Xue, S.J., Xia, X.Y., et al. 2002, ApJ, 576, 738

[177] Zampieri, L., Mucciarelli, P., Falomo, R., et al. 2004, ApJ, 603, 523

[178] Zezas, A., & Fabbiano, G. 2002, ApJ, 577, 726

Acknowledgements

First of all, I am deeply grateful to Prof. K. Makishima for his guidance and large support to establish this thesis. As well as a number of astrophysical comments, he showed me an attitude toward scientific research and provided me with invaluable experiences during my graduate courses. I also thank Dr. N. Nakamura, Dr. K. Sato, Dr. T. Shigeyama, Dr. F. Hamba, and Dr. K. Mitsuda for referees of this thesis and valuable comments to improve it.

I would like to express my thanks to Dr. M. Kokubun and Dr. K. Nakazawa because I owe them a great deal all through my graduate school life. I also thank Dr. T. Mizuno and Dr. A. Kubota for useful comments and valuable discussion about ULXs and BHBs. Furthermore, I wish to appreciate very much to my laboratory members, Dr. M. Sugiho, Dr. Y. Ezoe, Dr. J. Kotoku, Dr. I. Takahashi, Dr. Y. Okada, Dr. H. Takahashi, Dr. M. Kawaharada, Dr. M. Murashima, Mr. D. Kasama, Dr. T. Yanagida, Dr. T. Itoh, Dr. H. Niko, Mr. T. Kitaguchi, Mr. S. Hirakuri, Mr. T. Enoto, Mr. M. Sato, Mr. S. Yamada, Mr. T. Yuasa, Mr. T. Ueda, Mr. Y. Uehara, and Mr. S. Okuyama, for encouraging me and having fruitful discussion. Finally, I express my gratitude to all the *Suzaku* and HXD members and hope that they will give us more exciting astrophysics.